

Measurement of Cross-Sections of exclusive π^0
 Photo-production on Hydrogen from 1.1 GeV -
 5.45 GeV using $e^+e^-\gamma$ decay from the CLAS/g12
 Data

Michael C. Kunkel[†]

Old Dominion University, VA (U.S.A.)

Abstract

Photoproduction of the π^0 meson was studied using the CLAS detector at Thomas Jefferson National Accelerator Facility using tagged incident beam energies spanning the range $E_\gamma = 1.1$ GeV - 5.45 GeV. The measurement is performed on a liquid hydrogen target in the reaction $\gamma p \rightarrow pe^+e^-(\gamma)$. The final state of the reaction is the sum of two subprocesses for π^0 decay, the Dalitz decay mode of $\pi^0 \rightarrow e^+e^-\gamma$ and conversion mode where one photon from $\pi^0 \rightarrow \gamma\gamma$ decay is converted into a e^+e^- pair. This specific final state reaction avoided limitations caused by single prompt track triggering and allowed a kinematic range extension to the world data on π^0 photoproduction to a domain never systematically measured before.

We report the measurement of the π^0 differential cross-sections $\frac{d\sigma}{d\Omega}$ and $\frac{d\sigma}{dt}$. The angular distributions agree well with the SAID parametrization for incident beam energies below 3 GeV, while an interpretation of the data for incident beam energies greater than 3 GeV is currently being developed.

^{*}email: m.kunkel@fz-juelich.de

[†]Now at Forschungszentrum Jülich, Jülich (Germany)

Contents

1	Introduction	6
2	Data Selection and Analysis Cuts	6
2.1	Event Selection	6
2.2	Lepton Identification	8
2.2.1	Lepton Triggering and Neutral Triggering	8
2.3	Kinematic Fitting	11
2.3.1	Tuning	11
2.3.2	Analysis Fitting	19
2.3.3	Kinematic Fitting Analysis and Cuts	21
2.3.4	1-C & 4-C Cuts	26
2.3.5	Missing Energy Cut	29
2.3.6	2-C Cut	32
2.4	Particle Vertex Timing Cuts	36
2.5	z Vertex Cuts	37
2.5.1	Final MC Distribution	39
2.5.2	Final Data Distribution	40
2.6	Lepton Trigger Efficiency for π^0 Candidates	40
3	Target Density	41
4	Photon Normalization	42
5	Fiducial Cut	42
6	Normalization	43
6.1	Normalization History	43
6.2	g12 Normalization Procedure	43
6.3	g12 Normalization Results	46
6.4	Normalization Comparison	56
6.5	Normalization Uncertainties	57
7	Simulation	57
7.1	Simulation Verification	58
7.2	PLUTO++ Event Generator	59
7.3	Simulating the Lepton Trigger	60
7.3.1	Validity of Trigger Simulation	61
7.4	Simulation Kinematic Variables Verification	61
7.5	Acceptance	68

8 Results	69
8.1 Cross-Section	69
8.2 Statistical Uncertainties	70
8.3 Systematic Uncertainty	73
8.3.1 Branching Ratio Systematic Uncertainty	73
8.3.2 Cut Based Systematic Uncertainty	75
8.3.3 Photon Flux Systematic Uncertainty	76
8.3.4 Detector Efficiency Systematic Uncertainty	77
8.3.5 z -vertex Cut Systematic Uncertainty	79
8.3.6 Target Systematic Uncertainty	79
8.3.7 Track Efficiency Systematic Uncertainty	79
8.3.8 Total Systematic Uncertainty	89
8.4 Comparison to World Data and SAID Fits	90
8.4.1 Differential Cross-Sections $\frac{d\sigma}{d\Omega}$	90
8.4.2 Excitation Functions	95
8.4.3 t -Dependence	97
8.4.4 SAID χ^2 Improvements	101
8.4.5 Discussion of SAID Fits and Comaprision to World Data	101
9 Conclusions	102
BIBLIOGRAPHY	103
10 Appendix I	105
10.1 Acceptance plots	105
10.2 Acceptance plots	116

1 Introduction

In hadron physics, photoproduction of single pion is essential to understand the photon-nucleon vertex. At low energies, the photon-nucleon coupling establishes excited nucleon resonances which has been at the forefront of physics "missing resonances" search. At high energies single pion photoproduction can be used to test predictions of Regge theory, in which recent calculations [1] have shown to describe the presented data well. Furthermore, these measurements have shown that the differential cross section for single pion photoproduction at fixed c.m. angles, $\theta_{c.m.}$, where the mandelstam variables s , t , and u are large, seem to scale as $\frac{d\sigma}{dt} \sim s^{2-n} f(\theta_{c.m.})$, where s and t are the Mandelstam variables and n is the total number of interacting elementary fields in the initial and final state of the reaction. This is predicted by the constituent counting rule [2, 3] and exclusive measurements in pp and $\bar{p}p$ elastic scattering [4, 5], meson-baryon Mp reactions [5], and photoproduction γN [6, 7, 8, 9, 10, 11, 12, 13] agree well with this rule.

This analysis note details the CLAS g12 data set, the extraction of the π^0 signal from the data, the Monte-Carlo techniques utilized for acceptance correction and the track efficiency calculation used for correcting the data. Also to be shown is the differential cross-sections through the entire beam energy range of the g12 experiment, a comparison of the differential cross-section with existing world data.

This analysis note details the analysis techniques and corrections not already discussed and approved in the g12 analysis note procedure document [14]. All relevant procedures described in [14] have been applied to this analysis. See checklist.

2 Data Selection and Analysis Cuts

2.1 Event Selection

The reaction chain of interest in this analysis is:

$$\gamma p \rightarrow p + x \tag{1}$$

where x is reconstructed from the missing mass of $p(\gamma, p)x$ off the target proton and the tagged photon. The meson x can then decay according to

$$x \rightarrow e^+ e^- (\gamma) \tag{2}$$

where the decay product γ is left undetected. For the π^0 meson the decay products, e^+, e^-, γ , can arise from two main decay branching ratios found in Tab. 1. The first decay of $\pi^0 \rightarrow \gamma\gamma$ can produce electron/positron pairs via external conversion inside the hydrogen target, i.e. $\gamma \rightarrow e^+ e^-$, while the second decay $\pi^0 \rightarrow e^+ e^- \gamma$ is produced via Dalitz decays. The total sum of both branching ratios accounts for $\sim 99.997\%$ of all decays of π^0 .

Mode	Branching ratio
$\pi^0 \rightarrow 2\gamma$	$(98.823 \pm 0.034) \cdot 10^{-2}$
$\pi^0 \rightarrow e^+e^-\gamma$	$(1.174 \pm 0.035) \cdot 10^{-2}$
$\pi^0 \rightarrow \gamma$ positronium	$(1.82 \pm 0.29) \cdot 10^{-9}$
$\pi^0 \rightarrow e^+e^+e^-e^-$	$(3.34 \pm 0.16) \cdot 10^{-5}$
$\pi^0 \rightarrow e^+e^-$	$(6.46 \pm 0.33) \cdot 10^{-8}$
$\pi^0 \rightarrow 4\gamma$	$< 2 \cdot 10^{-8}$
$\pi^0 \rightarrow \nu\bar{\nu}$	$< 2.7 \cdot 10^{-7}$
$\pi^0 \rightarrow \nu_e\bar{\nu}_e$	$< 1.7 \cdot 10^{-6}$
$\pi^0 \rightarrow \nu_\mu\bar{\nu}_\mu$	$< 1.6 \cdot 10^{-6}$
$\pi^0 \rightarrow \nu_\tau\bar{\nu}_\tau$	$< 2.1 \cdot 10^{-6}$
$\pi^0 \rightarrow \gamma\nu\bar{\nu}$	$< 6 \cdot 10^{-4}$

Table 1: Branching ratios of the π^0 decay. [15]

Pions were skimmed initially because lepton identification is done at the analysis level. If the event satisfied the requirements listed in Table 2, then all timing, momentum and vertex information was outputted as well as CC and EC information. To reduce the size of the data set, a cut was placed on the total missing mass of $\gamma p \rightarrow p\pi^+\pi^-$ to be less than 275 MeV. This cut was broad enough to not interfere with π^0 selection from single π^0 production i.e. $\gamma p \rightarrow p\pi^0$ when assigned the pion the lighter mass of a electron/positron. This broad cut also does not interfere with π^0 production from light meson decay, i.e $\gamma p \rightarrow p\omega \rightarrow p\pi^+\pi^-\pi^0$.

Requirement
One in-time beam photon
One proton
One π^+ or “unknown” of q^+
One π^- or “unknown” of q^-

Table 2: Requirements of initial skim

The probability that there is a 2nd in-time photon detected is 18% at $E_\gamma = 1.1$ GeV and ~4% at $E_\gamma = 4.4$ GeV and ~2% at 5.5 GeV. Therefore the chance we choose the incorrect photon is half of these value, i.e. 9% at $E_\gamma = 1.1$ GeV and ~2% at $E_\gamma = 4.4$ GeV and ~1% at 5.5 GeV. The track-efficiency corrections (Sec. 6) derived with $p\pi^+\pi^-$ also were affected by this phenomena (i.e. skimmed with only one photon) and corrected this normalization. A study was performed using all in-time photons in which the track efficiency was also calculated with all in-time photons, the difference on the reported results was negligible

2.2 Lepton Identification

Typically, electron and positron identification in the CLAS is done by using selection cuts on the energy deposited in the EC and on the minimum number of photoelectrons in the CC. For electron runs, this allows to separate the scattered electron from negatively-charged pions. Since we are interested in a lepton pair produced in the pi0 decay for the two-body reaction $\gamma p \rightarrow p\pi^0 \rightarrow pe^+e^-(\gamma)$, we follow a different approach based in kinematics. Once the data is skimmed according to Table 2, all tracks that were identified in the PART bank as π^+ , π^- , unknown with q^+ , or unknown with q^- tracks, were assigned the electron mass for the 1-C and the 2-C kinematic fitting of the $\gamma p \rightarrow pe^+e^-(\gamma)$ final state, and the pion mass for the 4-C kinematic fitting of the $\gamma p \rightarrow p\pi^+\pi^-(\gamma)$ final state, as described in Sec. 2.3.2. The 4-C fitting was used to select and remove true $p\pi^+\pi^-$ events while the 1-C and the 2-C fits were used to select only true $\gamma p \rightarrow pe^+e^-(\gamma)$ and $p\pi^0$ final states, respectively. Thus, true pion tracks who are consistent with the two-pion final state were removed kinematically from our sample, while all the other tracks that were assigned the electron mass but were not true electron or positron tracks were also kinematically removed from the sample by the 1-C and the 2-C fits. This approach eliminated the need to apply dedicated electron/positron identification selection cuts.

2.2.1 Lepton Triggering and Neutral Triggering

In g12, since the CC was filled with gas, it was possible to include the CC as a component of the trigger. There were three trigger “bits” used for lepton identification in g12 as listed in Table 3. Each “bit” used a (EC·CC) configuration to identify leptons. The (EC·CC) configuration required a coincidence between the electromagnetic calorimeter and the Cherenkov subsystems. This coincidence was established by using the voltage sum of the CC for a sector and the voltage sum of the EC for the same sector and comparing each sum to a preset threshold described in Table 4. The EC voltage sum threshold comparison is done on both the EC_{inner} and EC_{total} which are the EC voltage signals for the energy deposited in the inner layer and in all layers. The labels of photon or electron specified in Table 4 are not actual photons or electrons, but were considered a first-order approximation for detection. The particle identification is done at the analysis level. The method for determining the (EC·CC) does not allow for multiple lepton triggering in the same sector. Determining multiple leptons in the same sector is done at the analysis level.

The “bit 6” trigger configuration, (ST·TOF)·(EC·CC) requires a ST and TOF coincidence previously described in [14] along with a coincidence between the electromagnetic calorimeter and the Cherenkov subsystems described above. The (ST·TOF) configuration of “bit 6” did not have to be in the same sector

as the (EC·CC) configuration of “bit 6”. The “bit 11” trigger configuration, (EC·CC)×2 requires two coincidences between the electromagnetic calorimeter and the Cherenkov subsystems described above, in two different sectors.

The “bit 5” trigger configuration was also established as a lepton trigger. It required EC hits in two sectors. The “bit 5” trigger configuration was also established to analyze physics involving two or more neutral particles accompanied with a charged track, such as exclusive π^0 production in which the π^0 decays via 2 photons. The method for “bit 5” voltage sum comparison is identical to the EC voltage sum of “bit 6” and “bit 11”

It should be noted that none of the lepton triggers required a MOR signal, allowing for physics involving leptons to be measured starting from g12’s lowest tagger detection value of 1.142 GeV.

For this analysis, runs which had the “bit 6” trigger configuration were used. To satisfy the trigger requirement in the data for photon beam energies < 3.6 GeV, cuts were placed on the EC and CC hit quantities recorded. Since either lepton could have produced the needed hits, the cut was a permutation of both leptons, i.e.

$$e_{\text{EChit}}^+ \& e_{\text{CChit}}^+ \text{ OR } e_{\text{EChit}}^- \& e_{\text{CChit}}^- \text{ OR } e_{\text{EChit}}^+ \& e_{\text{CChit}}^- \text{ OR } e_{\text{EChit}}^- \& e_{\text{CChit}}^+ \quad (3)$$

An analysis on the trigger efficiency for π^0 events was performed and is discussed in Sec. 2.6. For data with photon beam energies > 3.6 GeV, the analysis relied on the ”two-prong“ “bits 2-3”.

g12 runs 56595–56607, 56648–57323			
bit	definition	L2 multiplicity ^a	prescale
1	MORA·(ST·TOF)	1	1000/300 ^b
2	MORA·(ST·TOF)×2	2/ ^c	1
3	MORB·(ST·TOF)×2	2	1
4	ST·TOF	1	1000/300
5	(ST·TOF)·EC×2	1	1
6	(ST·TOF)·(EC·CC)	2	1
7	MORA·(ST·TOF)·(EC·CC)	—	1
8	MORA·(ST·TOF)×2	—	1
11	(EC·CC)×2	—	1
12	(ST·TOF)×3	—	1

Table 3: Trigger configuration for g12 runs from 56595 to 56607 and 56648 to 57323.

^aLevel 2 triggering was turned off on all bits for runs 56605, 56607 and 56647.

^bPrescaling for bits 1 and 4 were 1000 for runs prior to 56668 at which point they both were changed to 300.

^cLevel 2 triggering of bit 2 was set to 2 for runs prior to 56665 at which point it was turned off.

EC		CC
“photon”	“electron”	
50/100 mV	60/80 mV	20/20 mV
150/300 MeV	180/240 MeV	~0.4 photo-electrons

Table 4: Threshold values for the electromagnetic calorimeter (EC) and Cherenkov counter (CC) during the g12 running period. EC thresholds are shown as *inner/total*, and CC thresholds are shown as *left/right*.

2.3 Kinematic Fitting

2.3.1 Tuning

In order for the kinematic fitter to perform a χ^2 minimization properly, it has to be provided with an initial covariance matrix that contains the correlations between the kinematic variables of each track as determined during the reconstruction of the track. The covariance matrix recorded by CLAS is inadequate to use in the kinematic fitter because the covariance matrix does not incorporate multiple scattering errors, “energy loss” or the error approximation is misrepresented by a systematic. To correct for this, the elements of the covariance matrix are scaled appropriately by the kinematic fitter routine by means of what is called “tuning”. The process of “tuning” determines the nature of the misrepresented errors as a function of a measured variable by studying the shift from the zero mean at different ranges of dependent variables. To perform a “tune”, a test channel must be chosen in which the event selection must be background free. The multiple scattering option used in this analysis was set to false, therefore an algorithm which attempts to incorporate multiple scattering is not utilized. Instead a directory of parameterization files are called for the scaling of individual particle covariance matrix elements, such as p , π^+ , π^- , e^+ and e^- . This was done because the multiple scattering algorithm did not perform well for events involving electrons and positrons.

For this analysis, the channels

$$\gamma p \rightarrow \pi^+ \pi^- (p) \quad (4)$$

$$\gamma p \rightarrow p \pi^- (\pi^+) \quad (5)$$

$$\gamma p \rightarrow \pi^+ p (\pi^-) \quad (6)$$

$$\gamma p \rightarrow p \omega / \rho \rightarrow p e^+ e^- \quad (7)$$

were chosen as the “tune” channels because these channels incorporate the physics and background of the analysis performed. The reactions 4, 5, 6 were “tunes” done individually for the proton, π^+ and π^- respectively, while 7 “tuned” the electrons and positrons together because of the limit in statistics needed to tune each lepton individually. Once the “tuning” for 4, 5, 6 was complete, the “tune” was verified by checking the pull distributions and confidence level for the topology,

$$\gamma p \rightarrow p \pi^+ \pi^- . \quad (8)$$

Figures 1 and 2 illustrate the quality of the “tuned” covariance matrix for g12 data and g12 simulation of electrons and positrons from “tune” 7 and Fig. 3 illustrates the “confidence levels” for g12 data and simulation of electrons and positrons from “tune” 7. Figures 4 and 5 illustrate the quality of the “tuned” covariance matrix for g12 data and g12 simulation of π^+ and π^-

from “tune” 8 and Fig. 6 illustrates the “confidence levels” for g12 data and simulation of π^+ and π^- from “tune” 8. The variables p used in Figs. 1, 2, 4 and 5 represent the lab frame momentum. The λ variable is the angle between the track and the (x_{track}, y_{track}) plane. The ϕ variable is the angle in the sector’s (x_{track}, y_{track}) plane relative to the x_{track} -axis, or between the track and the beam line [16]. The parameters for Fig. 1 and Fig. 2 can be read in Tab. 5, while the parameters for Fig. 4 and Fig. 5 can be read in Tab. 6.

	Data		MC	
	μ	σ	μ	σ
Proton p-pull	0.2197	1.166	0.2965	1.11
Proton λ -pull	-0.1012	1.042	0.02447	1.221
Proton ϕ -pull	0.2191	1.245	0.01365	1.029
e^+ p-pull	0.2479	0.9045	0.4585	0.9494
e^+ λ -pull	0.1091	1.131	0.01275	1.174
e^+ ϕ -pull	0.1005	1.134	0.02877	1.012
e^- p-pull	0.2344	0.8944	0.4387	0.9443
e^- λ -pull	-0.0096	1.11	0.004	1.196
e^- ϕ -pull	0.8599	1.18	-0.01726	1.01
γ E-pull	-0.2269	1.116	-0.4832	1.03

Table 5: Pull distributions parameters for $\gamma p \rightarrow pe^+e^-$

	Data		MC	
	μ	σ	μ	σ
Proton p-pull	0.05151	1.163	0.1156	1.1027
Proton λ -pull	-0.03651	0.8975	0.01087	0.8408
Proton ϕ -pull	0.0076	1.113	-0.00081	0..9341
π^+ p-pull	0.0117	1.06	0.09357	0.9385
π^+ λ -pull	-0.0138	0.9362	0.009637	0.8591
π^+ ϕ -pull	-0.0081	1.075	-0.0304	0.9415
π^- p-pull	-0.0563	1.079	0.08686	0.9741
π^- λ -pull	-0.01515	0.9406	0.006595	0.8728
π^- ϕ -pull	-0.02302	1.115	-0.06083	0.9567
γ E-pull	0.004492	1.147	-0.1481	1.0

Table 6: Pull distributions parameters for $\gamma p \rightarrow p\pi^+\pi^-$

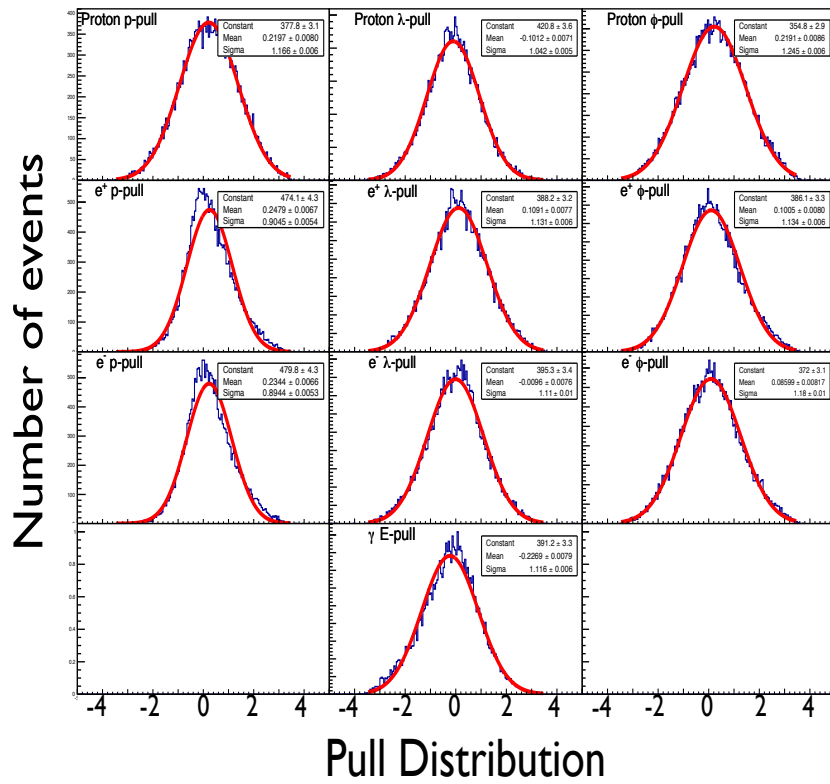


Figure 1: Number of events vs. Pull distribution for the (4-C) kinematic fit for $\gamma p \rightarrow pe^+e^-$ for g12 data with a 1% Confidence Level cut applied, and a Gaussian fit to each.

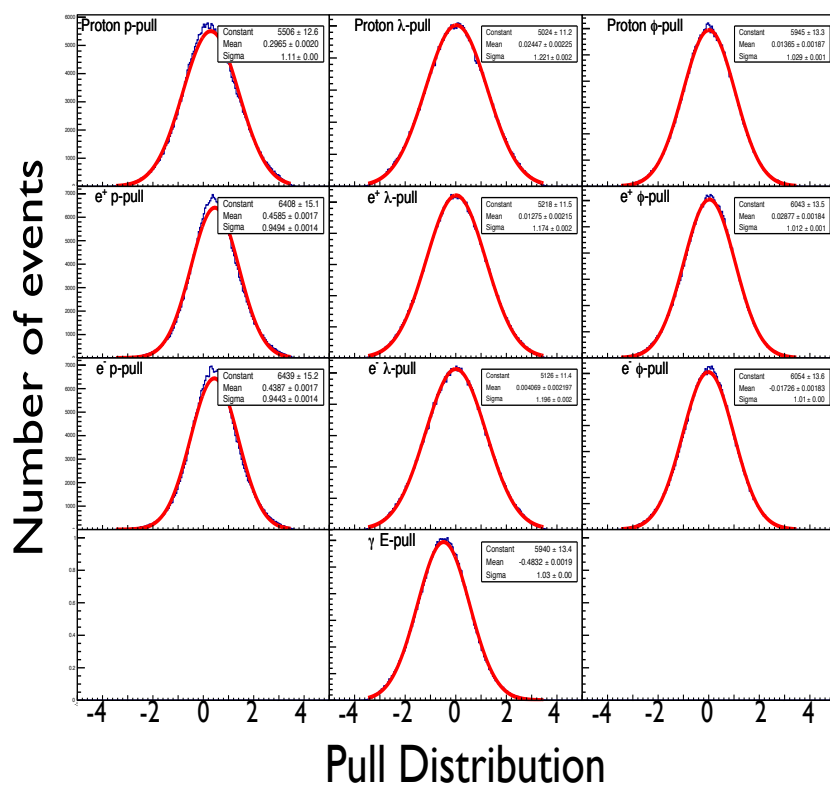


Figure 2: Number of events vs. Pull distribution for the (4-C) kinematic fit for $\gamma p \rightarrow pe^+e^-$ for g12 simulation with a 1% Confidence Level cut applied, and a Gaussian fit to each.

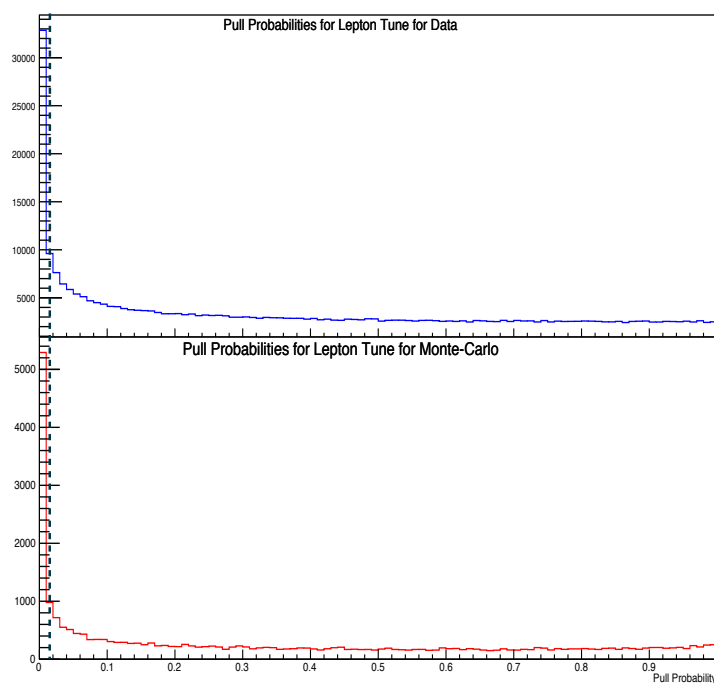


Figure 3: Number of events vs. Confidence Level for g12 (top) data and g12 simulation (bottom) for a (4-C) fit using $\gamma p \rightarrow pe^+e^-$. The black dashed line indicates the cut taken, events with probability <1% are rejected.

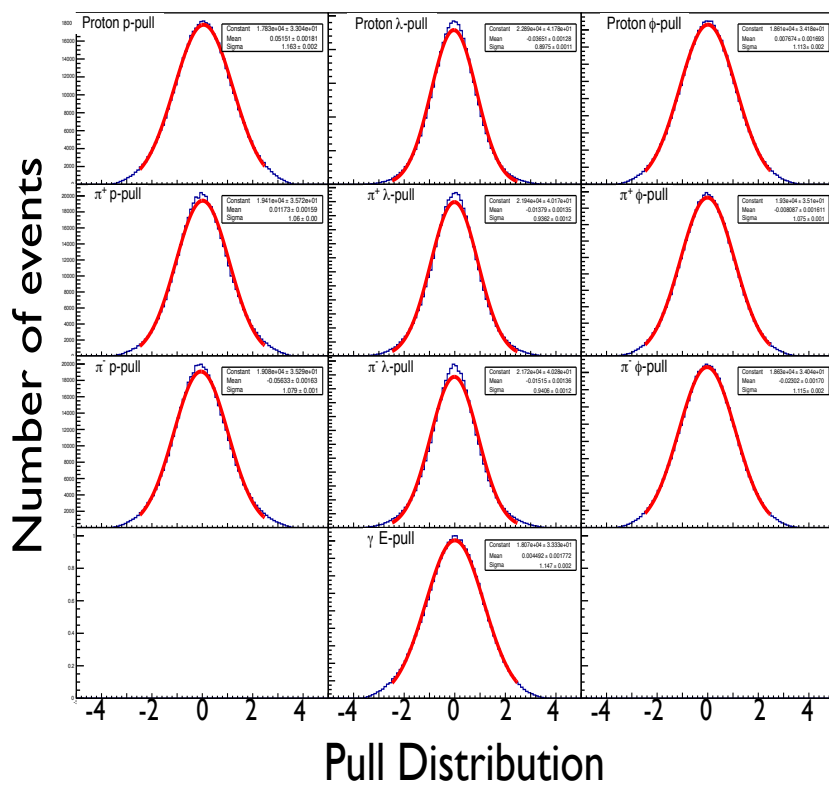


Figure 4: Number of events vs. Pull distribution for the (4-C) kinematic fit for $\gamma p \rightarrow p\pi^+\pi^-$ for g12 data with a 1% Confidence Level cut applied, and a Gaussian fit to each.

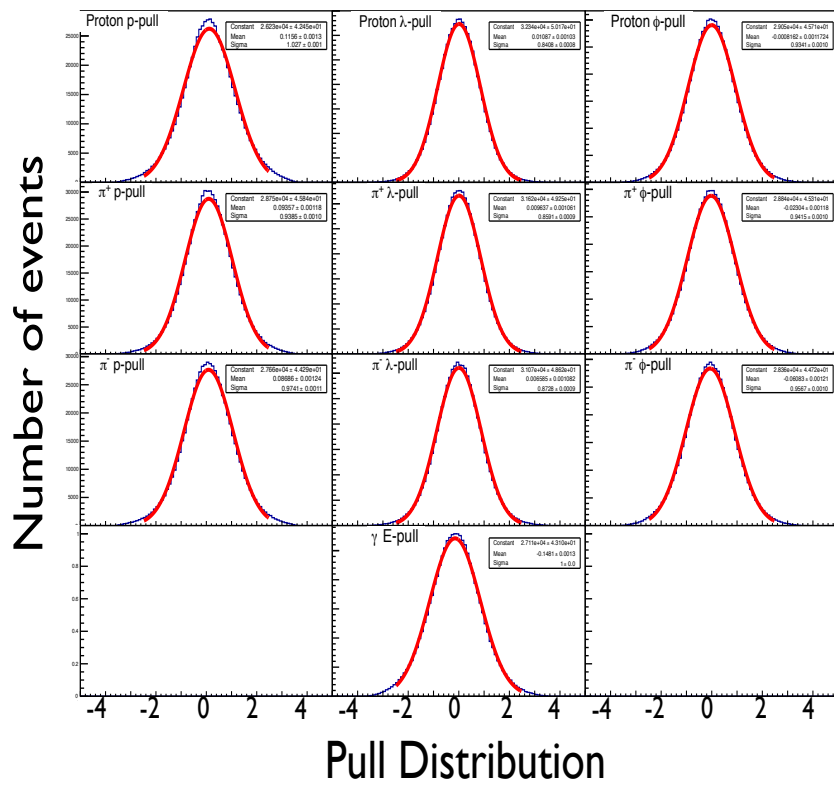


Figure 5: Number of events vs. Pull distribution for the (4-C) kinematic fit for $\gamma p \rightarrow p\pi^+\pi^-$ for g12 simulation with a 1% Confidence Level cut applied, and a Gaussian fit to each.

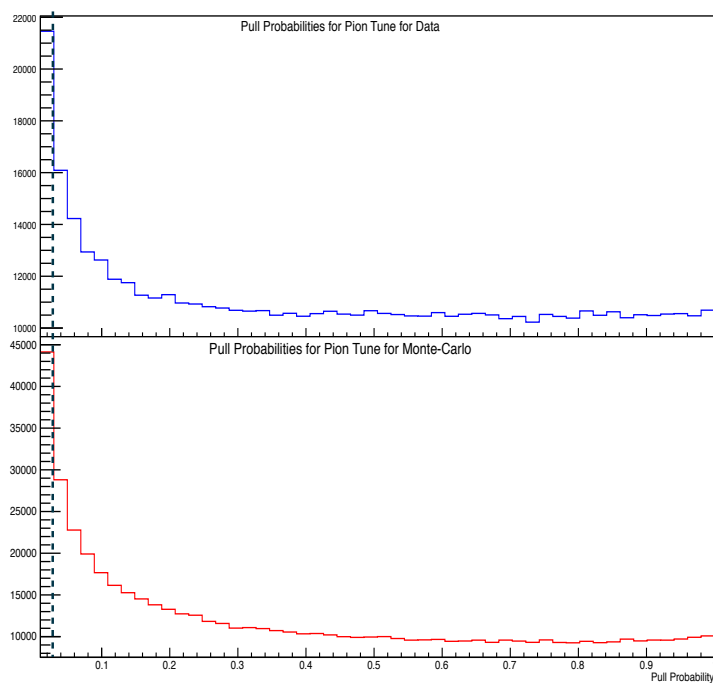


Figure 6: Number of events vs. Confidence Level for g12 (top) data and g12 simulation (bottom) for a (4-C) fit using $\gamma p \rightarrow p\pi^+\pi^-$. The black dashed line indicates the cut taken, events with probability <1% are rejected.

2.3.2 Analysis Fitting

This analysis performed three separate kinematic fitting hypotheses, 4-C, 1-C and 2-C. The 4-C fit used the $\gamma p \rightarrow p\pi^+\pi^-$ channel to filter background from double charged pion production from single π^0 production. The 1-C fit was used to the topology of $\gamma p \rightarrow pe^+e^-(\gamma)$ to fit to a missing final state photon. The constraint equation for this 1-C fit is given in Eq. 9.

$$\mathcal{F} = \begin{bmatrix} E_{beam} + M_p - (E_p + E_{e^+} + E_{e^-} + E_x) \\ \vec{p}_{beam} - (\vec{p}_p + \vec{p}_{e^+} + \vec{p}_{e^-} + \vec{p}_x) \end{bmatrix} = \vec{0} \quad (9)$$

The constraint equation for this 4-C fit is given in Eq. 10.

$$\mathcal{F} = \begin{bmatrix} E_{beam} + M_p - (E_p + E_{\pi^+} + E_{\pi^-}) \\ \vec{p}_{beam} - (\vec{p}_p + \vec{p}_{\pi^+} + \vec{p}_{\pi^-}) \end{bmatrix} = \vec{0} \quad (10)$$

The 2-C fit was used to the topology of $\gamma p \rightarrow pe^+e^-(\gamma)$ to fit to a missing final state photon but also to constrain the invariant mass of $e^+e^-(\gamma) = m_{\pi^0}^2$. The constraint equation for this 2-C fit is given in Eq. 11.

$$\mathcal{F} = \begin{bmatrix} (E_{e^+} + E_{e^-} + E_x)^2 - (\vec{p}_{e^+} + \vec{p}_{e^-} + \vec{p}_x)^2 - M_{\pi^0}^2 \\ E_{beam} + M_p - (E_p + E_{e^+} + E_{e^-} + E_x) \\ \vec{p}_{beam} - (\vec{p}_p + \vec{p}_{e^+} + \vec{p}_{e^-} + \vec{p}_x) \end{bmatrix} = \vec{0} \quad (11)$$

The “confidence levels” for each constraint Eq. 9, 10, 11 are shown in Fig. 7 and Fig. 8 for g12 data and simulation respectively. These quantities ensure proper mass and energy constraints for this analysis. Cuts on these quantities are discussed in Sec. 2.3.3.

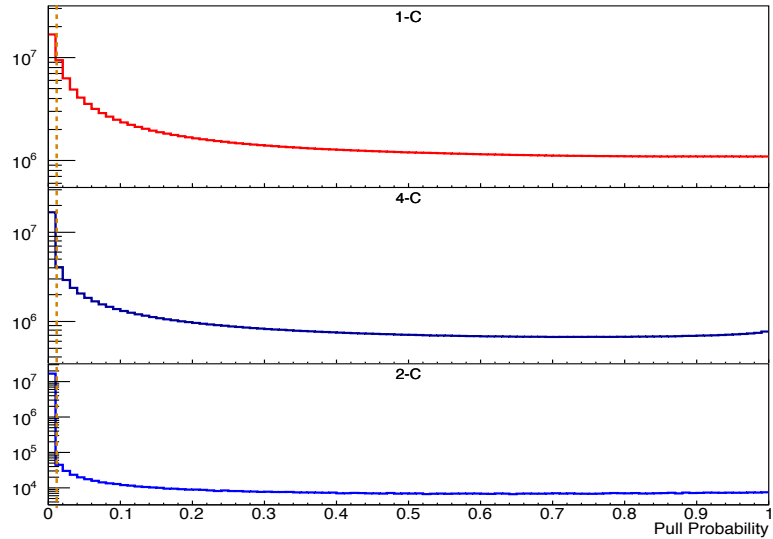


Figure 7: Number of data events plotted vs. Pull probability distribution for the 1-C(red,Eq. 9), 4-C(black,Eq. 10), 2-C(blue,Eq. 11) for g12 data. The orange dashed line illustrates the 1% cut for all pull probability distributions.

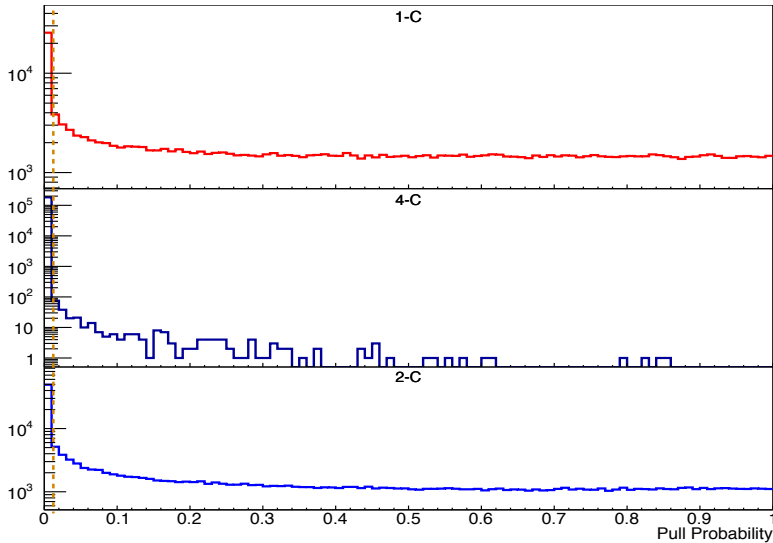


Figure 8: Number of data events plotted vs. Pull probability distribution for the 1-C(red,Eq. 9), 4-C(black,Eq. 10), 2-C(blue,Eq. 11) for g12 simulation. The orange dashed line illustrates the 1% cut for all pull probability distributions.

2.3.3 Kinematic Fitting Analysis and Cuts

The base hypothesis of all corrections performed to the data by the kinematic fitter was the 1-C constraint equation found in Eq. 9. This means that all fitted data will be presented in quantities based upon the hypothesis of a missing photon. The effect of 1-C kinematic fitting for events, prior to any topological cuts, with beam energies less than 3.6 GeV can be seen in Fig. 9, while for beam energies greater than 3.6 GeV can be seen in Fig. 10. The top panel depicts the unfitted data and the bottom panel depicts the data output from the kinematic fitter. The red data line represents all data while the blue line depicts the data where cuts were placed on CC and EC hits in order to satisfy the trigger as discussed in Sec 2.2.1 Eq. 3. The red, vertical dashed-dotted line illustrates the production point for two charged pion production. The MC counterpart plots of Figs. 9, 10 can be seen in Figs. 11, 12, where only the π^0 signal was simulated.

It can be seen that the effects of the 1-C fit, prior to topological cuts, narrows the π^0 signal for events with beam energies less than 3.6 GeV, while for energies greater than 3.6 GeV, the 1-C fit reveals a signal that appears hidden without further cuts for the data.

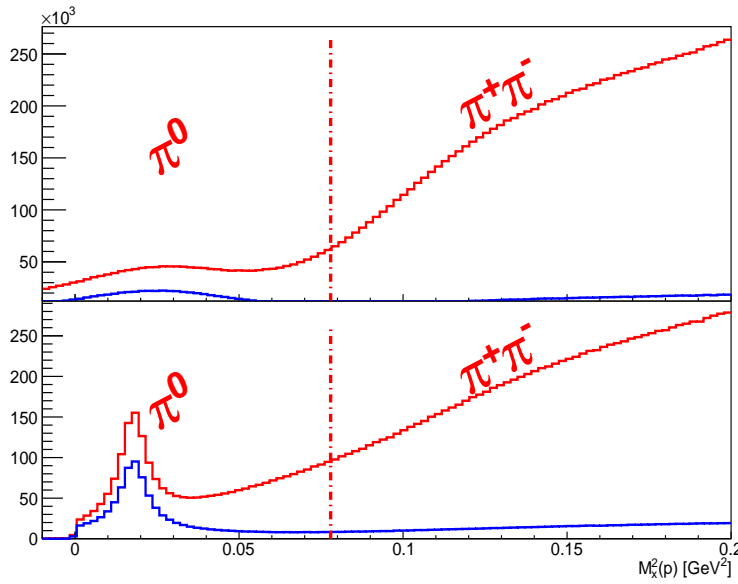


Figure 9: Number of data events plotted vs. squared missing mass $M_x^2(\gamma p \rightarrow pX)$ for uncut data and $E_\gamma < 3.6$ GeV. The top panel depicts the unfitted data, where the red data line represents all data while the blue line depicts all data with cuts placed on CC and EC. The bottom panel depicts the data output from the kinematic fitter 1-C fit, where the red data line represents all data while the blue line depicts all data with cuts placed on CC and EC. The vertical dashed-dotted line represents the threshold for $\gamma p \rightarrow p\pi^+\pi^-$ production.

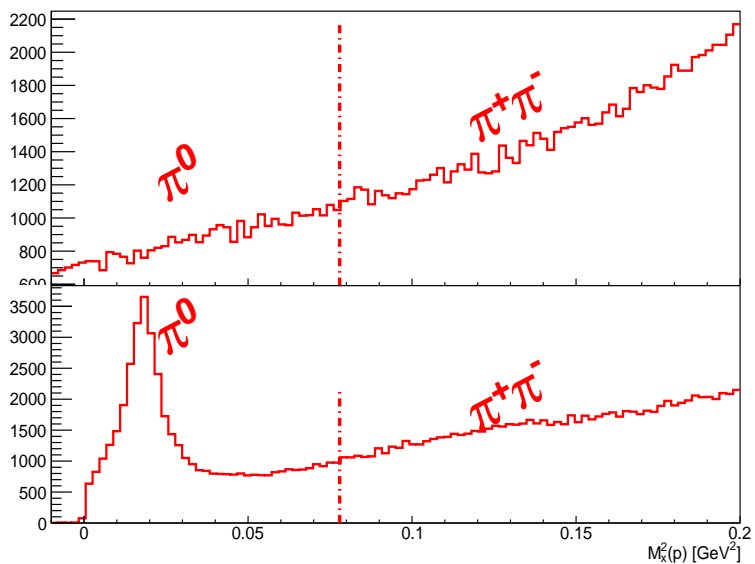


Figure 10: Number of data events plotted vs. squared missing mass $M_x^2(\gamma p \rightarrow pX)$ for uncut data and $E_\gamma > 3.6 \text{ GeV}$. The top panel depicts the unfitted data. The bottom panel depicts the data output from the kinematic fitter 1-C fit. The vertical dashed-dotted line represents the threshold for $\gamma p \rightarrow p\pi^+\pi^-$ production.

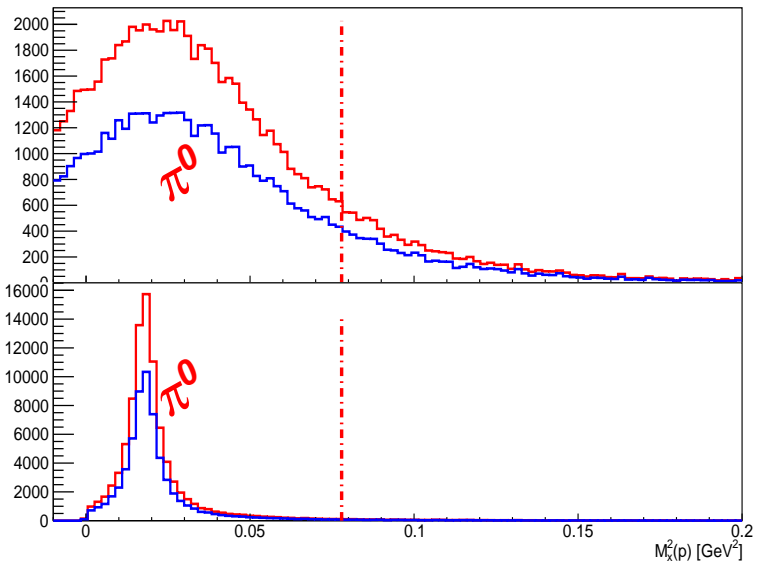


Figure 11: Number of MC events plotted vs. squared missing mass $M_x^2(\gamma p \rightarrow pX)$ for uncut data and $E_\gamma < 3.6$ GeV. The top panel depicts the unfitted data, where the red data line represents all data while the blue line depicts all data with cuts placed on CC and EC hits to be present. The bottom panel depicts the data output from the kinematic fitter 1-C fit, where the red data line represents all data while the blue line depicts all data with cuts placed on CC and EC hits to be present. The vertical dashed-dotted line represents the threshold for $\gamma p \rightarrow p\pi^+\pi^-$ production.

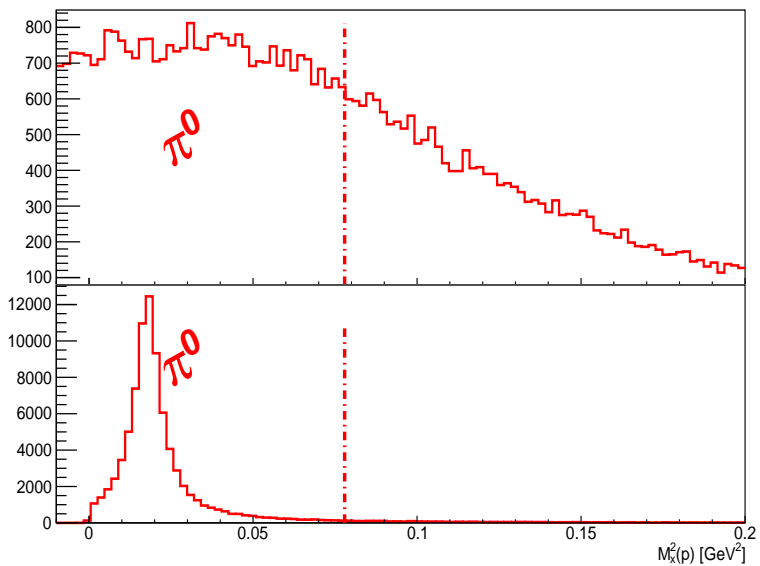
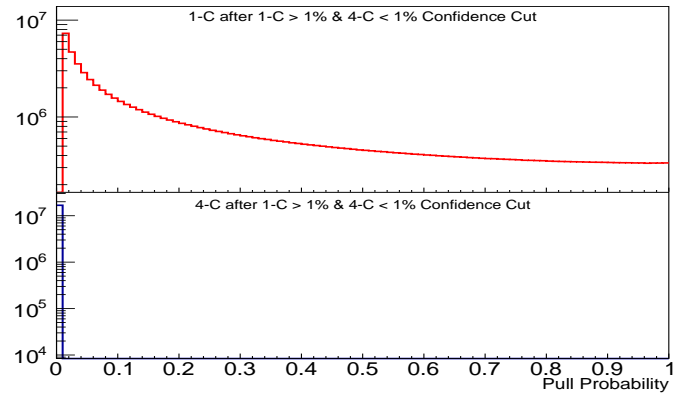


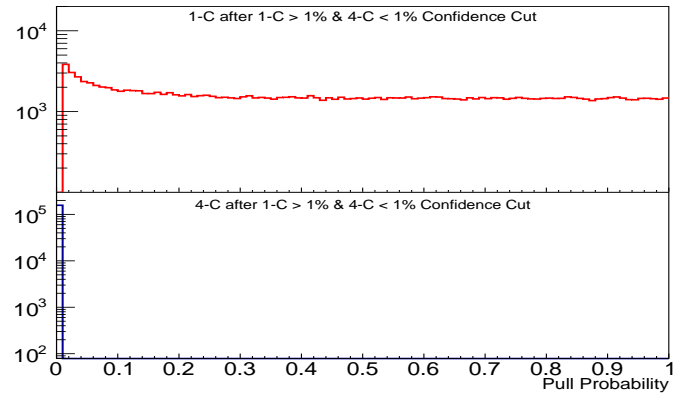
Figure 12: Number of MC events plotted vs. squared missing mass $M_x^2(\gamma p \rightarrow pX)$ for uncut data and $E_\gamma > 3.6$ GeV. The top panel depicts the unfitted data. The bottom panel depicts the data output from the kinematic fitter 1-C fit. The vertical dashed-dotted line represents the threshold for $\gamma p \rightarrow p\pi^+\pi^-$ production.

2.3.4 1-C & 4-C Cuts

As mentioned in Sec 2.3.2, there were 3 constraint equations used in this analysis. The 1-C fit utilizes a constraint equation to a missing photon, while the 4-C fit assumed a $\pi^+\pi^-$ topology instead of the e^+e^- topology. In this analysis a $>1\%$ confidence level cut was placed on the 1-C fit to ensure that a missing photon is in the event. However, a $<1\%$ confidence level cut was placed on the 4-C fit to remove the $\pi^+\pi^-$ background. The effect of the pull distributions after placing these cuts can be seen in Fig. 13. The effect of the 1-C and 4-C cut on the data can be seen in Fig. 14, where the blue line depicts the uncut fitted data spectrum, except the trigger cut, the black line depicts after a $>1\%$ cut placed on the 1-C and green line depicts the effect of the $<1\%$ 4-C fit cut. The top panel illustrates the effect of the cuts on recorded data, bottom panel illustrates the effect of the cuts on MC. The top plot of each panel depicts events of beam energies less than 3.6 GeV, while the bottom plot of each panel depicts events of beam energies greater than 3.6 GeV. It is shown in Fig. 14a that each cut reduces the background without significantly reducing the signal.



(a)



(b)

Figure 13: Number of events vs. Pull probability distributions after a 1% cut placed on the 1-C (top plots) and 4-C fit (middle plots) for data (a) and MC (b).

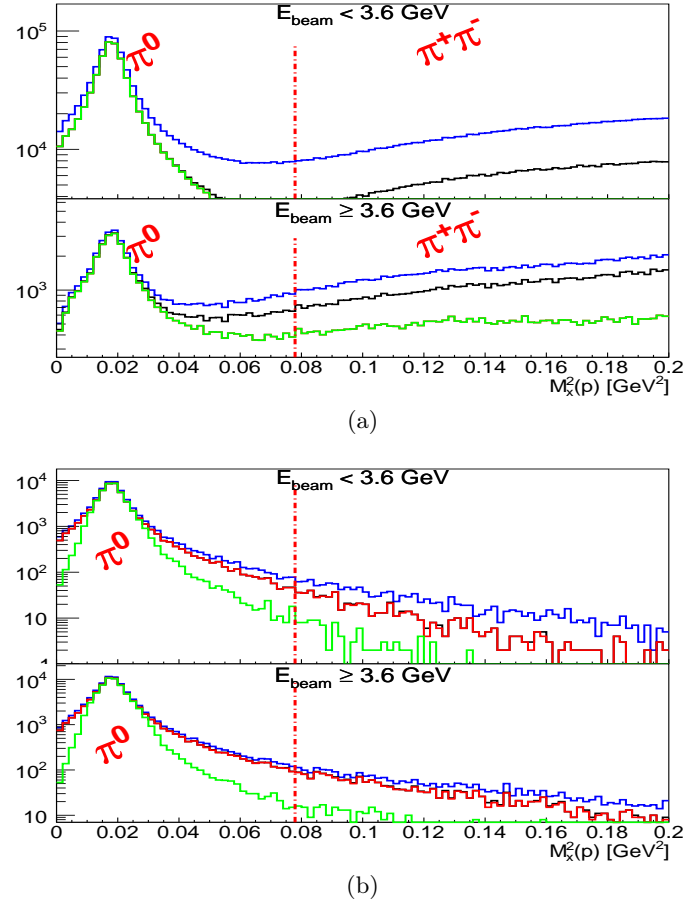


Figure 14: Number of data events plotted vs. squared missing mass $M_x^2(\gamma p \rightarrow pX)$. Blue lines depict the fitted data prior to pull distribution cuts, black line depicts after a 1% cut placed on the 1-C and green line depicts the effect of the 1% 4-C fit cut. Top panel (a) depicts data while bottom panel (b) depicts MC. The vertical dashed-dotted line represents the threshold for $\gamma p \rightarrow p\pi^+\pi^-$ production.

2.3.5 Missing Energy Cut

The remainder of the background can be attributed to $\pi^+\pi^-$ events. To reduce the background further, a comparison of the missing mass squared off of the proton and the pe^+e^- missing energy of the system was performed. This comparison is plotted in Fig. 15, where it can be seen that the majority of $\pi^+\pi^-$ background has missing energy less than 75 MeV. To eliminate this background all events with a missing energy less than 75 MeV were removed.

The effect of the 75 MeV missing energy cut on the $M_x^2(p)$ spectrum can be seen in Fig. 16. The signal function (red solid) is the *Crystal Ball Function* [17], [18] and the background (black) a 3rd order polynomial. The contamination of the background under the π^0 signal for data events where the beam energy is less than 3.6 GeV is 1.3 %. The contamination of the background under the π^0 signal for data events where the beam energy is greater than 3.6 GeV is 2.1 %. This background can be reduced more with the 2-C cut, Eq. 11, and is detailed in Sec. 2.3.6.

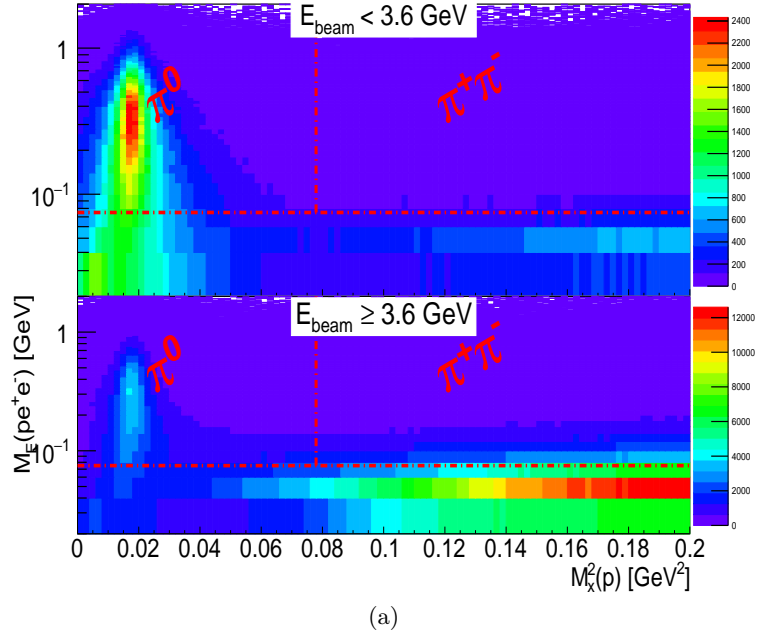
The Crystal Ball function, named after the Crystal Ball Collaboration, is a probability density function commonly used to model various lossy processes in high-energy physics. It consists of a Gaussian core portion and a power-law low-end tail, below a certain threshold. The function itself and its first derivative are both continuous [18].

$$f(x; \alpha, n, \bar{x}, \sigma) = N \cdot \begin{cases} \exp\left(-\frac{(x-\bar{x})^2}{2\sigma^2}\right), & \text{for } \frac{x-\bar{x}}{\sigma} > -\alpha \\ A \cdot (B - \frac{x-\bar{x}}{\sigma})^{-n}, & \text{for } \frac{x-\bar{x}}{\sigma} \leq -\alpha \end{cases} \quad (12)$$

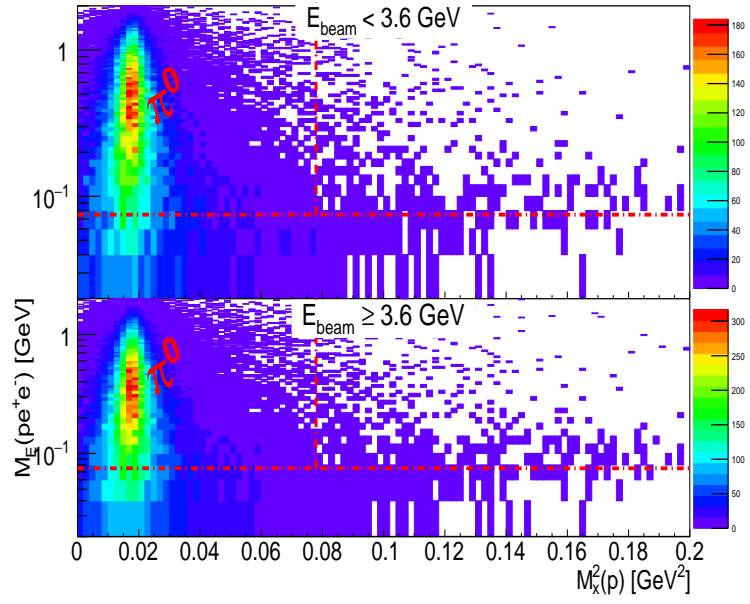
where

$$\begin{aligned} A &= \left(\frac{n}{|\alpha|}\right)^n \cdot \exp\left(-\frac{|\alpha|^2}{2}\right) \\ B &= \frac{n}{|\alpha|} - |\alpha| \end{aligned} \quad (13)$$

N is a normalization factor and α , n , x and σ are parameters which are fitted with the data.

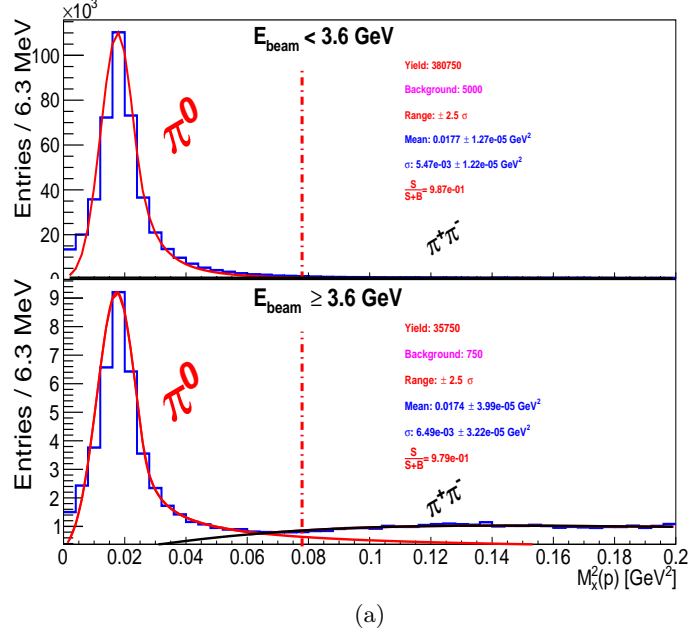


(a)

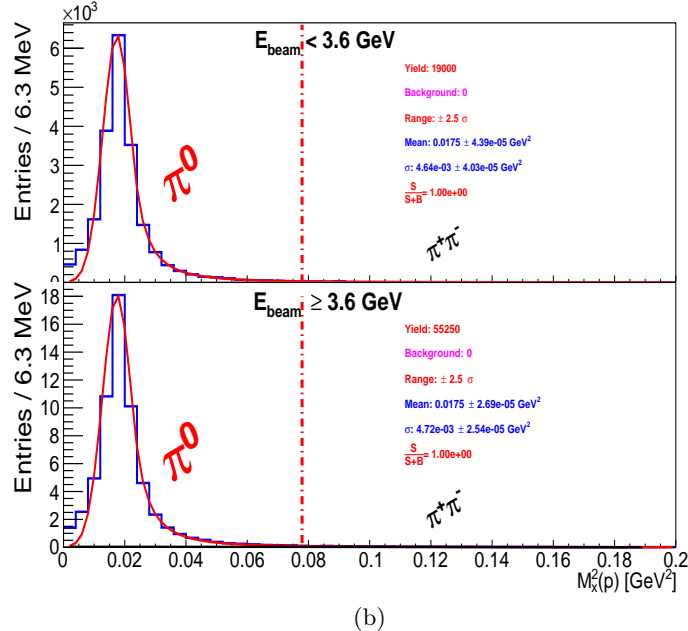


(b)

Figure 15: $M_x^2(p)$ vs. $M_E(pe^+e^-)$. The horizontal red dashed-dotted line depicts the 75 MeV cut used in this analysis. The vertical red dashed-dotted line depicts boundary of single π^0 to $\pi^+\pi^-$ production. Top panel (a) depicts data, while the bottom panel (b) depicts MC.



(a)



(b)

Figure 16: Number of data events plotted vs. missing mass $M_x^2(\gamma p \rightarrow pX)$ after the 1-C, 4-C and 75 MeV missing energy cut. Top plots (a) depicts the data. Bottom plot (b) depicts the MC. For both panels, the top plots illustrate events with beam energies less than 3.6 GeV, while the bottom plot illustrates events with beam energies greater than 3.6 GeV. The red solid line are fits using the *Crystal Ball Function*, while the black line illustrates the 3rd order polynomial background function. The vertical dashed-dotted line represents the threshold for $\gamma p \rightarrow p\pi^+\pi^-$ production.

2.3.6 2-C Cut

The final cut utilized in the analysis was the 2-C constraint. The 2-C constraint fits to a missing final state photon but also constrains the invariant mass squared of $e^+e^-(\gamma) = m_{\pi^0}^2$. The constraint equation for this 2-C fit is given in Eq. 11. This analysis used a $> 1\%$ confidence level cut on the 2-C fit, Fig. 17, this translates to a 2.5σ cut of a Gaussian function if a Gaussian was assumed for the signal instead of the *Crystal Ball Function*. The effect of the 2-C cut after the 1-C, 4-C and missing energy cut on the data can be seen in Fig. 18, where the top plot of each panel illustrates the mass spectrum prior to the $> 1\%$ 2-C cut and the bottom plot of each panel illustrates the mass spectrum after the $> 1\%$ 2-C cut along with the other cuts. To show the full effect of the 2-C fit, the bottom plot of each panel has the fits of their top plots superimposed. For events under 3.6 GeV in beam energy, the 2-C cut has little effect, which is expected because this spectrum presented itself almost background free due to the CC and EC trigger constraints. For events above 3.6 GeV in beam energy, the 2-C cut has greater effect, which is expected because this spectrum presented itself with more $\pi^+\pi^-$ background. The effect of the 2-C cut on MC, Fig. 19, is minimal as well due to the π^0 spectrum being the only topology simulated. The blue lines atop of the data spectrum for each plot in which the 2-C cuts were taken, shows the new fit using the *Crystal Ball Function*. The mass differences from the accepted value [15] to the fitted value are $3 \cdot 10^{-4}$ GeV 2 (≈ 1.2 MeV) and $4 \cdot 10^{-4}$ (≈ 1.7 MeV) for the events below 3.6 GeV and above 3.6 GeV respectively.

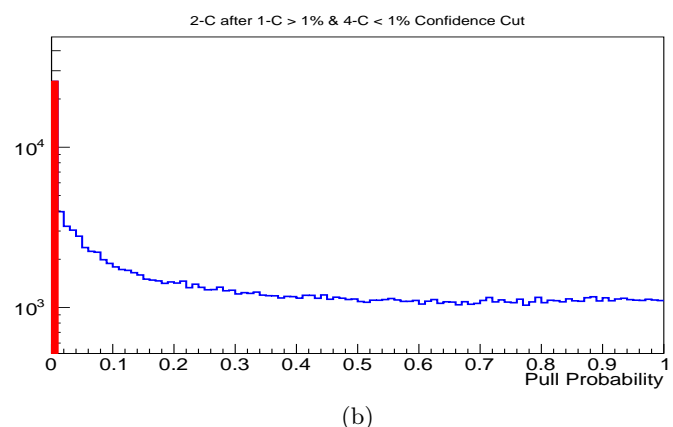
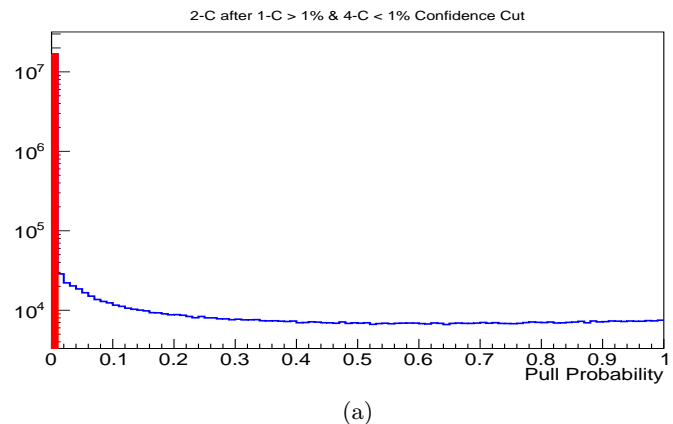
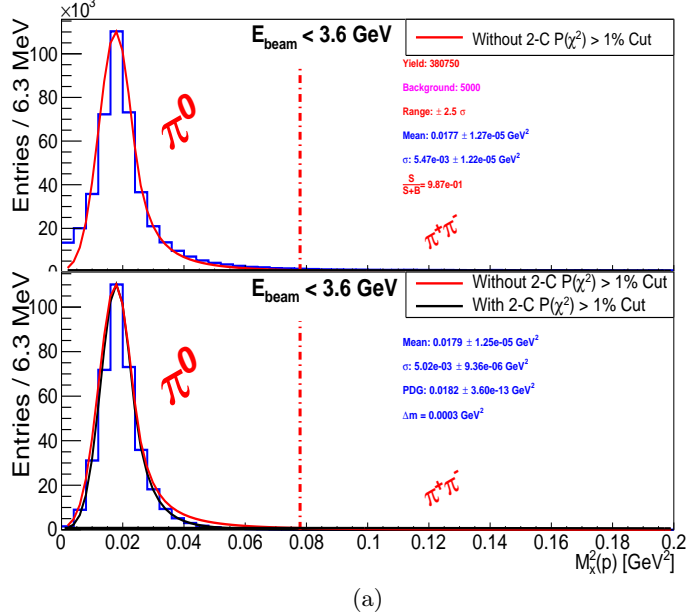
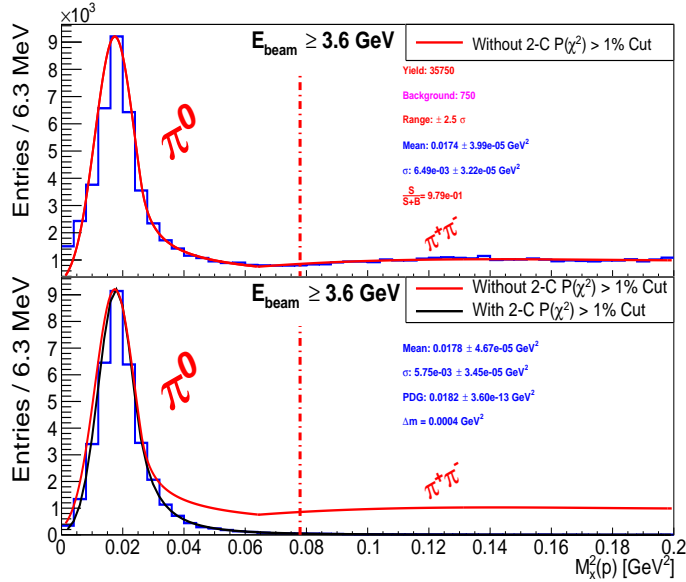


Figure 17: Number of events vs. 2-C Pull probability distributions after a 1% cut placed on the 1-C and 4-C fit for data (a) and MC (b). The red box in each plot depicts the 1% confidence level cut placed on the pull probability distribution.

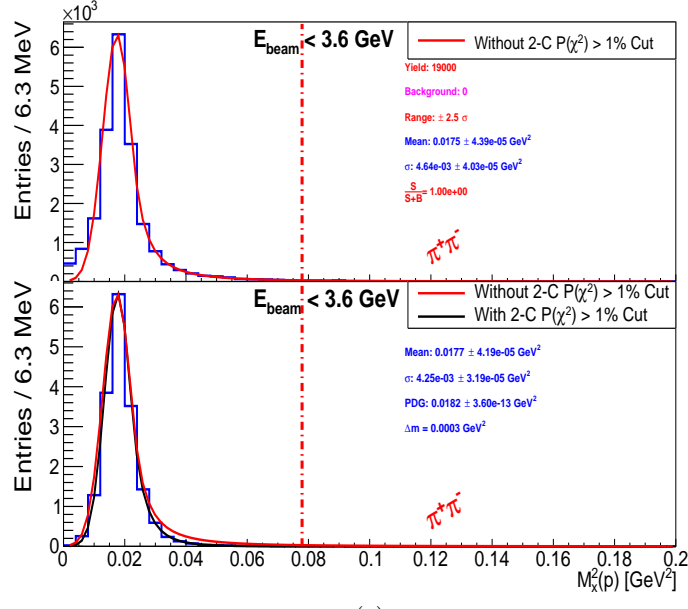


(a)

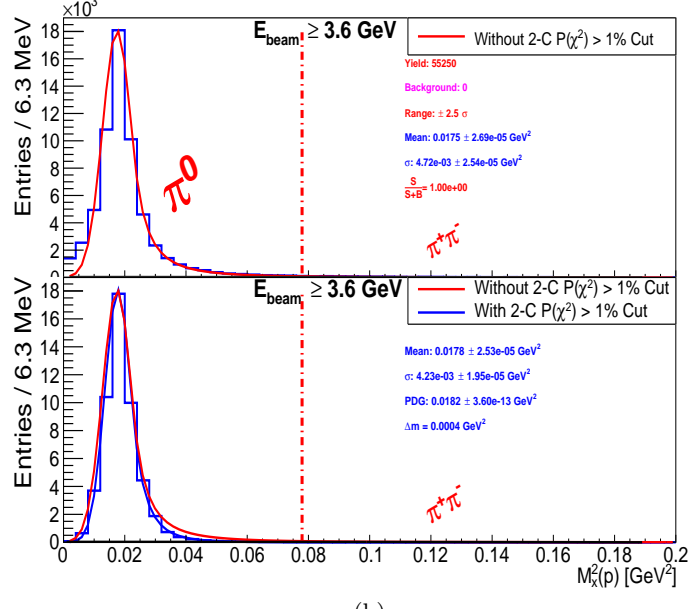


(b)

Figure 18: (Color Inline) Number of data events plotted vs. squared missing mass $M_x^2(\gamma p \rightarrow pX)$ after the 1-C, 4-C and 75 MeV missing energy cut. Top plots (a) illustrates events with beam energies less than 3.6 GeV. Bottom plots (b) illustrates events with beam energies greater than 3.6 GeV. The red solid line are fits using the *Crystal Ball Function* with a 3rd order polynomial background function. The bottom panels for both set of plots depict what the background and signal function parameters were without the 2-C cut for comparison. The vertical dashed-dotted line represents the threshold for $\gamma p \rightarrow p\pi^+\pi^-$ production.



(a)



(b)

Figure 19: (Color Inline) Number of MC events plotted vs. squared missing mass $M_x^2(\gamma p \rightarrow pX)$ after the 1-C, 4-C, 2-C and 75 MeV missing energy cut. Same notation as Fig. 18.

2.4 Particle Vertex Timing Cuts

Another quantity that is used for PID and data cleanliness is the vertex timing t_{vert} , which is the time the particle left the target. It can be calculated as;

$$t_{vert} = t_{\text{TOF}} - l_{\text{TOF}}/(c\beta) \quad (14)$$

where t_{TOF} and l_{TOF} are the time and length measurement, respectively, recorded at the TOF subsystem, and c is the speed of light. The value of β is calculated using the particles mass, m , and momentum, p , as measured from the DC. Therefore $\beta = \frac{p}{E} = \frac{p}{\sqrt{p^2+m^2}}$. Another means of calculating t_{vert} is to use the timing of the tagger hit using the RF-corrected tagger time, see tagger calibration in [14]. In this method t_{vert} is calculated as;

$$t_{vert} = t_{pho} + t_{prop} \quad (15)$$

where t_{pho} is the RF-corrected time that the photon crossed the center of the target and t_{prop} is the propagation time from the center of the target to the track's vertex. Comparing the two quantities of t_{vert} from Eq. 14 and Eq. 15 gives information of proper particle timing as well as the PID. In Fig. 20, the comparison of the difference $t_{(vert, \text{tagger})} - t_{(vert, \text{TOF})}$ is shown for the detected proton, e^- , and e^+ for data and MC after all geometric, TOF, EC fiducial cuts as well as all analysis cuts mentioned previously. A cut of ± 1.2 ns was placed on all particles, the effect is minimal.

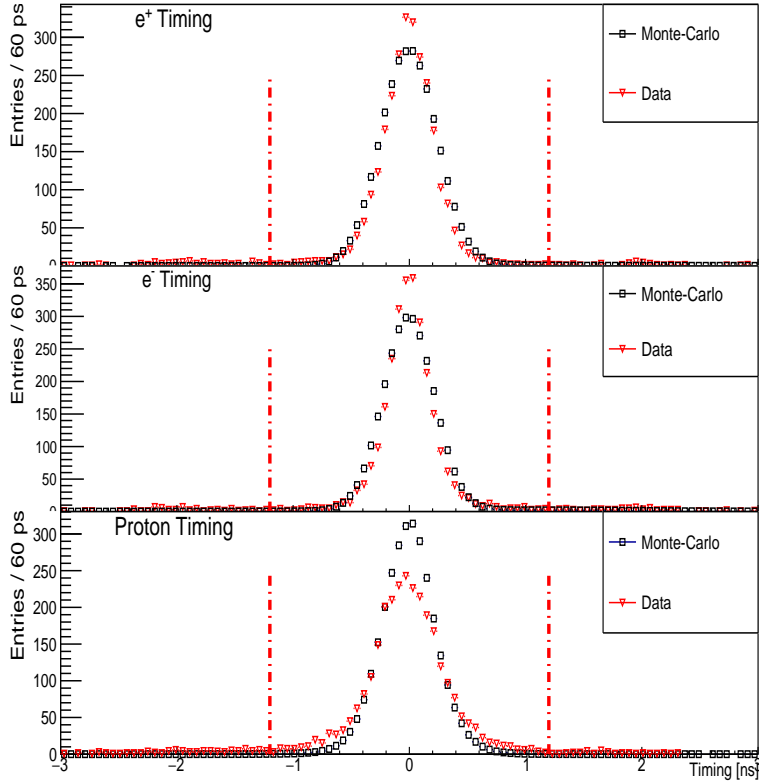


Figure 20: Number of events vs. $t_{pho} + t_{prop} - (t_{\text{TOF}} - l_{\text{TOF}}/(c\beta))$ for MC and data for proton, e^- , and e^+ . The vertical dashed-dotted lines represent the 1.2 ns cut placed on this quantity.

2.5 z Vertex Cuts

To ensure that π^0 production occurred on the ℓH_2 target, a cut was placed on the z -vertex position to be $-110 \leq z \leq -70$ cm Fig. 21. Since the vertex resolution of CLAS is 1 cm, there is a probability of π^0 production on the Kapton endcaps of the target. This effect was studied as a systematic uncertainty (see Sec 8.3). The z -vertex distribution is not flat because of acceptance. At large angles(backward) the acceptance in g12 was reduced to ≈ 100 degrees for single particle detection. For multi-particle detection, the acceptance, at large angles, was reduced to ≈ 70 degrees (see Fig. 22). For particles that originated from the target entrance, this acceptance effect was prominent. For π^0 production in g12, in which the decay of π^0 was identified with $e^+e^-(\gamma)$ events, the acceptance was largest when production occurred near the center of the target. When production happened in the downstream part of the target, the dilepton acceptance was reduced.

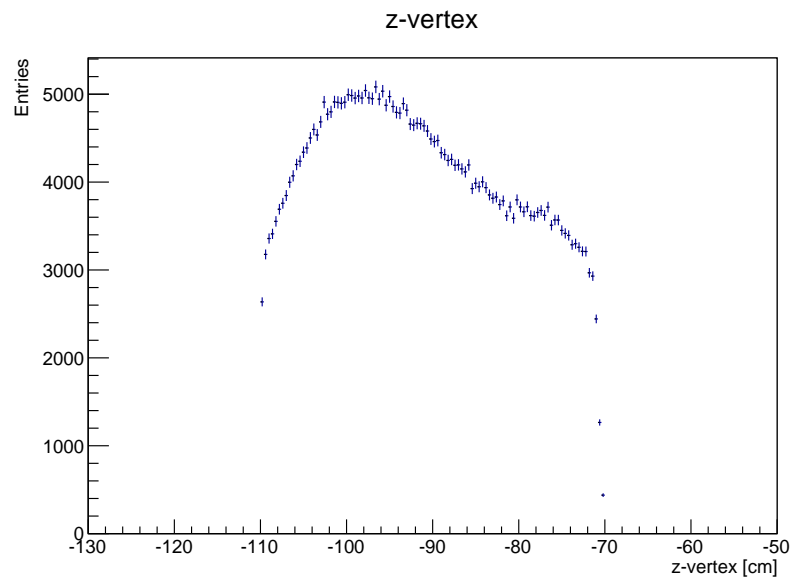


Figure 21: Number of data events plotted vs. z -vertex.

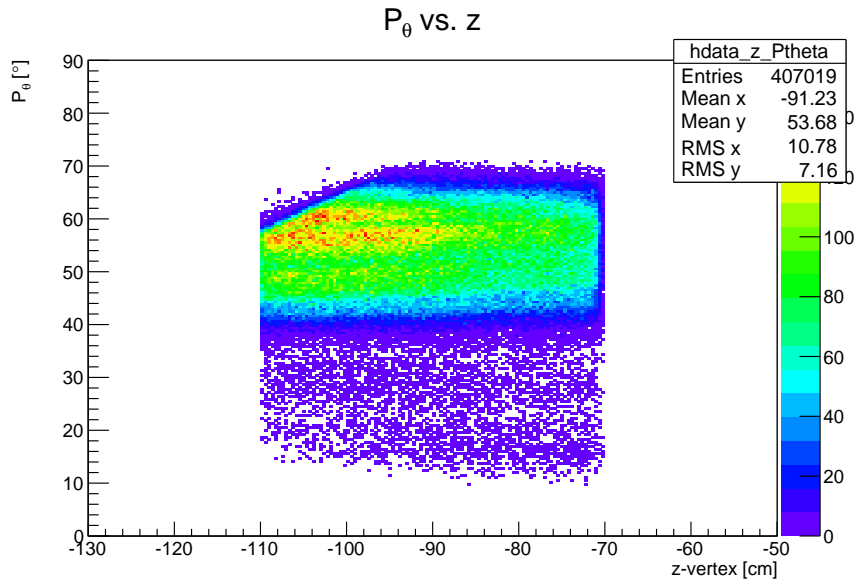


Figure 22: Proton θ vs. z -vertex. The z-axis depicts the total number of events.

2.5.1 Final MC Distribution

The final MC selection used for measuring of physics variables from π^0 production for this analysis can be seen in Fig. 23.

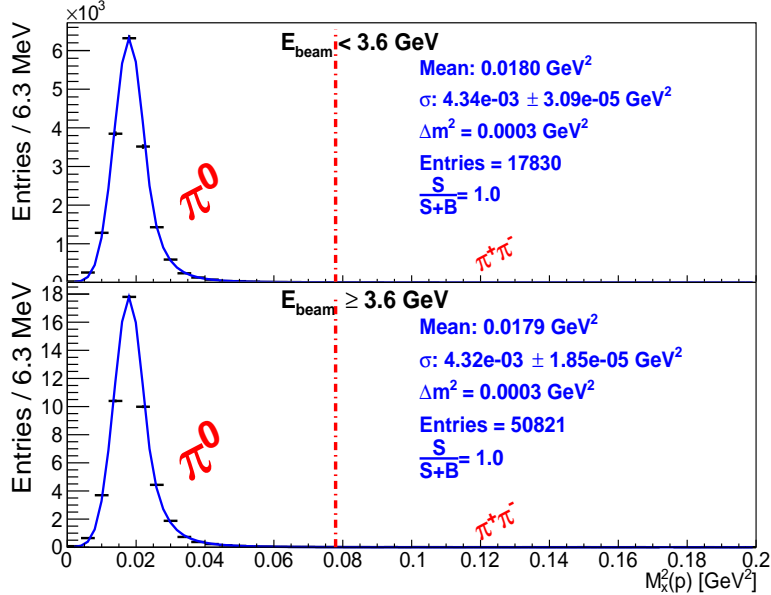


Figure 23: Number of MC events plotted vs. squared missing mass $M_x^2(\gamma p \rightarrow pX)$ for $\gamma p \rightarrow pe^+e^-(\gamma)$ events after all cuts and corrections. The vertical dashed-dotted line represents the threshold for $\gamma p \rightarrow p\pi^+\pi^-$ production.

2.5.2 Final Data Distribution

The final data selection used for measuring of physics variables from π^0 production for this analysis can be seen in Fig. 24. A table of fitted mass quantities for both data and MC can be see in Tab. 7

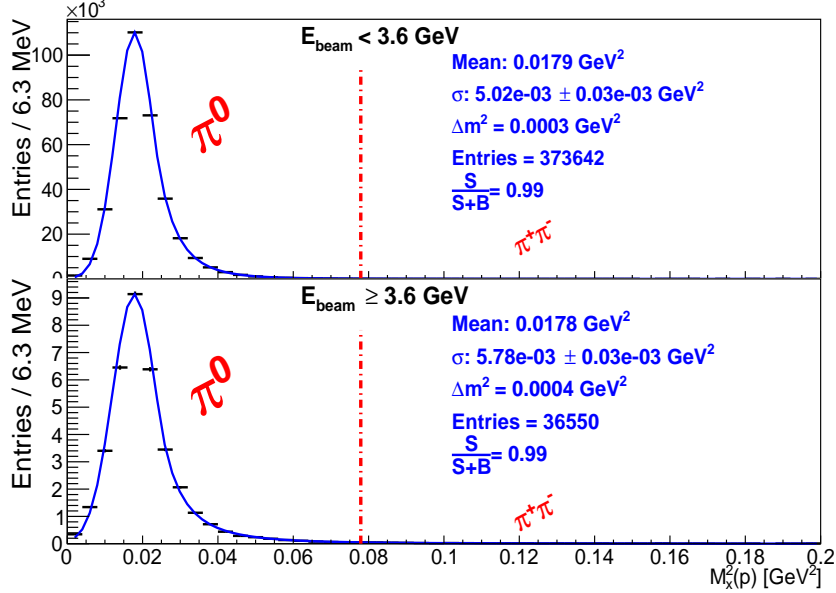


Figure 24: Number of data events plotted vs. squared missing mass $M_x^2(\gamma p \rightarrow pX)$ for $\gamma p \rightarrow pe^+e^-(\gamma)$ events after all cuts and corrections. The vertical dashed-dotted line represents the threshold for $\gamma p \rightarrow p\pi^+\pi^-$ production.

PDG mass	$E_\gamma < 3.6 \text{ GeV}$		$E_\gamma \geq 3.6 \text{ GeV}$	
	DATA	MC	DATA	MC
$1.349 \cdot 10^{-1} \text{ [GeV]}$				
$M_x^2(\gamma p \rightarrow pX) \text{ [GeV}^2]$	$1.788 \cdot 10^{-2}$	$1.795 \cdot 10^{-2}$	$1.779 \cdot 10^{-2}$	$1.790 \cdot 10^{-2}$
$\Delta M_x^2(\gamma p \rightarrow pX) \text{ [GeV}^2]$	$3.352 \cdot 10^{-4}$	$2.687 \cdot 10^{-4}$	$4.207 \cdot 10^{-4}$	$3.187 \cdot 10^{-4}$
$M_x(\gamma p \rightarrow pX) \text{ [GeV]}$	$1.337 \cdot 10^{-1}$	$1.339 \cdot 10^{-1}$	$1.334 \cdot 10^{-1}$	$1.338 \cdot 10^{-1}$
$\Delta M_x(\gamma p \rightarrow pX) \text{ [GeV]}$	$1.247 \cdot 10^{-3}$	$9.989 \cdot 10^{-4}$	$1.568 \cdot 10^{-3}$	$1.186 \cdot 10^{-3}$

Table 7: $M_x^2(\gamma p \rightarrow pX)$ fit values for entries used in $\frac{d\sigma}{d\Omega}$ measurement

2.6 Lepton Trigger Efficiency for π^0 Candidates

Using all π^0 candidates for incident beam energies less than 3.6 GeV in which satisfy the hit quantities of the CC and EC requirements outlined in Sec. 2.2.1

, a trigger analysis was performed to investigate the lepton trigger “bit 6” efficiency. The normalization is the total number of π^0 events as seen in the top panel of Fig. 24 in Sec. 2.5.2. The normalization is done by calculating the total number of entries for each trigger “bit” and normalizing by the total number of events. I.e., let us denote the total number of π^0 events with N . For each π^0 event, the trigger “bit” was looked at. The number of π^0 events with a valid “bit i ” entry, N_i is counted. The efficiency of the trigger “bit $_i$ ” is then calculated as: $\beta = N_i/N$. Since in the g12 trigger system there was no hierarchy in the trigger, i.e. no “bit” had a higher precedence, it is always possible that if “bit $_i$ ”, was triggered, that it could have been accompanied by other trigger hits. By counting all the valid π^0 events for which trigger “bit $_i$ ” was set and dividing this value to all the valid π^0 events, we determine in how many cases trigger “bit $_i$ ” should have been set but was not. Since we are going to use in this analysis only events with a valid “bit 6”, the important efficiency on Fig 25 is the one of that trigger bit. It can be seen in Fig 25 that for π^0 candidate events, below 3.6 GeV beam energy, the trigger “bit 6” efficiency 100%.

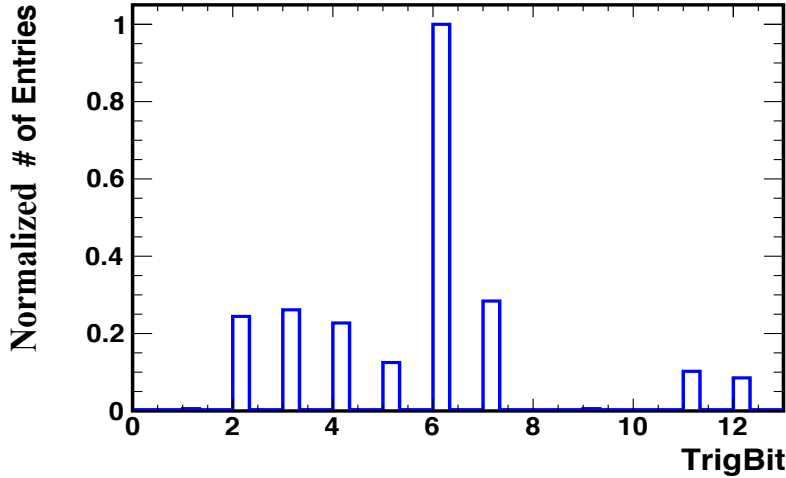


Figure 25: Normalized lepton trigger “bit 6” for π^0 candidates. The normalization is based upon the total number of π^0 candidates.

3 Target Density

We need to know the target density to calculate the differential cross-section. The procedure for determining the density of ℓH_2 target in CLAS has already

been established in [19] and is explained in Sec. 2.3 of [14].

4 Photon Normalization

In the calculation of the differential cross-section, Sec. 8, accuracy of the total number of photons incident on the target will determine the accuracy of the cross-section measurement. The procedure for determining the total number of photons in CLAS has already been established in [?] and is explained in Sec. 4 of [14]. A 25 MeV binning was chosen to compare past experiments differential cross-sections with this analysis.

It should be noted that beam energies with values 3.025 ± 25 MeV, 3.075 ± 25 MeV, 3.125 ± 25 MeV and 3.525 ± 25 MeV bins are excluded from the analysis due to flux calculation problems that arose from dead scintillators in the tagger.

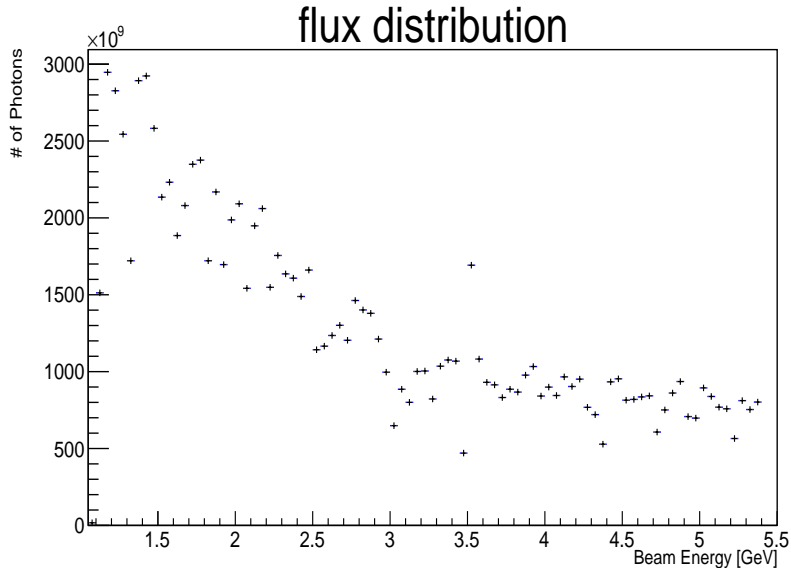


Figure 26: Photon flux for analysis.

5 Fiducial Cut

Fiducial cuts for g12 were derived and appropriately described in [14]. For this analysis, fiducial cuts were performed prior the the application of the track efficiency described in Sec. 6.

6 Normalization

6.1 Normalization History

In the g11 experiment there is an 18% discrepancy between the differential cross-sections of $\gamma p \rightarrow p\omega$ measured channels $\gamma p \rightarrow p\pi^+\pi^-(\pi^0)$ and $\gamma p \rightarrow p\pi^+(\pi^-\pi^0)$. One method of correction for this effect was to apply a global scale factor to the two track topology. The scale factor was on the order of 18%. The cause of the inefficiency was unknown but is believed to be due to the high current of the electron beam in conjunction with requiring 3 charged tracks from a 2-prong trigger.

6.2 g12 Normalization Procedure

In this analysis, a normalization constant on the order of 18% was also needed. The cause of this effect is unknown, but it is also believed to be related to using 3 charged tracks from 2-prong triggers at high current. GPP is responsible for smearing and dropping inefficient parts of the detector but not trigger efficiency. Therefore the normalization could be simulated if it was a trigger effect or another happenstance related to requiring 3 charged tracks in the analysis. To investigate this effect the following 3 topologies;

$$\begin{aligned} \gamma p &\rightarrow p\pi^+(\pi^-) \\ \gamma p &\rightarrow p\pi^-(\pi^+) \\ \gamma p &\rightarrow \pi^+\pi^-(p) \end{aligned} \quad (16)$$

were skimmed from data and simulated using the prescription chain in Sec. 7. In order to eliminate any statistical effects, $\frac{1}{4}$ of the entire g12 data set was used and over 1 billion events were generated for simulation. Table 8 lists the number of events analyzed for each of the topologies listed in Eq. 16.

Topology	Data Reconstructed	Monte-Carlo Generated/Reconstructed
$\gamma p \rightarrow p\pi^+(\pi^-)$	$5.09 \cdot 10^{10}$	$1.2 \cdot 10^9 / 2.16 \cdot 10^8$
$\gamma p \rightarrow p\pi^-(\pi^+)$	$5.43 \cdot 10^{10}$	$1.2 \cdot 10^9 / 2.17 \cdot 10^8$
$\gamma p \rightarrow \pi^+\pi^-(p)$	$5.34 \cdot 10^{10}$	$1.2 \cdot 10^9 / 1.08 \cdot 10^8$

Table 8: Number of Events Used in Efficiency Study

The data had two orders of magnitude higher statistics than the simulation, this was done to ensure enough events to analyze in the high momentum spectrum. The simulation generated the listed reactions in phase space using PLUTO++ [20]. The data and simulation were analyzed in the same manner.

The data was skimmed under the conditions of Eq. 16. If the missing particle (particle in parenthesis) was detected, then this information was also recorded. After the data was skimmed, kinematic fits (1-C) were performed to the missing particles. Nominal geometric fiducial cuts were employed for all detected particles along with a pull probability for each topology $> 1\%$, see Fig. 27.

Pull Probabilities for Normalization Study

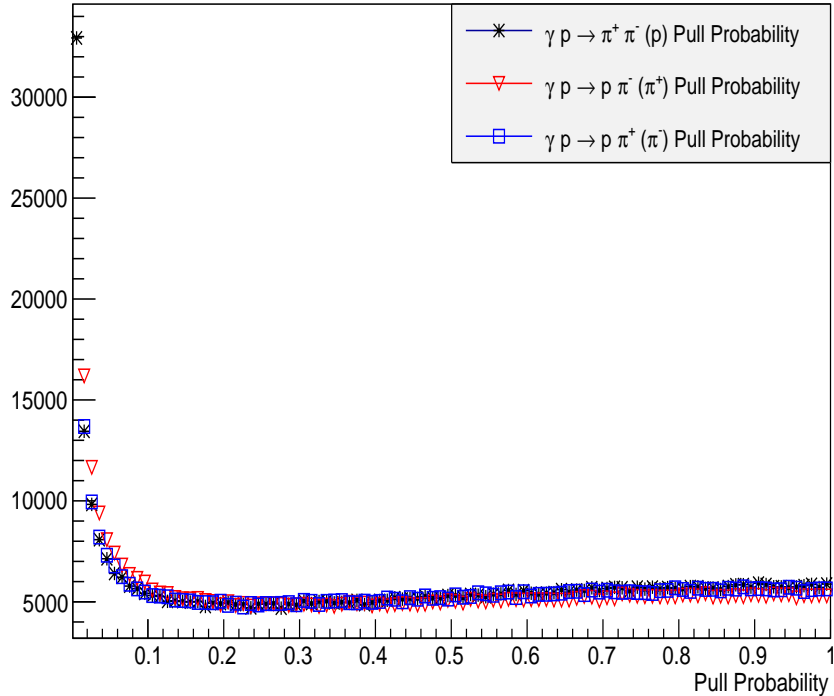


Figure 27: Number of events vs. the 1-C pull probability distribution for the reactions used in the normalization study for data.

The z-vertex of the two needed particles was determined by the method of distance of closest approach of the two vectors. The data was then binned for the fitted missing particle according to the z-vertex position, momentum, $\theta \sin \phi$, and $\theta \cos \phi$. The z-vertex and momentum binning used can be seen in Table 9. If the particle to be fit was detected by CLAS, the information was also binned according z-vertex, momentum, $\theta \sin \phi$, and $\theta \cos \phi$. However to ensure that the detected particle and the fitted missing particle were the same, the detected particle must have been in the same momentum bin as the fitted missing particle.

Pull Probabilities for Normalization Study for Monte-Carlo

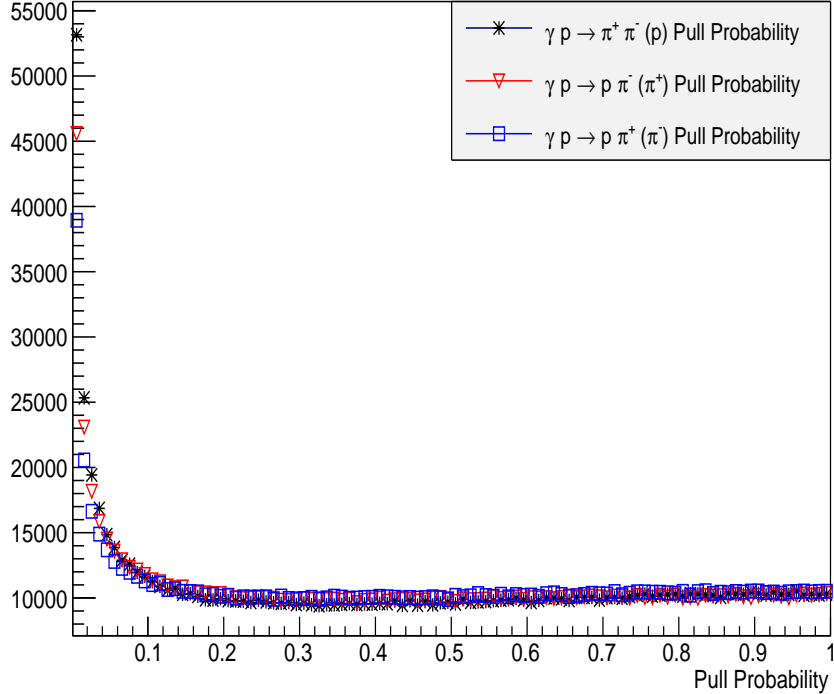


Figure 28: Number of events vs. the 1-C pull probability distribution for the reactions used in the normalization study for MC.

z bins [cm] (5 cm increments)	Momentum bins [GeV]
	0 - 0.5
	0.5 - 0.75
	0.75 - 1
$-70 \text{ cm} < z < -110 \text{ cm}$	1 - 1.5
	1.5 - 2
	2 - 2.5
	2.5 - 3
	3 - 5

Table 9: Binning Used in the Efficiency Study.

The $\theta \sin \phi$ and $\theta \cos \phi$ binning was chosen to interpret the geometric x and y space the particle travels, independent of momentum and x and y vertex. These $\theta \sin \phi$ and $\theta \cos \phi$ quantities are plotted as x and y variable of a histogram. To better illustrate this interpretation consider a spherical

coordinate system where;

$$r = \sqrt{x^2 + y^2 + z^2} \quad (17)$$

$$x = r \sin \theta \cos \phi \quad (18)$$

$$y = r \sin \theta \sin \phi \quad (19)$$

therefore,

$$\theta \sin \phi = \left(\frac{\theta}{r \sin \theta} \right) y \quad (20)$$

$$\theta \cos \phi = \left(\frac{\theta}{r \sin \theta} \right) x . \quad (21)$$

It can be seen that plotting Eq 21 versus Eq 20 projects $x - y$ space.

For each type of missing particle, we plotted the number of events versus $\theta \sin \phi$ and $\theta \cos \phi$. We then plotted the number of events where the “missing” particle was detected. The ratio of the number of detected “missing” particle to the total number of “missing” particles is the detection efficiency for that bin in z -vertex, p , $\theta \sin \phi$ and $\theta \cos \phi$ (see Figs 29, 32 and 35). This process was repeated for simulated data (see Figs 30, 33 and 36). The ratio of the simulated efficiency to the measured efficiency for each particle was used to correct the data (see Figs 31, 34 and 37). This procedure revealed any differences between the real and simulated detector responses.

6.3 g12 Normalization Results

It was noticed that the simulation was over-efficient as compared to the data and the ratio of the efficiency of reconstruction should suffice as a correction to the data. Figures 29, 32, 35 depict the efficiency of data reconstruction for the proton π^+ and π^- respectively. Figures 30, 33, 36 depict the efficiency of the simulation reconstruction for the proton π^+ and π^- respectively. Figures 31, 34, 37 depict the over-efficiency of the simulation to data reconstruction for the proton π^+ and π^- respectively. The total over-efficiency was calculated as the product of each track’s over-efficiency, i.e.,

$$\epsilon = \epsilon_{proton} \cdot \epsilon_{\pi^+} \cdot \epsilon_{\pi^-} . \quad (22)$$

The value of ϵ from Eq. 22 is the same quantity used in the cross-section calculation in Eq. 26.

Proton Data Efficiency at $-90. < z < -85.$ cm at $0.75 < P < 1$ GeV

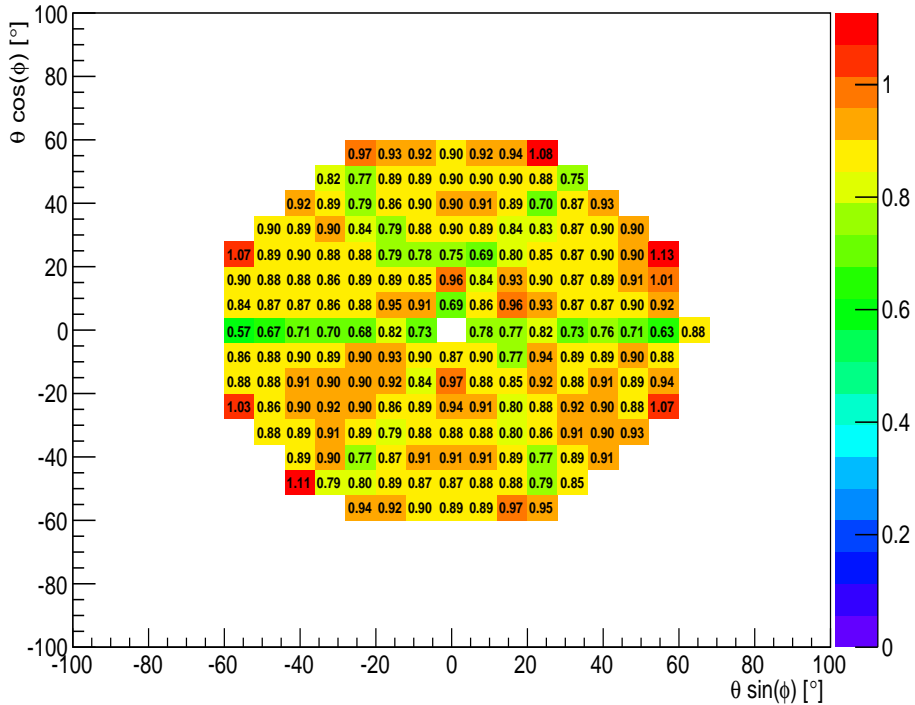


Figure 29: $\theta \cos \phi$ vs. $\theta \sin \phi$ plot showing the efficiency of detecting the proton with z-vertex $-90 < z < -85$ cm and momentum $0.75 < p < 1$ GeV from a 2 charged track reaction using CLAS detection for g12.

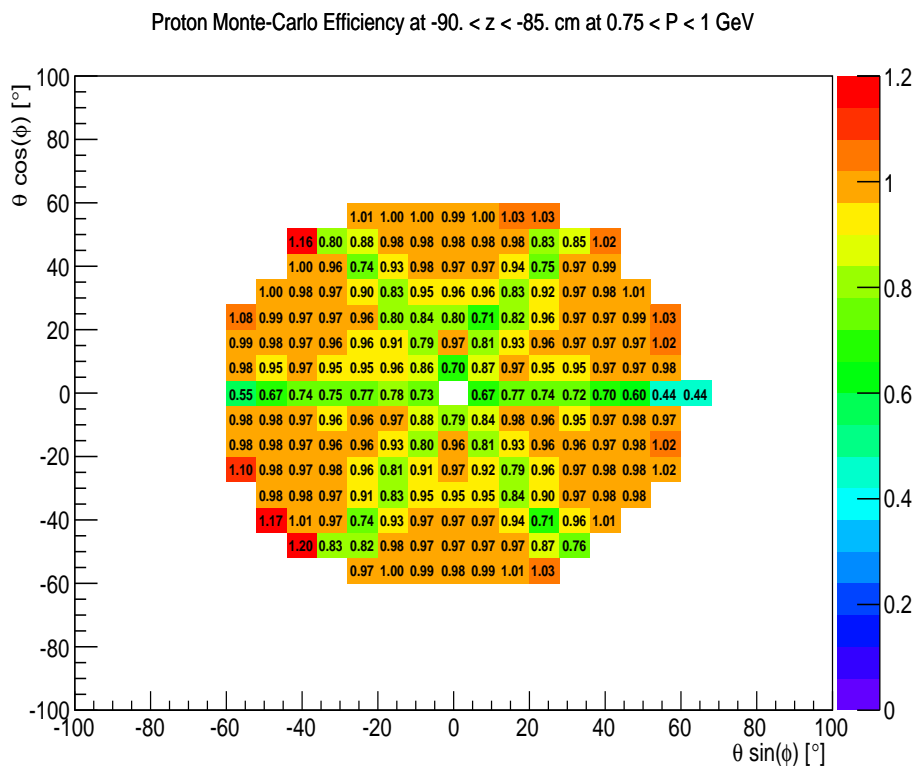


Figure 30: $\theta \cos \phi$ vs. $\theta \sin \phi$ plot showing the efficiency of reconstructing the proton with z-vertex $-90 < z < -85$ cm and momentum $0.75 < p < 1$ GeV from a 2 charged track reaction using CLAS Monte-Carlo for g12.

Proton Over-Efficiency at $-90 < z < -85$ cm at $0.75 < p < 1$ GeV

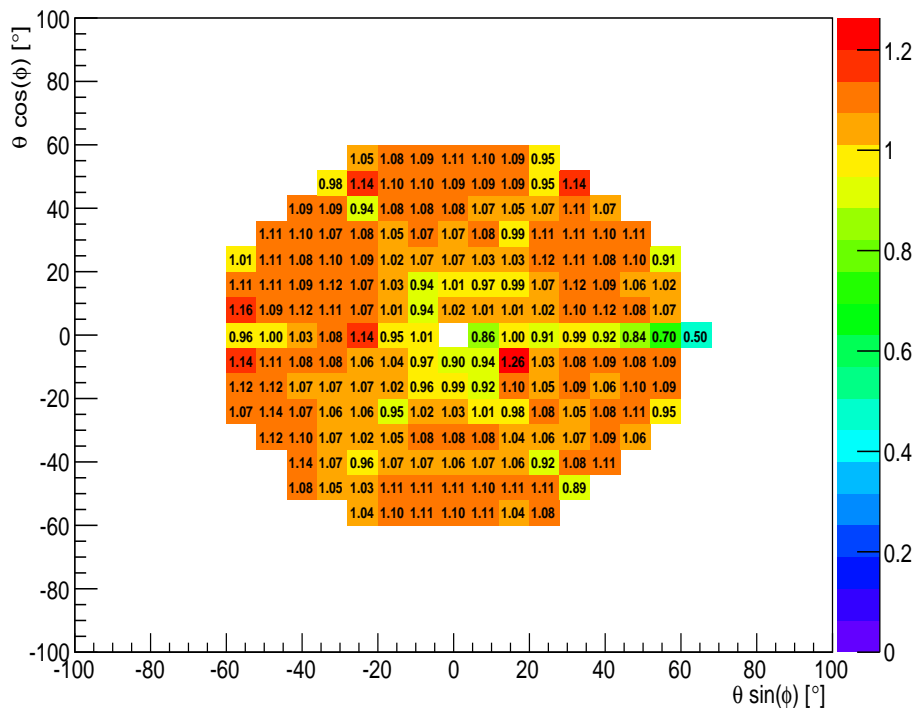


Figure 31: $\theta \cos \phi$ vs. $\theta \sin \phi$ plot showing the over-efficiency of simulating the proton with z-vertex $-90 < z < -85$ cm and momentum $0.75 < p < 1$ GeV from a 2 charged track reaction.

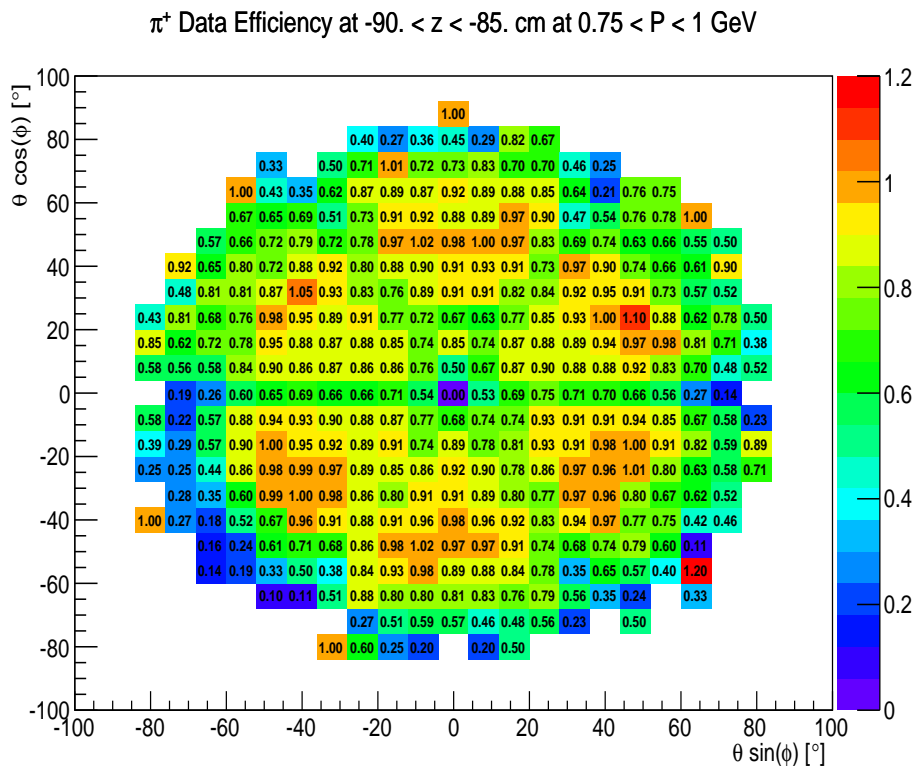


Figure 32: $\theta \cos \phi$ vs. $\theta \sin \phi$ plot showing the efficiency of detecting the π^+ with z-vertex $-90 < z < -85$ cm and momentum $0.75 < p < 1$ GeV from a 2 charged track reaction using CLAS detection for g12.

π^+ Monte-Carlo Efficiency at $-90^\circ < z < -85^\circ$ cm at $0.75 < p < 1$ GeV

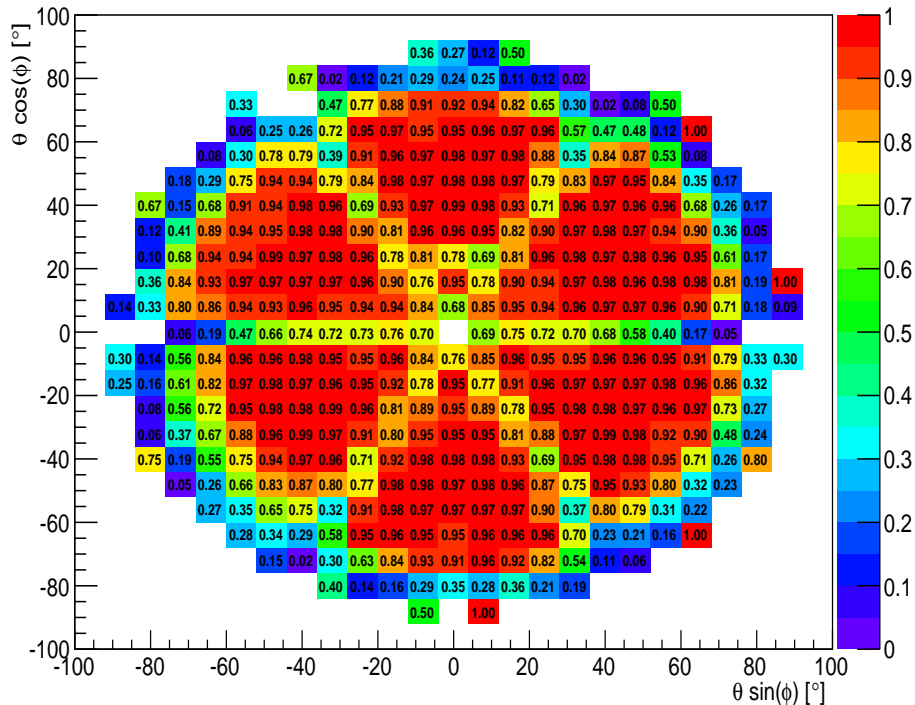


Figure 33: $\theta \cos \phi$ vs. $\theta \sin \phi$ plot showing the efficiency of reconstructing the π^+ with z-vertex $-90^\circ < z < -85^\circ$ cm and momentum $0.75 < p < 1$ GeV from a 2 charged track reaction using CLAS Monte-Carlo for g12.

π^+ Over-Efficiency at $-90. < z < -85.$ cm at $0.75 < P < 1$ GeV

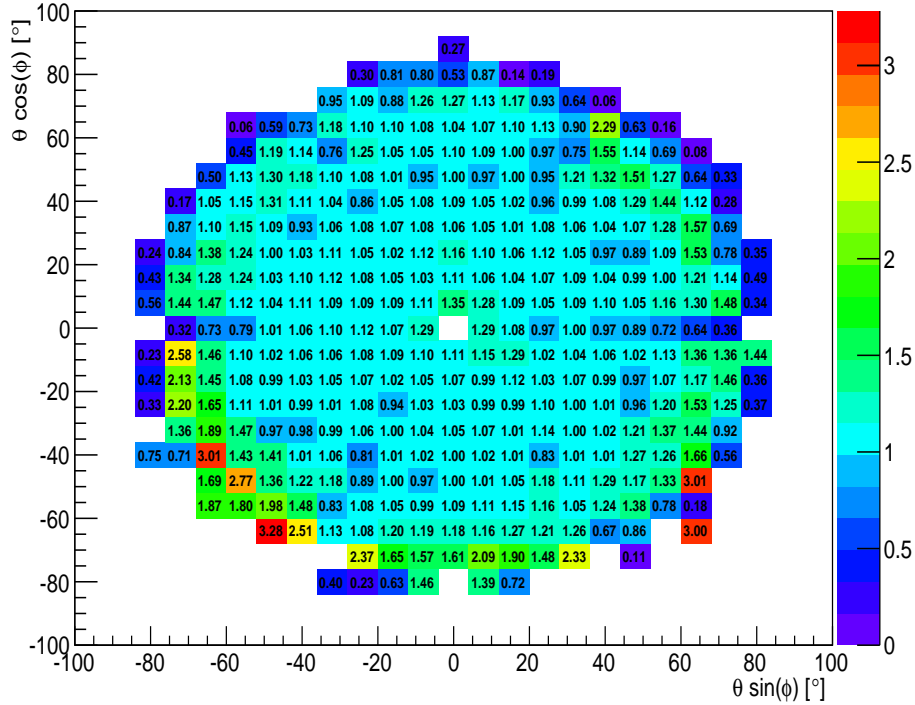


Figure 34: $\theta \cos \phi$ vs. $\theta \sin \phi$ plot showing the over-efficiency of simulating the π^+ with z-vertex $-90 < z < -85$ cm and momentum $0.75 < p < 1$ GeV from a 2 charged track reaction.

π^- Data Efficiency at $-90. < z < -85.$ cm at $0.5 < P < 0.75$ GeV

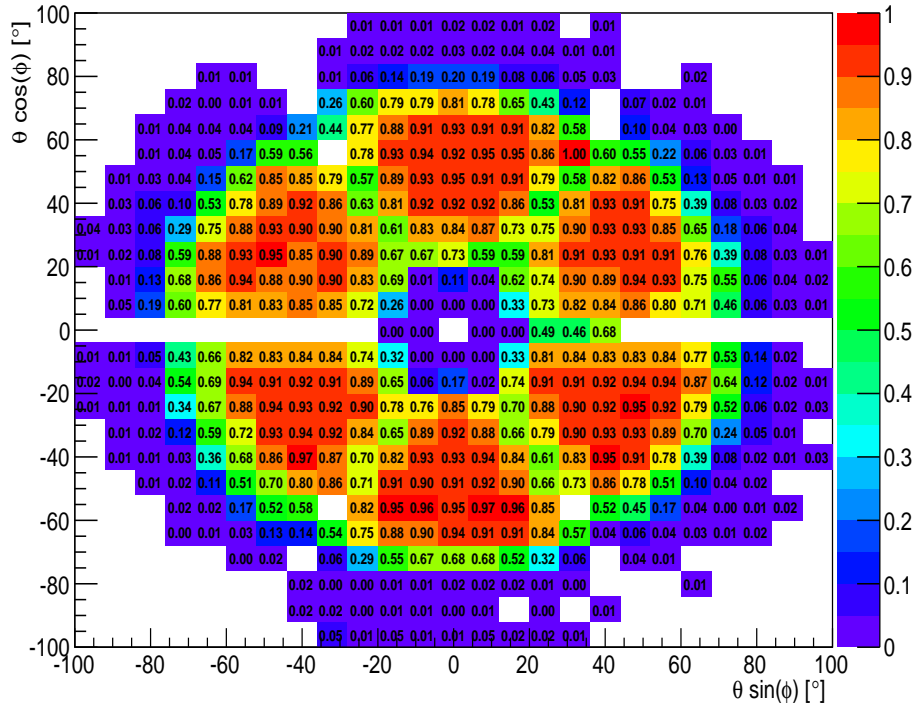


Figure 35: $\theta \cos \phi$ vs. $\theta \sin \phi$ plot showing the efficiency of detecting the π^- with z-vertex $-90 < z < -85$ cm and momentum $0.75 < p < 1$ GeV from a 2 charged track reaction using CLAS detection for g12.

π^- Monte-Carlo Efficiency at $-90 < z < -85$ cm at $0.5 < P < 0.75$ GeV

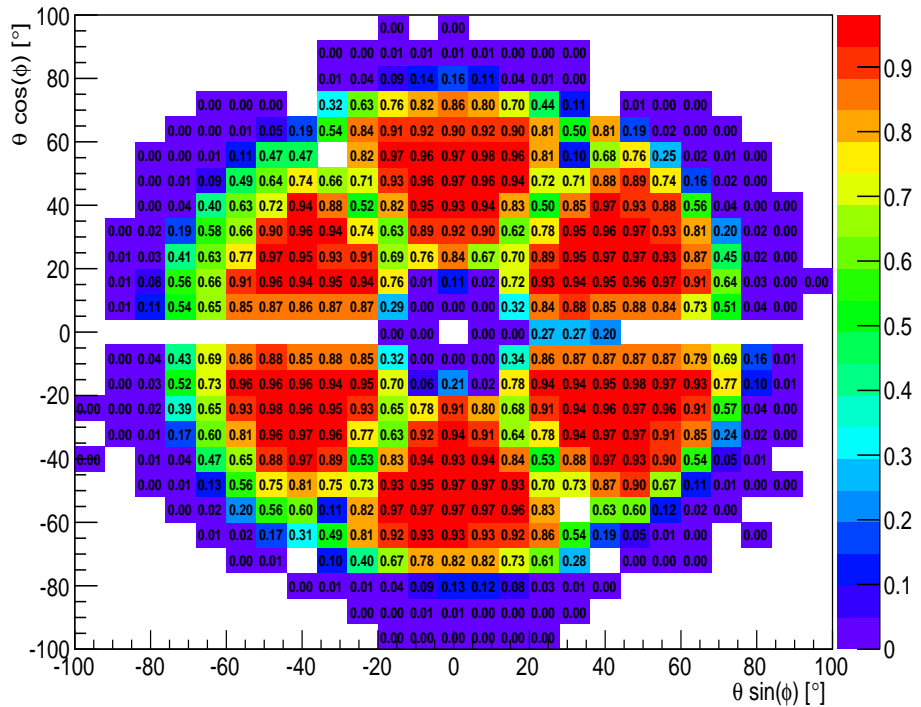


Figure 36: $\theta \cos \phi$ vs. $\theta \sin \phi$ plot showing the efficiency of reconstructing the π^- with z-vertex $-90 < z < -85$ cm and momentum $0.75 < p < 1$ GeV from a 2 charged track reaction using CLAS Monte-Carlo for g12.

π^- Over-Efficiency at $-90 < z < -85$ cm at $0.5 < P < 0.75$ GeV

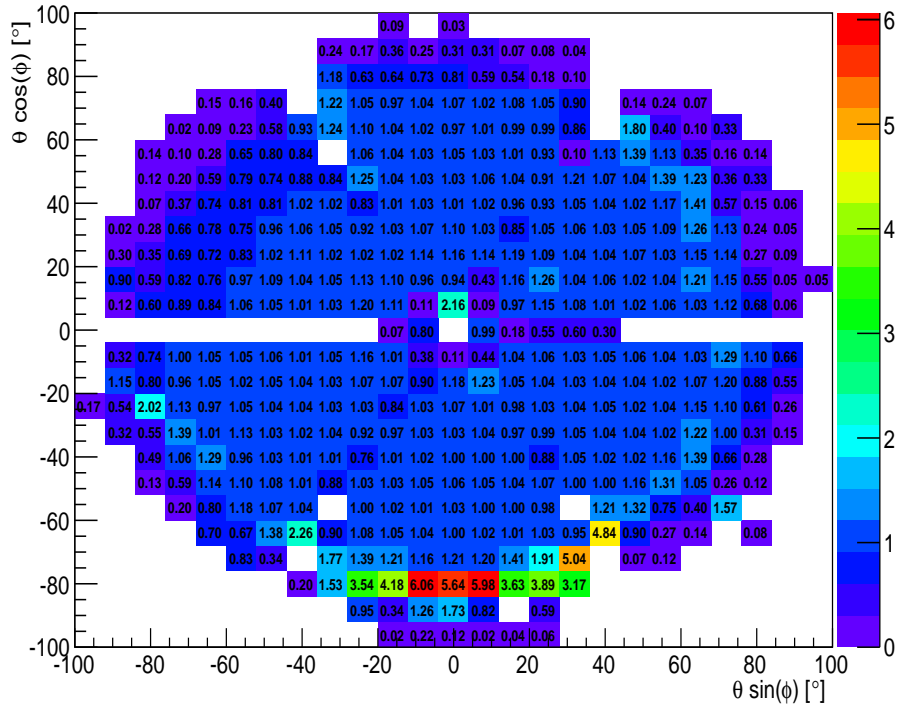


Figure 37: $\theta \cos \phi$ vs. $\theta \sin \phi$ plot showing the over-efficiency of simulating the π^- with z-vertex $-90 < z < -85$ cm and momentum $0.75 < p < 1$ GeV from a 2 charged track reaction.

6.4 Normalization Comparison

To validate the g12 normalization results, the g12 π^0 differential cross-section was calculated using the G11 global normalization factor and then compared to the g12 π^0 differential cross-section using the g12 normalization procedure results. It is shown in Fig. 38 and Fig. 39 that the 2 methods agree with one another except for the very forward regions of $\cos \theta_{C.M.}^{\pi^0}$, where the cross-section using the dynamic normalization is larger than the cross-section measured with the G11 global normalization, however the larger cross-sections at forward $\cos \theta_{C.M.}^{\pi^0}$ agree very well with the past results of [21].

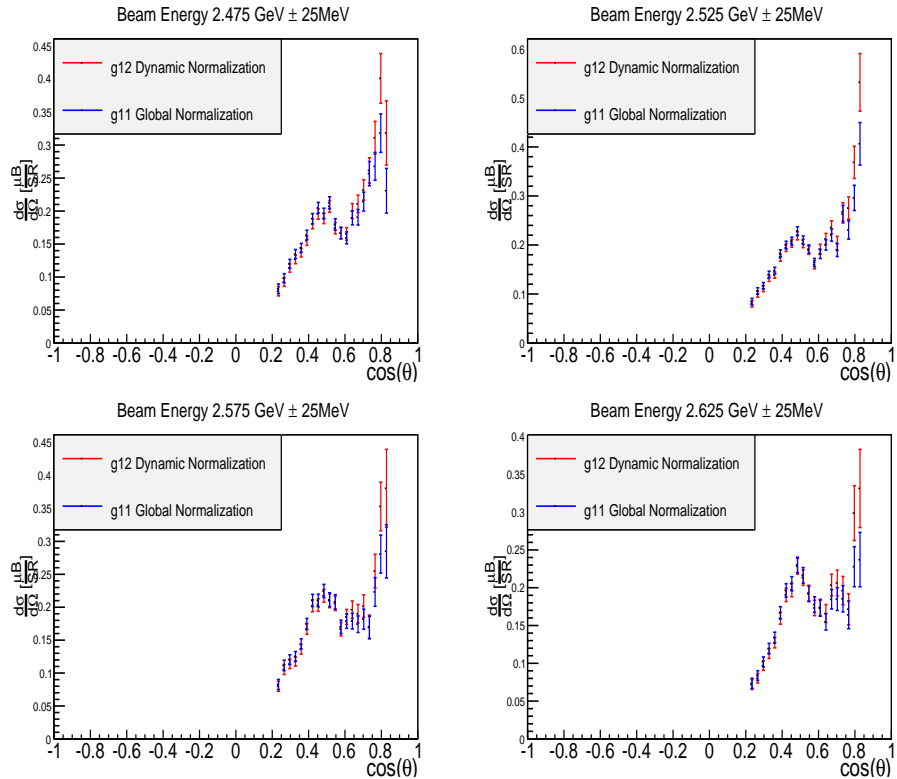


Figure 38: $\frac{d\sigma}{d\Omega}$ vs. $\cos \theta$ plot showing the g12 π^0 differential cross-section when the G11 global normalization is used (blue) and when the g12 dynamic normalization is used (red) for various bins of beam energy inside the lepton trigger acceptance.

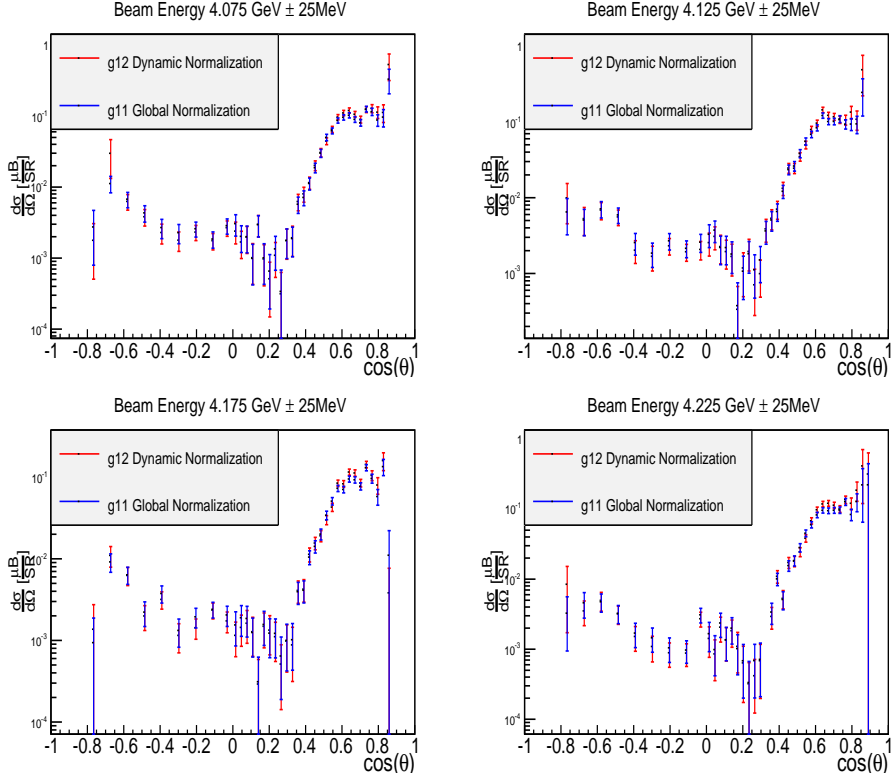


Figure 39: $\frac{d\sigma}{d\Omega}$ vs. $\cos \theta$ plot showing the $g_{12} \pi^0$ differential cross-section when the G11 global normalization is used (blue) and when the g_{12} dynamic normalization is used (red) for various bins of beam energy above the MORB threshold.

6.5 Normalization Uncertainties

The statistical uncertainties of the normalization correction was minimized by ensuring that the statistical sample of the data and MC was sufficient in each bin of z -vertex, momentum, $\theta \sin \phi$ and $\theta \cos \phi$. The maximum statistical uncertainty was 0.01%. The systematic uncertainties of the normalization correction was calculated and shown in Sec. 8.3.7.

7 Simulation

There are certain kinematic regions of CLAS in which physics events are not recorded properly, i.e. the area dividing each sector in CLAS. Furthermore each sector in CLAS is asymmetric in the acceptance of events due to subsystem inefficiencies such as inoperable DC wires, PMT inefficiencies, dead scintillator strips the the TOF and ST subsystems. When a triggered

event is recorded and reconstructed these asymmetric inefficiencies factors are reflected and must be carefully understood because these factors are properties of the CLAS detector and independent of any physics that occurred. To properly understand the detector effects on the data, CLAS utilizes a GEANT simulation package known as GSIM. To prepare an event for GSIM the program GAMP2PART converts a text file, containing the 4-momentum of the generated event, into a suitable file format for GSIM. GSIM then simulates the passage of these particles through the CLAS detector and generates the associated ADC and TDC information from detector hits. GSIM takes into account detector inefficiencies described in the CLAS_CALDB_RUNINDEX. The CLAS_CALDB_RUNINDEX is an array of information about each subsystem's inefficiency that was derived during the g12 calibration process. The GSIM simulated hits are then “post-processed” by smearing the TDC and ADC hits to imitate the observed resolution of the detector subsystems using the program GPP (GSIM post-processor). GPP also removes detector hits due to inefficient DC wires. The simulation output processed with GPP is then reconstructed with a1c, the same program used to reconstruct data events. The reconstructed simulation is subject to the same scrutiny as real data events, undergoing all the cuts (Sec. 2), corrections [14], and kinematic fitting (Sec. 2.3), as the real data except for beam corrections [14].

7.1 Simulation Verification

Part of understanding the simulation output is understanding how well the simulation mimics the real data. To investigate this, 26,000 real e^+e^- events were treated as generated events and inputted into the

GAM2PART→GSIM→GPP→a1c

chain. Of the 26,000 events, only 100 were successfully reconstructed through the simulation chain. The source of this low efficiency was due to the calibrations entries for the CC and EC in the CLAS_CALDB_RUNINDEX not having values in which would set the “PEDESTAL” values appropriately for simulation. The calibrations constants in the CLAS_CALDB_RUNINDEX were correct for data reconstruction, but not for simulation reconstruction of e^+e^- in the CC and EC subsystems. It was also discovered that the CC and EC subsystems should be simulated with “RUN 10” constants instead of the normal “RUN 56855” used by the g12 group. “RUN 56855” is a special run benchmarked to have the best calibrations and required to properly simulate the ST, DC, and TOF subsystems. To rectify this, a special CLAS_CALDB_RUNINDEX was created, changing “RUN 10” to have “RUN 56855” constants for all subsystems except the CC and EC subsystems which were kept at “RUN 10” constants. Inputting the 26,000 real e^+e^- events into the simulation chain using the CLAS_CALDB_RUNINDEX *RunIndexg12_mk* outputted $\approx 24,700 e^+e^-$ reconstructed events, i.e. $\approx 95\%$ efficiency.

The missing 5 % was a result of “time-based” and “hit-based” tracking

failures. The events that failed “hit-based” tracking contributes a 3.75 % overall event inefficiency. The cause of the “hit-based” failure was never determined, but it was thought to have also occurred in the cooking of the data. Therefore since it did occur in the data reconstruction, this was considered to cancel the inefficiency of the simulation.

The “time-based” failure was due to a random bug in the processing of the TDC element information of ST (STN0) and the ADC element information of ST (STN1) raw data banks. The bug miscalculated the tracks sector exiting the ST even as the hit element of the ST matched that to the track in the DC. If the track failed due to this error, it usually passed “time-based” on the second or third pass of the “time-based” tracking if another particle passed “time-based” during the initial pass. The probability that a track failed initial “time-based” tracking was $\approx .23\%$. The probability that this failed event would pass “time-based” tracking after another pass was $\approx 99.78\%$. The average inefficiency for three charged track events for data was 0.0125%

7.2 PLUTO++ Event Generator

Pluto [20] is a Monte-Carlo event generator designed for the study of hadronic interactions and heavy ion reactions in HADES, FAIR and upcoming PANDA collaborations. The versatility of Pluto enables its use as an event generator for photoproduction in CLAS. For hadronic interactions, Pluto can generate interactions from pion production threshold to intermediate energies of a few GeV per nucleon. The entire software package is based on ROOT and uses ROOT’s embedded C++ interpreter to control the generation of events. Programming event reaction can be set up with a few lines of ROOT macro code without detailed knowledge of programming. Some features in Pluto are, but not limited to;

- Ability to generate events in phase space.
- Ability to generate events with a continuous bremsstrahlung photon beam.
- Ability to generate events weighted by a user defined t -slope.
- Ability to generate events weighted by a user defined cross-section.
 - Total cross section can be inputted via functional form or a histogram.
 - Differential cross sections can be inputted via functional forms or histograms for specific beam energies, with up to 110 histograms relating to intervals of beam energy.
- Ability to generate events that decay via already established physics parameters, i.e. transition form factors.

- Ability to generate events that decay via modified established physics parameters.
- Ability to generate events with multiple production channels, weighted by user inputted cross-section probability.
- Ability to generate events with multiple decay channels, weighted by user inputted branching ratio.
- Ability to perform vertex smearing.
- Ability to create virtual detectors.

For the analysis presented in this work, Pluto was used in conjunction with known differential cross sections to verify simulation momentum smearing and tagger resolution, Sec. 7.4. Pluto was also utilized as a phase space generator in this analysis, to perform a “tune” on the kinematic fitter, Sec. 2.3, to calculate the acceptance corrections Sec. 7.5, and to calculate the normalization Sec. 6.

7.3 Simulating the Lepton Trigger

During the collection process, for an event to be written by the DAQ it must have passed at least one of the trigger “bits” defined in Sec. 2.2.1. As discussed in Sec. 2.2.1, the process of lepton triggering required a coincidence between the EC and the CC subsystems. This coincidence was established by using the voltage sum of the CC for a sector and the voltage sum of the EC for the same sector and comparing each sum to a preset threshold described in Table 4. However when GSIM simulates tracks through the CC and EC, it does not account for the minimum voltage threshold that was required for data collection, moreover the simulation of the trigger must match the trigger efficiency discussed in Sec. 2.6.

Simulation of the CC and EC trigger “bit 6”, Sec. 2.2.1, was performed by writing an algorithm that attempted to mimic the method in which triggered data was recorded. To accomplish this a modified function, written by Simeon McAleer from FSU, was written into the simulation reconstruction algorithm. The routine returned the sector and a boolean of 0 or 1 (pass or fail), that simulated the trigger based on the following criteria;

1. The sector with the highest EC summed energy over threshold.
2. The sector with the highest EC Inner Layer summed energy over threshold.
3. The sector with the highest CC summed energy over threshold.
4. All three above conditions must be in same sector.

Thresholds as described in Table 4 are 80 mV, 60 mV and 20 mV for EC *inner*, EC_{total} and CC respectively. The CC trigger threshold was applied to groups of eight CC PMTs, called “sim bits”. The “sim bits” were staggered by four PMTs so that each PMT goes into two “sim bits”, after which all “sim bits” were “OR”’d together. If any “sim bit” calculated as above threshold, that specific sector was then compared to the remaining sectors to establish the condition listed in 3.

The EC *inner* and EC *total* trigger thresholds were applied to all EC strips in a sector. This was done by summing over the energy for every strip in every orientation of the EC per sector. If the energy summation for the EC *inner* was above threshold, that specific sector was then compared to the remaining sectors to establish the condition listed in 2. If the energy summation for the EC *total* was above threshold, that specific sector was then compared to the remaining sectors to establish the condition of the sector with the highest EC summed energy over threshold.

7.3.1 Validity of Trigger Simulation

The actual triggered data could have been triggered by the following scenarios;

1. e^- CC and EC hit above preset thresholds,
2. e^+ CC and EC hit above preset thresholds,
3. e^- CC hit above preset thresholds and e^+ EC hit above preset thresholds in the same sector,
4. e^- EC hit above preset thresholds and e^+ CC hit above preset thresholds in the same sector.

The lepton trigger “bit 6” was 100% efficient (see Sec. 2.6) when the data was cut using all the conditions listed above (1, 2, 3, 4) using an “OR” flag. This means that a $\gamma p \rightarrow pe^+e^-$ event must satisfy at least one of the listed conditions. The reduction in events when at least one of the conditions was satisfied was 69.91%. Prior to simulating the trigger, cutting the MC with the listed conditions reduced the event yield by 81.91%. Simulating the trigger and cutting on the MC events with the listed conditions reduced that event yield to 69.48%. This indicates that the trigger simulation is properly mimicking the trigger configuration used when data is collected.

7.4 Simulation Kinematic Variables Verification

In the Sec. 7.1 the simulation was verified for efficiency. Another systematic check on the simulation was performed to investigate the validity of the kinematic variables outputted from the simulation package, Sec. 7. This

procedure was also performed as a means to double check the conclusion about the simulation efficiency found in Sec. 7.1 and to verify whether GSIM simulates *pair-production* properly. To perform this check, first the total number of expected π^0 events as well as $\pi^+\pi^-$ events were calculated for the beam energy range 1.1 GeV-2.8 GeV using the total cross-section, σ , for π^0 and $\pi^+\pi^-$ production found in [22] and using

$$N_{events} = \sigma \rho L , \quad (23)$$

where ρ and L are the target density and photon flux respectively. The total number of π^0 and $\pi^+\pi^-$ events can be seen in Fig. 40, where the left axis depicts the number of π^0 events and the right axis depicts the number of $\pi^+\pi^-$ events.

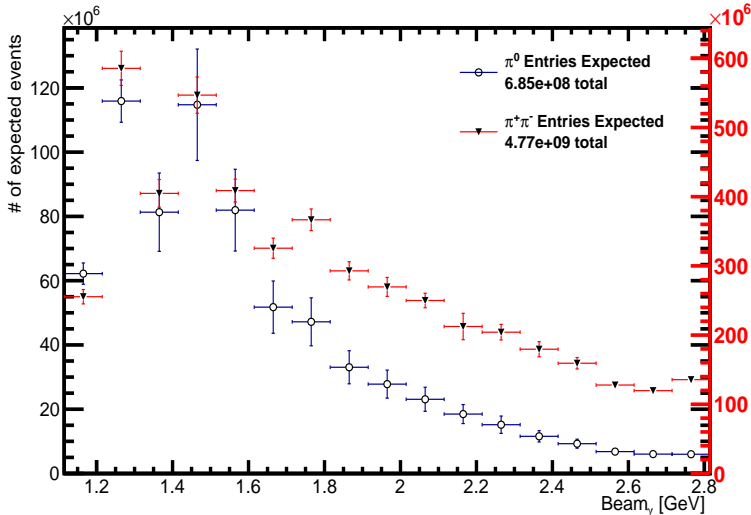
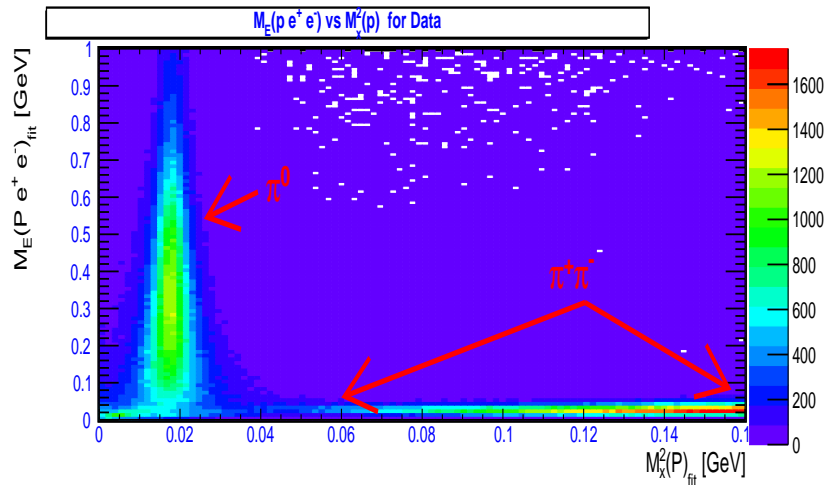


Figure 40: Total Number of π^0 (black open circles) and $\pi^+\pi^-$ (black closed triangles) events expected between E_γ 1.1 GeV-2.8 GeV. The left axis depicts the number of events, per energy bin, expected for π^0 production while the right axis depicts the number of events, per energy bin, expected from $\pi^+\pi^-$ production.

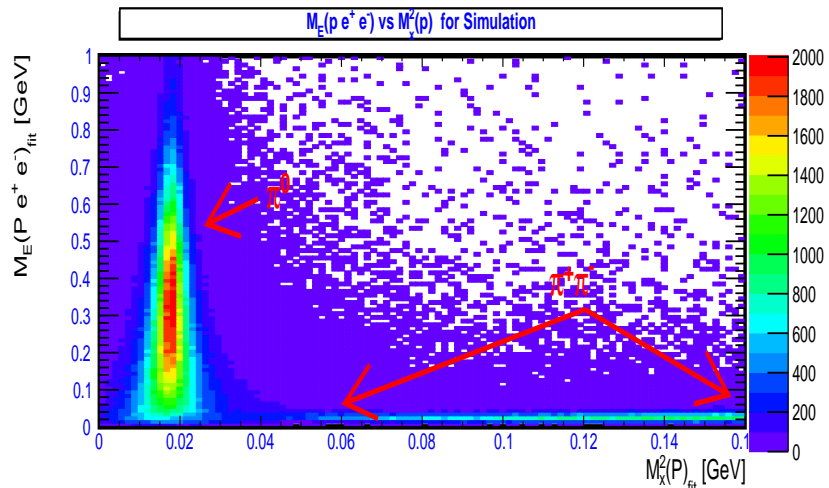
Once the total number of π^0 events was determined, it was necessary to determine the number of $\pi^0 \rightarrow \gamma\gamma$ and $\pi^0 \rightarrow e^+e^-\gamma$ events to generate. This was done via the branching ratios of π^0 decay. The $\pi^0 \rightarrow \gamma\gamma$ has a branching ratio of $(98.823 \pm 0.034)\%$ while $\pi^0 \rightarrow e^+e^-\gamma$ has a branching ratio of $(1.174 \pm 0.035)\%$ [15] which lead to $7.03914 \cdot 10^8 \pi^0 \rightarrow \gamma\gamma$ events generated and $8.36237 \cdot 10^6 \pi^0 \rightarrow e^+e^-\gamma$ events generated. Moreover, once the total number of events were determined, the generation of the events

was weighted using the π^0 differential cross-section found in the SAID [23] database and the $\pi^+\pi^-$ differential cross-section found in the Durham [22] database. After the events were generated, they were processed using the simulation package described in Sec. 7 in which afterward were given the same fiducial cuts described in [14], kinematic constraint cuts Sec. 2.3.3 and trigger simulation cuts Sec. 7.3.

In Figs. 42, 43, 44, 45 it is shown that the simulation procedure appears to give an accurate representation of physics events for the incident beam, detected proton positron and electron within CLAS. Furthermore, the overall acceptance and simulation of *pair-production* is within a normalization factor of 1.011, meaning that the number of generated events was correct within 1.1% or the simulation has an acceptance inefficiency of 1.1%. The different sources contributing to the final detected e^+e^- topology can be seen in Fig. 46.



(a)



(b)

Figure 41: $M_x^2(\gamma p \rightarrow pX)$ vs. $M_E^2(\gamma p \rightarrow pe^+e^-X)$ for systematic check of the simulations. Top panel (a) depicts data, while the bottom panel (b) depicts MC.

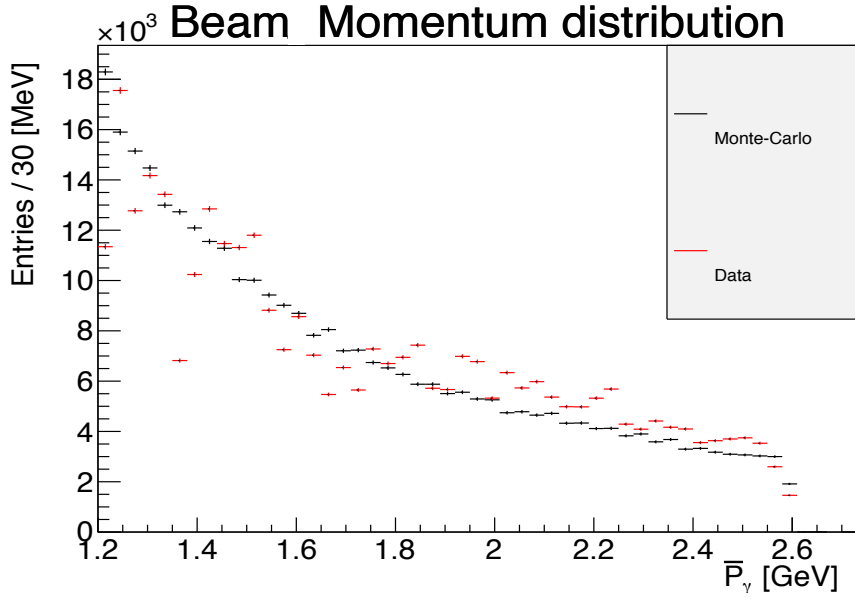


Figure 42: Number of events vs. beam momentum for systematic check of the simulation. Comparison of incident photon beam kinematics for MC (black) events and data (red) when generating MC via differential cross-sections. Normalization factor is 1.011.

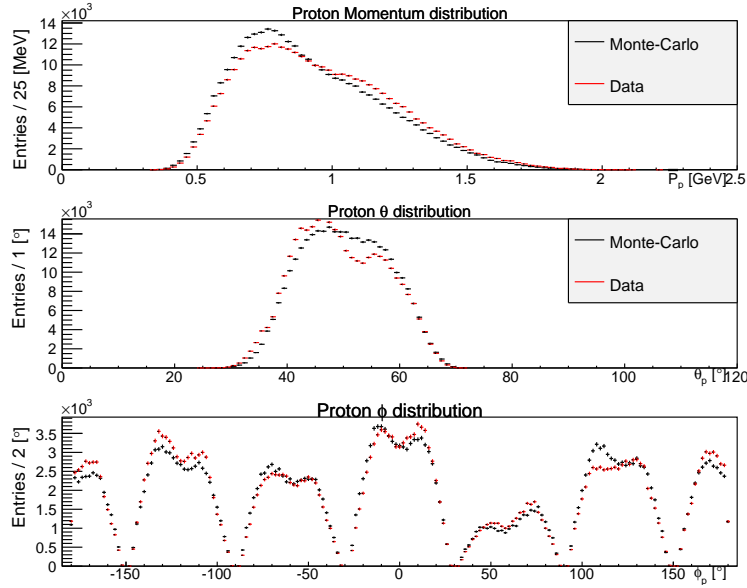


Figure 43: Number of events vs. proton momentum (top), proton θ (middle) and proton ϕ distributions for MC (black) events and data (red) when generating MC via differential cross-sections. Normalization factor is 1.011.

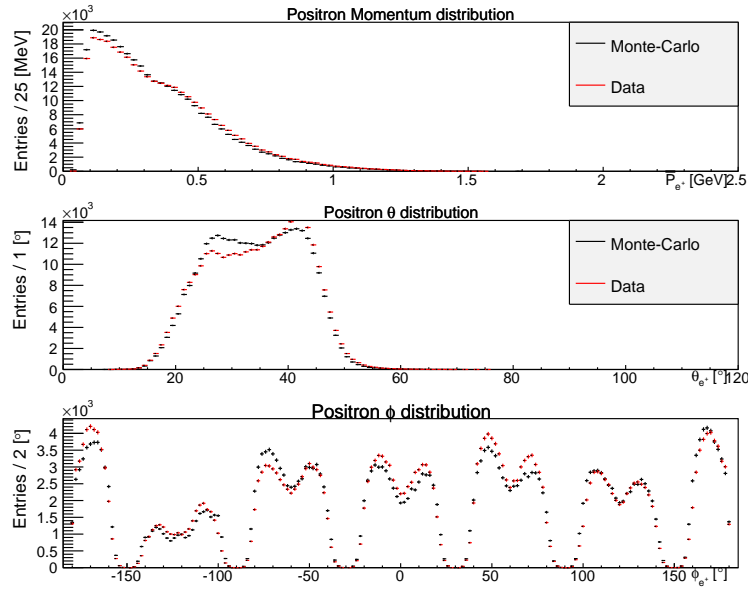


Figure 44: Number of events vs. positron momentum (top), positron θ (middle) and positron ϕ distributions for MC (black) events and data (red) when generating MC via differential cross-sections. Normalization factor is 1.011.

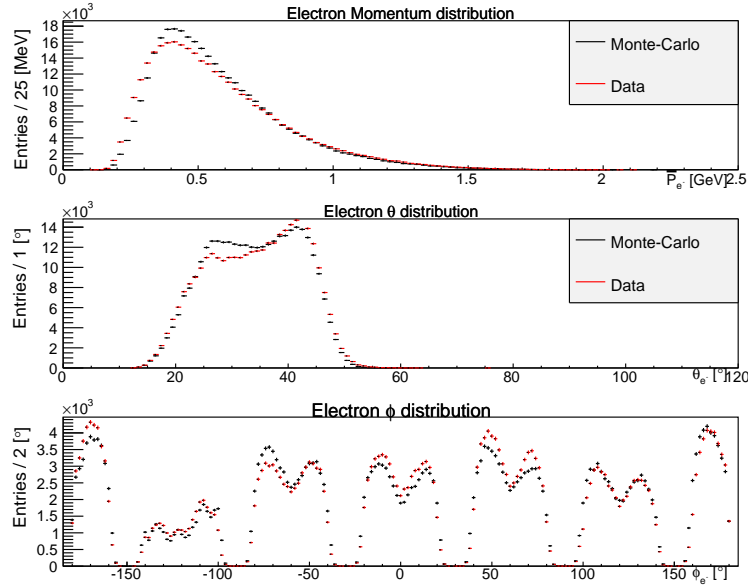


Figure 45: Number of events vs. electron momentum (top), electron θ (middle) and electron ϕ distributions for MC (black) events and data (red) when generating MC via differential cross-sections. Normalization factor is 1.011.

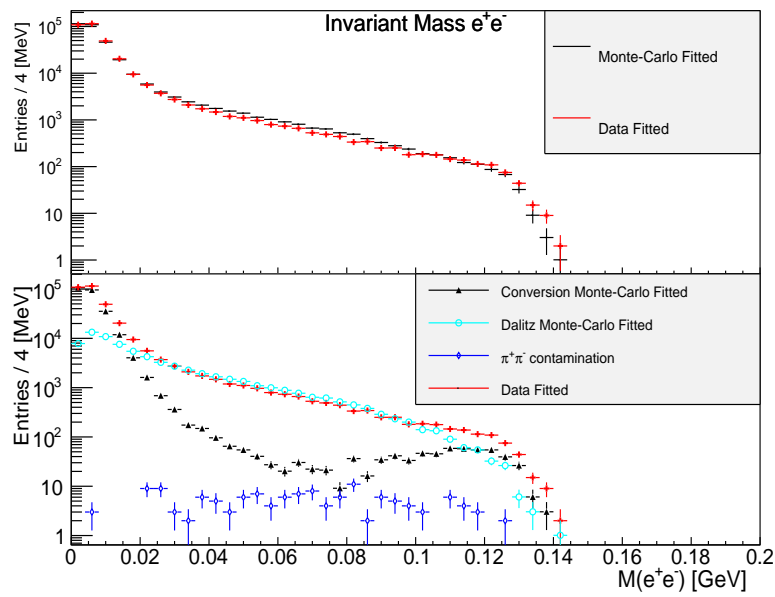


Figure 46: Top Panel: Distributions of the number of events vs. e^+e^- mass for all MC (black) events and data (red). Bottom Panel: Number of events vs. e^+e^- mass distribution showing the sources of the MC e^+e^- topology overlaid to the data. Normalization factor is 1.011.

7.5 Acceptance

The simulation package was verified for both geometry and detector response efficiency in Sec 7. The acceptance for the cross-sections presented in this work was measured using phase-space Monte-Carlo (MC) simulation, using PLUTO++ [20] as the generator, for the reaction channels,



A total of events (N_g), was generated and this number was weighted by the relative branching ratios found in Table 11 to resemble the conditions of the data. The number of events generated for the reaction channel 24a can be found in Table 10 as N_c . The number of events generated for the reaction channel 24b can be found in Table 10 as N_d . After the events are

Quantity	Value·10 ⁷	Description
N_g	240	π^0 events generated
N_c	237	$\pi^0 \rightarrow \gamma\gamma$ events generated
N_d	2.8	$\pi^0 \rightarrow e^+e^-\gamma$ generated

Table 10: Number of generated events in each decay spectrum

generated, they are input into the CLAS simulation chain **GAMP2BOS**, **GSIM**, **GPP**, and then reconstructed with the same program used to reconstruct the data, **a1c**, all programs in the simulation chain use the parameters and the run index described in Sec. 7. For a detailed explanation of this chain, refer to Sec. 7. Once the events are processed through **a1c**, the cuts described in [14], Sec. 7.3, Secs. 2, 2.3.3, are applied as they are to the real data. The acceptance $\eta(E_\gamma, \cos\theta_{C.M.}^{\pi^0})$ is then determined by adding the simulations for the conversion and the dalitz, then for photon energy bins of 25 MeV increments and $\Delta \cos\theta_{C.M.}^{\pi^0} = 0.0125$ increments, the ratio of reconstructed events (N_R) to generated events (N_G) yields,

$$\eta(E_\gamma, \cos\theta_{C.M.}^{\pi^0}) = \frac{N_R(E_\gamma, \cos\theta_{C.M.}^{\pi^0})}{N_G(E_\gamma, \cos\theta_{C.M.}^{\pi^0})}. \quad (25)$$

The $\Delta \cos\theta_{C.M.}^{\pi^0}$ binning in the acceptance is a factor of 2.4 finer than the smallest $\Delta \cos\theta_{C.M.}^{\pi^0}$ increment used in the cross-section measurement. If an

accurate physics model for the generator had been used, as was in Sec. 7, the binning for the acceptance would not have had to be so fine. A list of acceptance plots can be seen in Appendix 10.1

Although not depicted in the plots, the analysis employs a cut of 10% the maximum acceptance value. Meaning is for that bin of incident beam energy, the maximum acceptance was 0.005, then the lowest value to be take was 0.0005.

8 Results

This section will discuss the results of the cross-sections with comparisons to previous world data, as well as a comparison of SAID fits to the previous data sets and this analysis data.

8.1 Cross-Section

In this section, the calculations leading up to the cross-section measurement of the π^0 are described in detail. The number of particles detected in any apparatus in photo-production, Υ , can be described as,

$$\Upsilon(E_\gamma) = \sigma(E_\gamma) \left(\frac{F(E_\gamma) \rho_{target} \ell_{target} N_A}{A_{target}} \right) \eta(E_\gamma) \epsilon \quad (26)$$

where ρ_{target} , ℓ_{target} and A_{target} are the target density, length and atomic weight respectively, N_A is Avogadro's number. The quantities $\sigma(E_\gamma)$, $F(E_\gamma)$, $\eta(E_\gamma)$ are the cross-section for the particle to be produced, the number of photons incident on the target, and the detector acceptance at beam energy E_γ . The factor ϵ is the total efficiency of detecting the particle, sometimes also referred to as normalization. For this analysis ϵ was derived independently of any cross-section, see Sec. 6

If the particle of interest decays into daughters, i.e. $P_{mother} \rightarrow P_{daughter_1} + P_{daughter_2} + \dots + P_{daughter_N}$, then Eq. 26 must be normalized by the branching ratio of the decay $\frac{\Gamma}{\Gamma_{tot}}$. For this analysis, the detected final state particles were proton, electron and positron with a missing photon. The electron, positron and missing photon are the daughter particles of the π^0 decay. However the final state of this decay was a mixture of the π^0 dalitz decay and the π^0 two photon radiative decay with one photon converting into an electron-positron pair. Since the detected final state is a mixture of branching ratios, Eq. 26 must be normalized by the sum of the normalized branching ratios contributing

$$\frac{\Gamma}{\Gamma_{tot}} = \frac{\Gamma_{\pi^0 \rightarrow e^+ e^- \gamma}}{\Gamma_{tot}} + \frac{\Gamma_{\pi^0 \rightarrow \gamma \gamma}}{\Gamma_{tot}}, \quad (27)$$

and the detector acceptance $\eta(E_\gamma)$ also becomes a mixture of the branching ratios.

$$\eta(E_\gamma) = \eta_{\text{dalitz}} + \eta_{\text{conversion}} \quad (28)$$

which is described in Sec. 7.5

The differential cross-section in the center-of-mass system of a particle can be obtained by differentiating eq. 26 with respect to the observables $\cos \theta$ and ϕ , where $\cos \theta$ is the polar angular distribution and ϕ the azimuthal distribution. Since there are no physical observables with respect to ϕ , we can rewrite Eq. 26 as,

$$\frac{d\sigma}{d \cos \theta_{C.M.}^{\pi^0} d\phi} = \frac{1}{2\pi \Delta \cos \theta_{C.M.}^{\pi^0}} \frac{\Upsilon(E_\gamma, \cos \theta_{C.M.}^{\pi^0})}{\eta(E_\gamma, \cos \theta_{C.M.}^{\pi^0}) \epsilon} \left(\frac{A_{\text{target}}}{F(E_\gamma) \rho_{\text{target}} \ell_{\text{target}} N_A} \right) \frac{1}{\Gamma} \quad (29)$$

where $\Delta \cos \theta_{C.M.}^{\pi^0}$ is the width of each $\cos \theta_{C.M.}^{\pi^0}$ bin. In this analysis two bin widths were used

$$\Delta \cos \theta_{C.M.}^{\pi^0} = 0.09375 \quad -1 < \cos \theta_{C.M.}^{\pi^0} < 0 \quad (30a)$$

$$\Delta \cos \theta_{C.M.}^{\pi^0} = 0.03125 \quad 0 < \cos \theta_{C.M.}^{\pi^0} < 1, \quad (30b)$$

in order to minimize statistical errors in the backward direction, Sec. 8.2. The values of the constants used in Eq. 29 can be found in Table 11.

Quantity	Value	Description
A_{target}	1.00794 g/mol	Target atomic number
ρ_{target}	0.0711398 g/cm ³	Target density Sec. 3
ℓ_{target}	40 cm	Length of target [14]
N_A	$6.022 \cdot 10^{23}$	Avogadro's number
$\Gamma_{\pi^0 \rightarrow \gamma\gamma}$	0.98823	Branching ratio of $\pi^0 \rightarrow \gamma\gamma$
$\Gamma_{\pi^0 \rightarrow e^+ e^- \gamma}$	0.01174	Branching ratio of $\pi^0 \rightarrow e^+ e^- \gamma$
$\frac{\Gamma}{\Gamma_{\text{tot}}}$	0.99997	Sum of branching ratios used in this analysis

Table 11: Constants used in $\frac{d\sigma}{d \cos \theta_{C.M.}^{\pi^0} d\phi}$ measurements

8.2 Statistical Uncertainties

In this section, the calculations leading up to the statistical uncertainty of the cross-section measurement will be discussed. Statistical fluctuations of the measurement will depend solely on the variables in Eq. 29 that are not constant and can vary depending on bin width or calculation methods.

For this analysis, discrete binning was employed allowing to utilize Poisson distribution error estimation. A Poisson distribution $P(\lambda, k)$ is defined as,

$$P(\lambda, k) = \frac{\lambda^k e^{-\lambda}}{k!} \quad (31)$$

with k being the observed occurrences, λ being the rate of occurrences and also the variance, is a discrete probability distribution that expresses the probability of a given number of events occurring in a fixed interval of time and/or space if these events occur with a known average rate and independently of the time since the last event [24]. With λ as the variance of the measurement the standard deviation (σ), or error of the measurement is described by $\sigma = \sqrt{\lambda}$. For data samples of uncorrelated variables, the error propagation can be described as

$$\left(\frac{\sigma_f}{f}\right)^2 = \sum_{i=1}^M \left(\frac{\sigma_i}{f_i}\right)^2 \quad (32)$$

Let's denote the differential cross-section as

$$\frac{d\sigma}{d \cos \theta_{C.M.}^{\pi^0} d\phi} = \Xi$$

and the error of Ξ to be

$$\sigma_\Xi = \Xi \left(\left(\frac{\sigma_\Upsilon}{\Upsilon}\right)^2 + \left(\frac{\sigma_{\eta(E_\gamma, \cos \theta_{C.M.}^{\pi^0})}}{\eta(E_\gamma, \cos \theta_{C.M.}^{\pi^0})}\right)^2 + \left(\frac{\sigma_{F(E_\gamma)}}{F(E_\gamma)}\right)^2 \right)^{\frac{1}{2}} \quad (33)$$

where the statistical error of the flux $F(E_\gamma)$ and detected particles Υ is given by Poisson statistics,

$$\sigma_{F(E_\gamma)} = \sqrt{F(E_\gamma)} \quad (34a)$$

$$\sigma_\Upsilon = \sqrt{\Upsilon}. \quad (34b)$$

From Eq. 25

$$\left(\frac{\sigma_\eta}{\eta}\right) = \left(\left(\frac{\sigma_R}{N_R}\right)^2 + \left(\frac{\sigma_G}{N_G}\right)^2 \right)^{\frac{1}{2}} \quad (35)$$

where the statistical error of the reconstructed events, σ_R , and generated events, σ_G , is given by Poisson statistics

$$\begin{aligned} \sigma_R &= \sqrt{N_R} \\ \sigma_G &= \sqrt{N_G} \end{aligned}$$

therefore

$$\left(\frac{\sigma_\eta}{\eta}\right) = \left(\frac{1}{N_R} + \frac{1}{N_G}\right)^{\frac{1}{2}} \quad (37)$$

The number of events reconstructed, N_R for the simulation was chosen to be such that $N_R \sim 4\Upsilon$, while the pair-production rate combined with the acceptance made it such that $N_R \ll N_G$, simplifying Eq. 37 to be

$$\left(\frac{\sigma_\eta}{\eta}\right) = \left(\frac{1}{4\Upsilon}\right)^{\frac{1}{2}}. \quad (38)$$

It should also be noted that the beam energy binning chosen reflects that $\Upsilon \ll F(E_\gamma)$ and so substituting Eqs. 34b, 34a, 38 into Eq. 33 yields

$$\sigma_\Xi = \Xi \left(\frac{1}{\Upsilon} + \frac{1}{4\Upsilon}\right)^{\frac{1}{2}} \quad (39)$$

The backward angle binning discussed in Sec 8.1 Eq. 30a was chosen to minimize the statistical error by maximizing

$$\left(\frac{1}{\Upsilon} + \frac{1}{4\Upsilon}\right)^{\frac{1}{2}} \quad (40)$$

The contribution of Eq. 40 is shown in Fig. 47 for values of $\Upsilon < 100$ which is typical at high beam energies, large backward $\cos\theta_{C.M.}^{\pi^0}$.

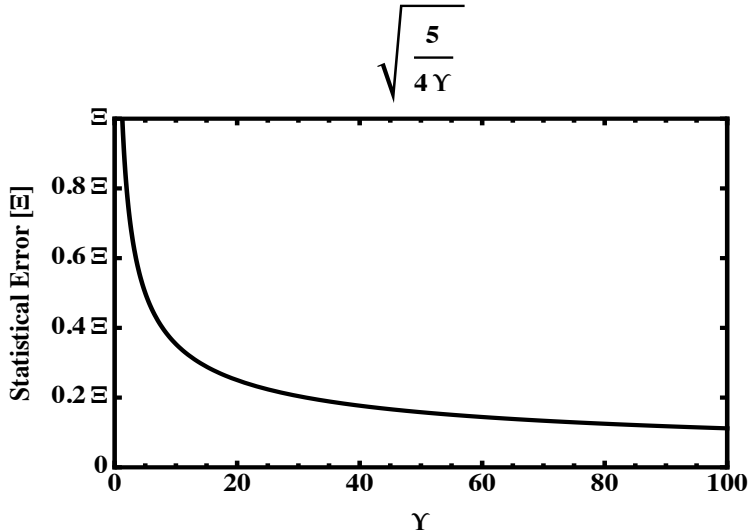


Figure 47: The uncertainty plotted vs. the total number of detected events and reconstructed events from MC, for small values of Υ . The binning in the backward direction was chosen to maximize Υ to reduce the overall statistical error

8.3 Systematic Uncertainty

In this section, the calculations leading up to the systematic of the measurement will be discussed. Systematic errors are caused by the controls of the experiment, such as flux, simulation, density and length of the ℓH_2 target and also systematic errors are caused by various analytical tools used, such as the kinematic fitter.

8.3.1 Branching Ratio Systematic Uncertainty

The branching ratios for the two topologies used to measure the cross-section were obtained from PDG [15] and are listed in Table 12 with their associated errors. Uncorrelated quantities that are summed as,

$$f = \sum_{i=1}^M a_i P_i \quad (41)$$

have errors as

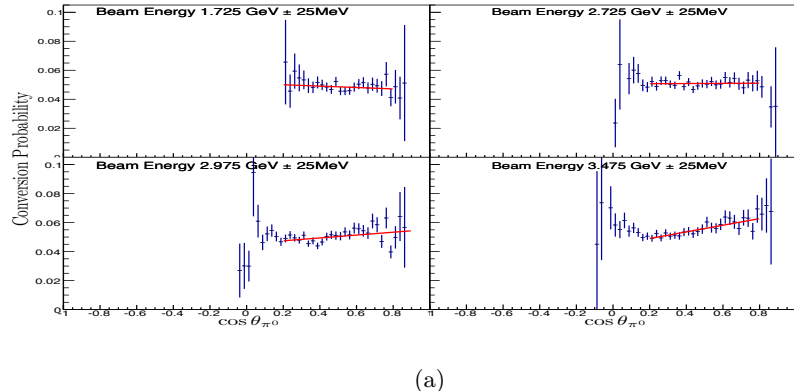
$$\sigma_f = \sqrt{\sum_{i=1}^M (a_i \sigma_i)^2}. \quad (42)$$

Therefore

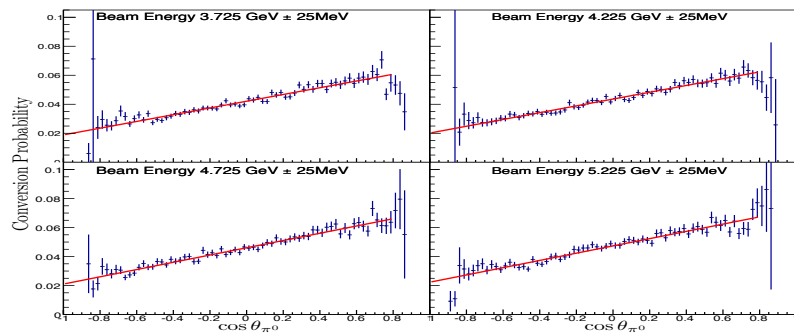
$$\frac{\Gamma}{\Gamma_{tot}} = \frac{\Gamma_{\pi^0 \rightarrow e^+ e^- \gamma}}{\Gamma_{tot}} + \frac{\Gamma_{\pi^0 \rightarrow \gamma\gamma \rightarrow e^+ e^- \gamma}}{\Gamma_{tot}} \quad (43)$$

$$= \frac{\Gamma_{\pi^0 \rightarrow e^+ e^- \gamma}}{\Gamma_{tot}} + \frac{\Gamma_{\pi^0 \rightarrow \gamma\gamma} P(\gamma \rightarrow e^+ e^-)}{\Gamma_{tot}}, \quad (44)$$

where $P(\gamma \rightarrow e^+ e^-)$ is the probability of photon conversion into $e^+ e^-$. To measure $P(\gamma \rightarrow e^+ e^-)$, the acceptance for conversion ($P(\gamma \rightarrow e^+ e^-) \cdot \eta_{e^+ e^-}$) is divided by the acceptance for Dalitz ($\eta_{e^+ e^-}$). Fig. 48 shows that the conversion probability depends on incident photon energy. A maximum probability of 8% per-photon was measured, shown in Fig 48b bottom right plot. Therefore



(a)



(b)

Figure 48: Probability of Photon Conversion vs. $\cos \theta$ for various values of E_γ . The maximum probability for this analysis was measured in the bottom right plot of (b).

$$\frac{\Gamma}{\Gamma_{tot}} = \frac{\Gamma_{\pi^0 \rightarrow e^+ e^- \gamma}}{\Gamma_{tot}} + \frac{\Gamma_{\pi^0 \rightarrow \gamma\gamma} P(\gamma \rightarrow e^+ e^-)}{\Gamma_{tot}} = 0.09 , \quad (45)$$

and has error

$$\sigma_f = \sqrt{\left(\frac{1}{\Gamma_{tot}}\right)^2 (\sigma_{\pi^0 \rightarrow e^+ e^- \gamma}^2 + \sigma_{\pi^0 \rightarrow \gamma\gamma}^2)} = 0.0037. \quad (46)$$

The energy and $\cos\theta$ dependence of the conversion is accounted for in the acceptance, which is E_γ and $\cos\theta$ bin-dependent.

Quantity	Value	Error
$\Gamma_{\pi^0 \rightarrow \gamma\gamma}$	0.98823	0.00034
$\Gamma_{\pi^0 \rightarrow e^+ e^- \gamma}$	0.01174	0.00035
$\frac{\Gamma}{\Gamma_{tot}}$	0.13	0.0037

Table 12: Branching ratio and errors used in the $\frac{d\sigma}{d\cos\theta_{C.M.}^{\pi^0} d\phi}$ measurements.

8.3.2 Cut Based Systematic Uncertainty

The procedure to determine the systematic uncertainty of the cuts placed on the various kinematic fits was first to calculate an acceptance with a different cut, then to calculate a new total cross-section measurement applying the different cut to the data. The total cross-section was computed at various photon beam energies. Lets denote the original measured total cross-section as Ξ_1 and the new total cross-section determined by the new cut as Ξ_n , then the systematic error was calculated as.

$$\sigma_{cut} = \frac{|\Xi_1 - \Xi_n|}{\Xi_1} \quad (47)$$

Some systematic uncertainty depended on the photon energy. All cut based systematics were performed individually, meaning when a cut was changed, the remaining cuts retained their original value, see Table 13 for the values of the cuts that were changed to calculate the systematic error. The decision to use 10% as the adjusted cut was that the CL distribution from 1% to 20% had the same shape as 1% to 10%, therefore author wanted to use the maximum amount of statistics because of fine binning used.

Cut	Original	Adjusted	Uncertainty
2-C Fit	1%	10%	0.0219
1-C Fit	1%	10%	$0.00216 + 0.01083E_\gamma$
4-C Fit	1%	10%	0.00031
Missing Energy	75 MeV	100 MeV	0.02781

Table 13: Different Cuts to analyze systematics

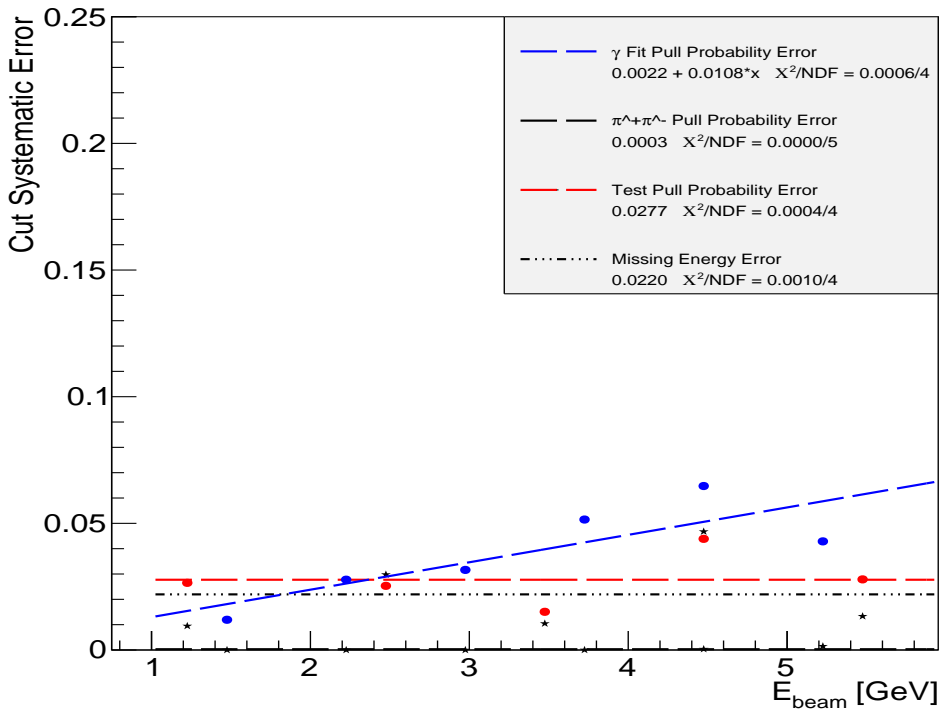


Figure 49: Plot showing the contribution of the systematic error and the incoming beam dependence of the error for the various cuts used in the data (see plot legend).

8.3.3 Photon Flux Systematic Uncertainty

The photon flux calculation should be consistent throughout the experiment. If the flux measurement is not consistent due to corrections made with the live-time, beam corrections or fractional difference in the reported current to the actual current during the photon flux normalization run then a systematic uncertainty would be produced. The systematic uncertainty of the

photon flux was derived in [14] and is quoted to be as a lower limit of 5.7%.

8.3.4 Detector Efficiency Systematic Uncertainty

Each sector in CLAS can be treated as an individual detector, with its own efficiency and resolution. A systematic uncertainty could arise if one or more of the sectors is not simulated properly. The procedure to determine the systematic error, σ , of the sector is to calculate the accepted corrected yield, Υ^c , for each sector and compare Υ^c to the average accepted corrected yield of all 6 sectors, μ^c . After σ is calculated, it was normalized to $N\mu^c$ as to represent the error as a percentage, which later is multiplied by the measured cross section to determine the appropriate error.

$$\sigma_{sector} = \sqrt{\sum_{i=1}^{N=6} (\Upsilon_i^c - \mu^c)}, \quad (48)$$

where

$$\mu^c = \frac{1}{N} \sum_{i=1}^{N=6} \Upsilon_i^c \quad (49)$$

$$\sigma_{sector}^{normalized} = \frac{\sigma_{sector}}{N\mu^c} \quad (50)$$

This calculation was performed using $\gamma p \rightarrow p\pi^0$ yields for various bins of incoming beam energy to determine the beam energy dependence (see Fig. 50).

The sector systematic uncertainty is consistent with the extracted sector systematic uncertainty from the g11 data set [25](seeFig. 51).

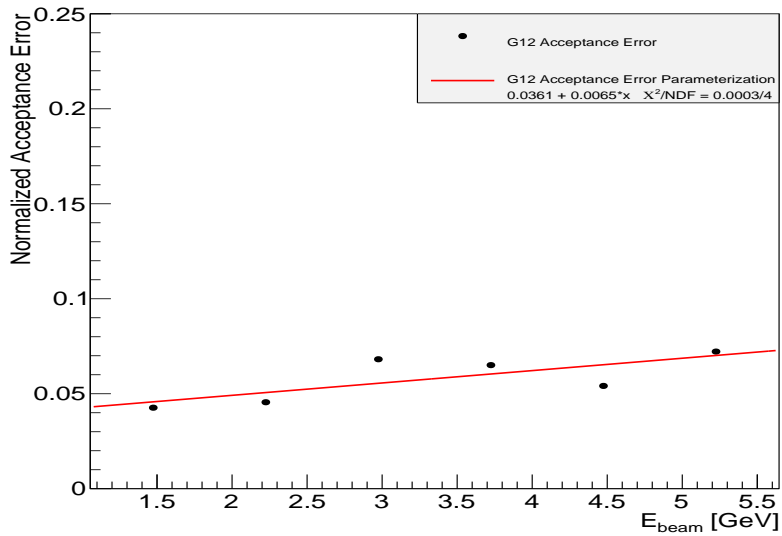


Figure 50: The sector systematic uncertainty as a function of the incoming photon energy.

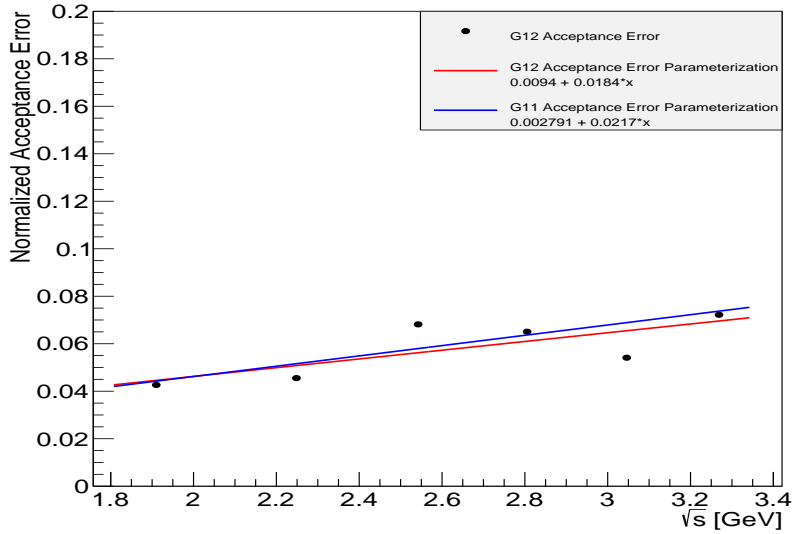


Figure 51: Comparison of sector systematic uncertainty to the g11 measurement.

8.3.5 z -vertex Cut Systematic Uncertainty

The systematic uncertainty of the z -vertex cut was analyzed by varying the initial vertex cut from $-110 \leq z \leq -70$ to $-109 \leq z \leq -71$ for both data and MC. The choice of ± 1 cm was chosen based upon hte vertex resolution in CLAS. Afterward the procedure for determining the systematic was identical to the method used to determine the "Cut Based Systematic Uncertainty". The systematic uncertainty from varying the z was 0.0041, shown in Fig. 61

8.3.6 Target Systematic Uncertainty

Since the systematic uncertainty on the density is 0.02%, see [14], the maximum systematic on the target is due to uncertainty in the length on the target which is $40 \text{ cm} \pm 0.2 \text{ cm}$. A total systematic on the target was assign to be 0.5%.

8.3.7 Track Efficiency Systematic Uncertainty

To calculate the track-efficiency systematic uncertainty, the calculation was redone as described in Sec. 6.2 of the analysis note. The track-efficiency for the systematic study had a binning scheme of θ, ϕ , Fig. 52, instead of the $\theta \sin \phi, \theta \cos \phi$ binning seen in Fig. 31 in the analysis note.

Three-charged track-efficiency values from the initial procedure, described in Sec. 6.2, were compared to the values from this new binning. Since both techniques are not known quantities, the method for calculating the error between the is;

$$\Delta = \frac{x_{\text{previous}} - x_{\text{new}}}{\frac{x_{\text{previous}} + x_{\text{new}}}{2}} \quad (51)$$

where x_{previous} is a value of a three-charged track-efficiency from the mapping of Sec 6.2 and x_{new} is a three-charged track-efficiency from the mapping from the new set of figures derived for this systematic calculation.

Since both values are corrections, it makes little statistical sense to promote one to a "known value", therefore the only appropriate method to measure the error between the values is to use the percent difference method. In this method the denominator is the average value between the two hypotheses, hence the factor of 2.

Angular dependence

To investigate whether there exists a C.M. $\cos \theta$ dependence, the values of Eq. 51 were binned in according with the event C.M. $\cos \theta$, per E_γ value.

From Figs.[53, 54, 55, 56], there appears that any dependence on $\cos \theta$ is negligible because the relative uncertainty for each $\cos \theta$ value at a certain beam energy is mostly within errors of the neighboring $\cos \theta$ values and the

Proton Over_Efficiency at $-90 < z < -85$ cm at $0.75 < P < 1$ GeV

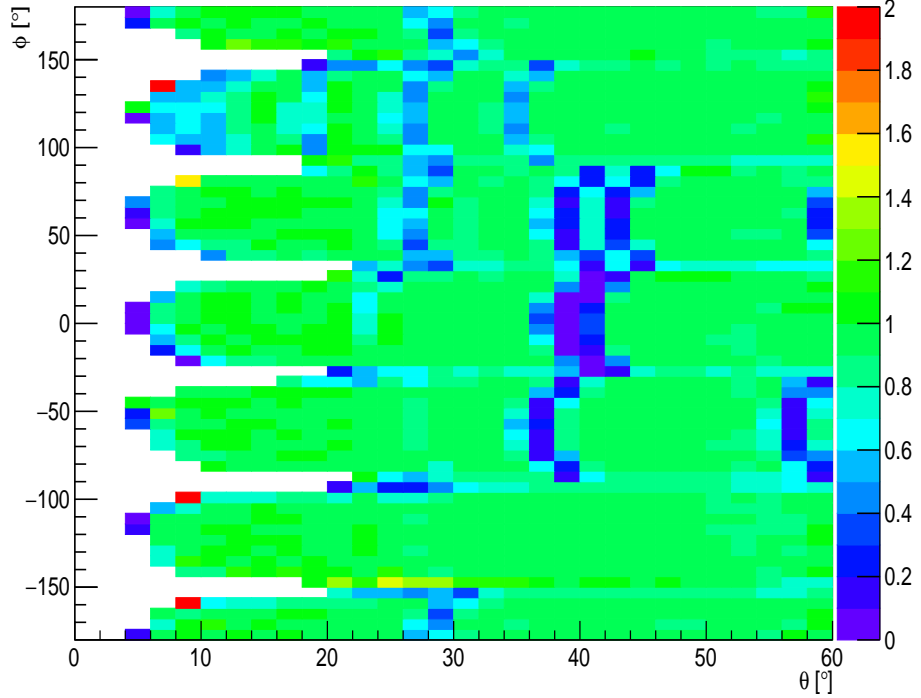
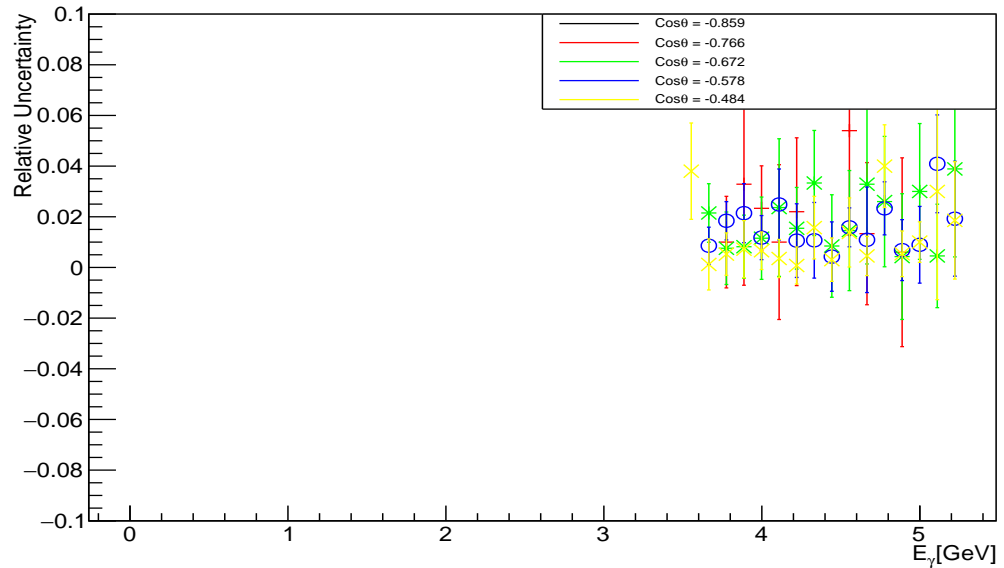
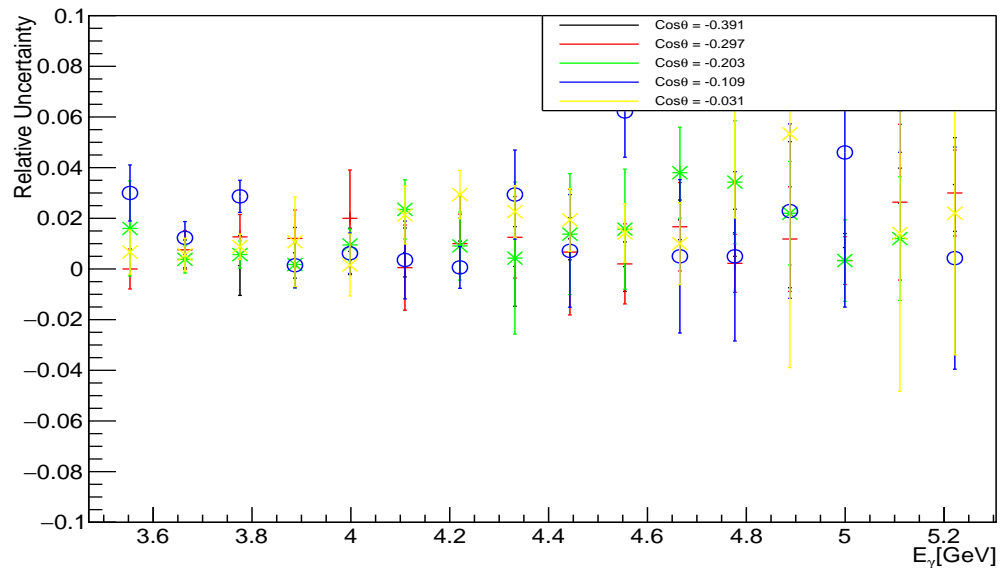


Figure 52: ϕ vs. θ plot showing the over-efficiency of simulating the proton with z-vertex $-90 < z < -85$ cm and momentum $0.75 < p < 1$ GeV from a 2 charged track reaction.

relative shape of the distribution for neighboring $\cos \theta$ values are mostly alike. The only exception for this the 2 bins for $\cos \theta = 0.703$ and $\cos \theta = 0.734$ (Fig. 56), however these 2 bins account for 2/37 of all $\cos \theta$ bins.

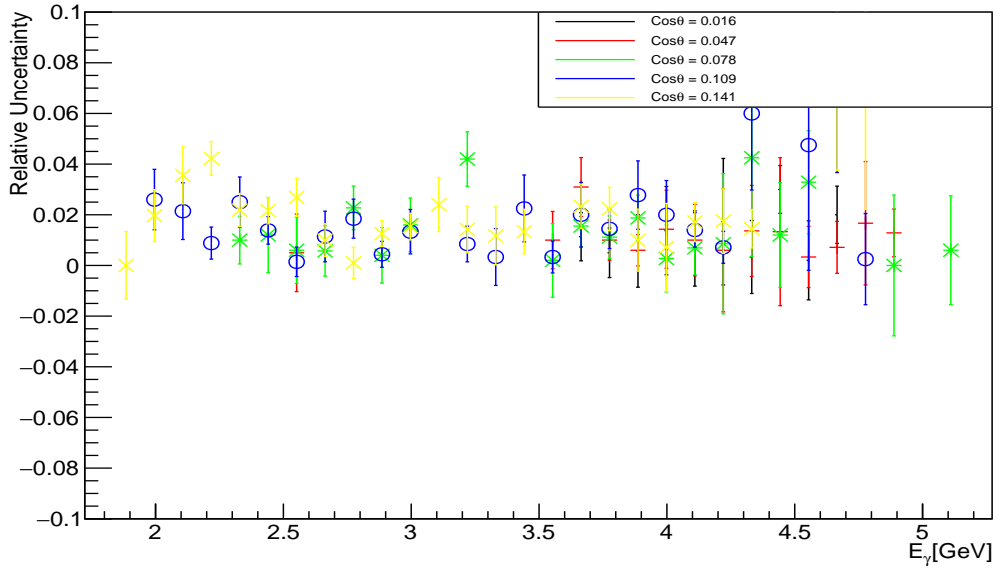


(a) $-0.859 < \cos \theta < -0.484$

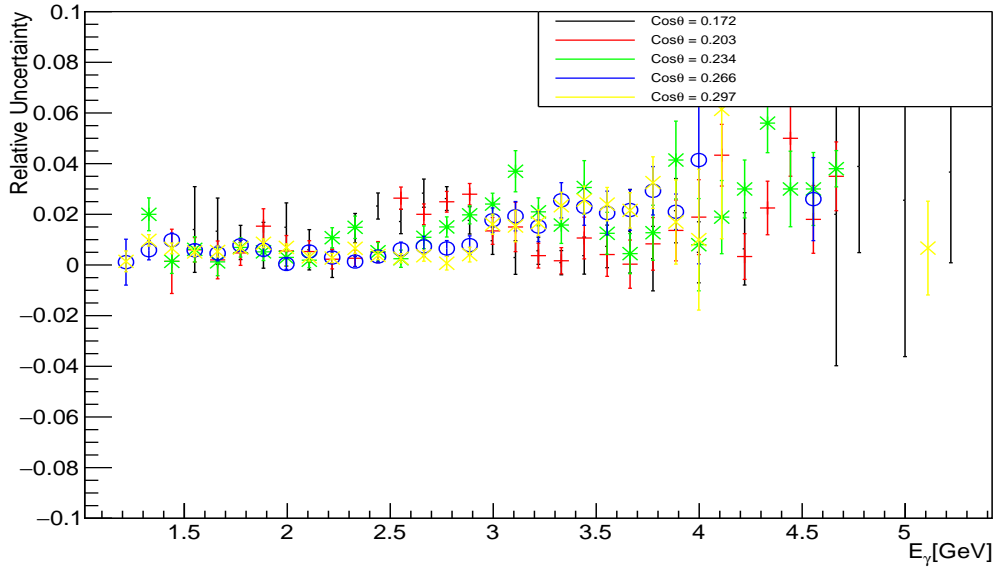


(b) $-0.391 < \cos \theta < -0.031$

Figure 53: (Color Online) Mean relative uncertainty vs. E_γ calculated between the two sets of track efficiencies for $\cos \theta$.

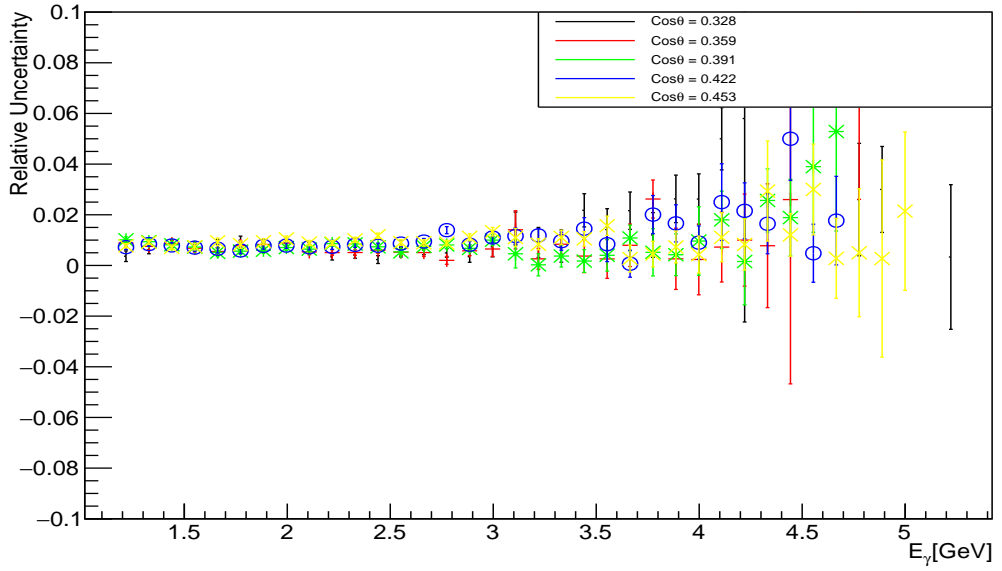


(a) $0.016 < \cos \theta < 0.141$

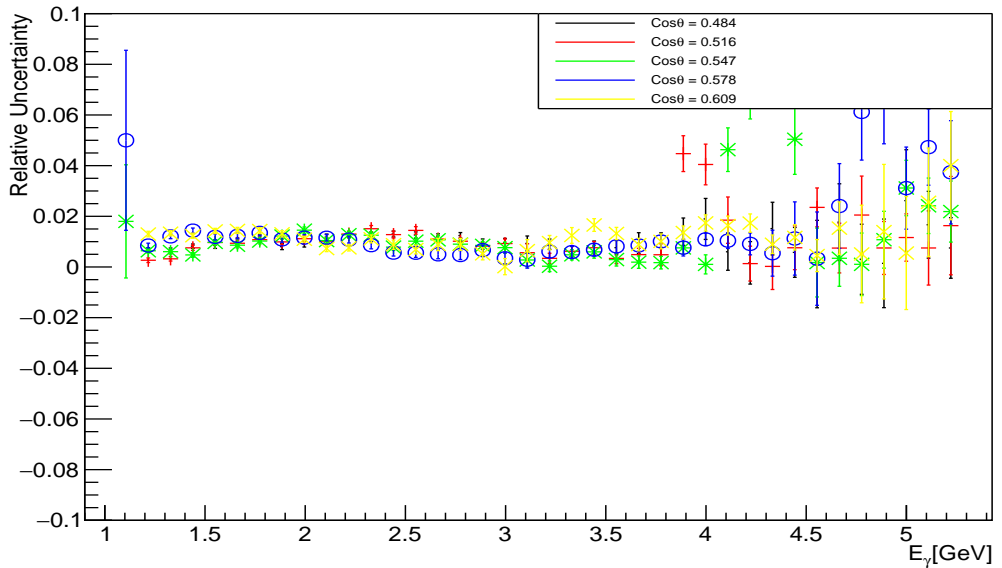


(b) $0.172 < \cos \theta < 0.297$

Figure 54: (Color Online) Mean relative uncertainty vs. E_γ calculated between the two sets of track efficiencies for $\cos \theta$.

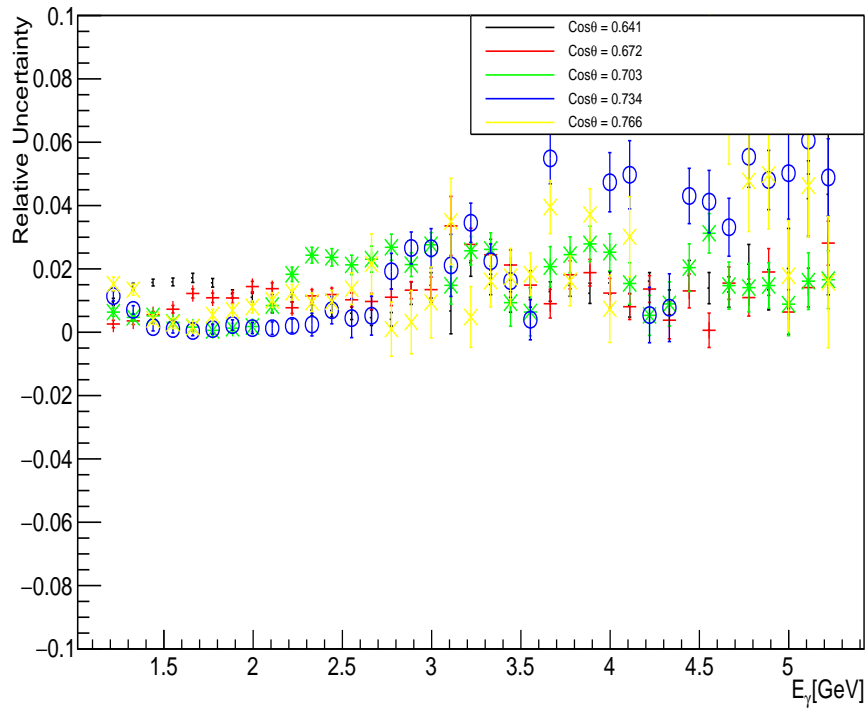


(a) $0.328 < \cos\theta < 0.453$

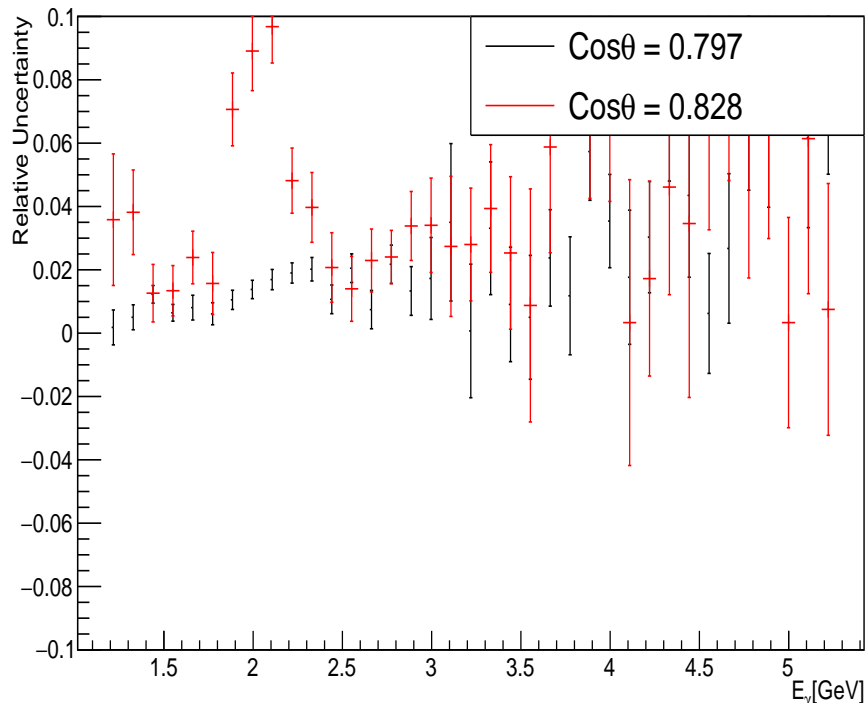


(b) $0.484 < \cos\theta < 0.609$

Figure 55: (Color Online) Mean relative uncertainty vs. E_γ calculated between the two sets of track efficiencies for $\cos\theta$.



(a) $0.641 < \cos \theta < 0.766$



(b) $0.797 < \cos \theta < 0.828$

Figure 56: (Color Online) Mean relative uncertainty vs. E_γ calculated between the two sets of track efficiencies for $\cos \theta$.

Incident photon (E_γ) dependence

To investigate whether there exists a C.M. $\cos \theta$ dependence, the values of Eq. 51 were binned in according with the event C.M. $\cos \theta$. To investigate whether there exists a dependence to the variable of incident beam energy (E_γ), the values of Eq. 51 were binned in according with the event E_γ . Two regions were chosen, the “Lep Trigger” region, which consists of incident beam energies between 1.1 –3.6 GeV and the “MOR” region, which consists of incident beam energies between 3.6 –5.5 GeV. Figure 57 and Fig. 58 depict the mean value of Eq. 51 for bins of C.M. $\cos \theta$ and incident beam energy for the “Lep Trigger” and “MOR trigger” regions respectively.

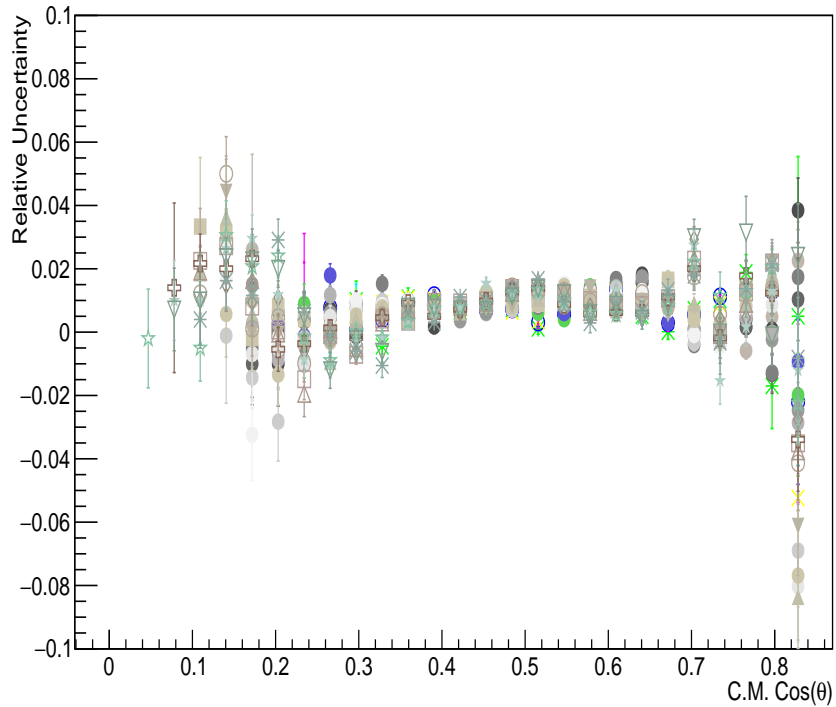


Figure 57: Mean relative uncertainty vs. $\cos \theta$ calculated between the two sets of track efficiencies for incident beam energy between 1.2–3.6 GeV. Multiple points in $\cos \theta$ are bins of incident beam energy.

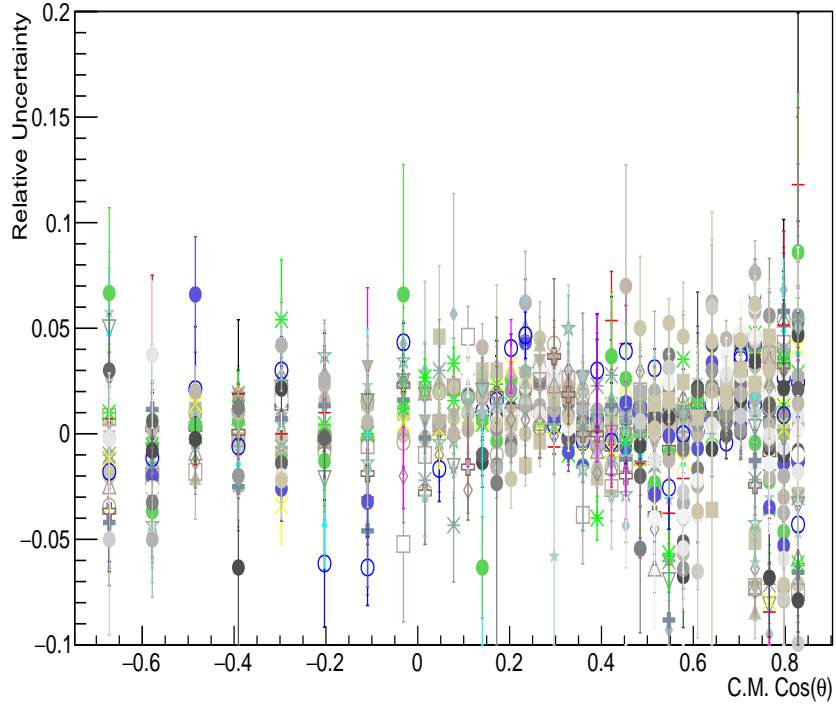


Figure 58: Mean relative uncertainty vs. $\cos \theta$ calculated between the two sets of track efficiencies for incident beam energy between 3.6–5.5 GeV. Multiple points in $\cos \theta$ are bins of incident beam energy.

Therefore, to investigate the dependence on incident beam energy the mean value for all C.M. $\cos \theta$ bins per incident beam energy were plotted, example plots for this can be seen in Fig. 59. The mean and RMS track-efficiency systematic uncertainty value from each incident beam energy was added in quadrature and plotted as a function of incident beam energy. This distribution was then fit to a 2nd order polynomial and the values of the polynomial were taken to be the systematic uncertainty for the track-efficiency, which is dependent on incident beam energy. This fit and distribution can be seen in Fig. 60.

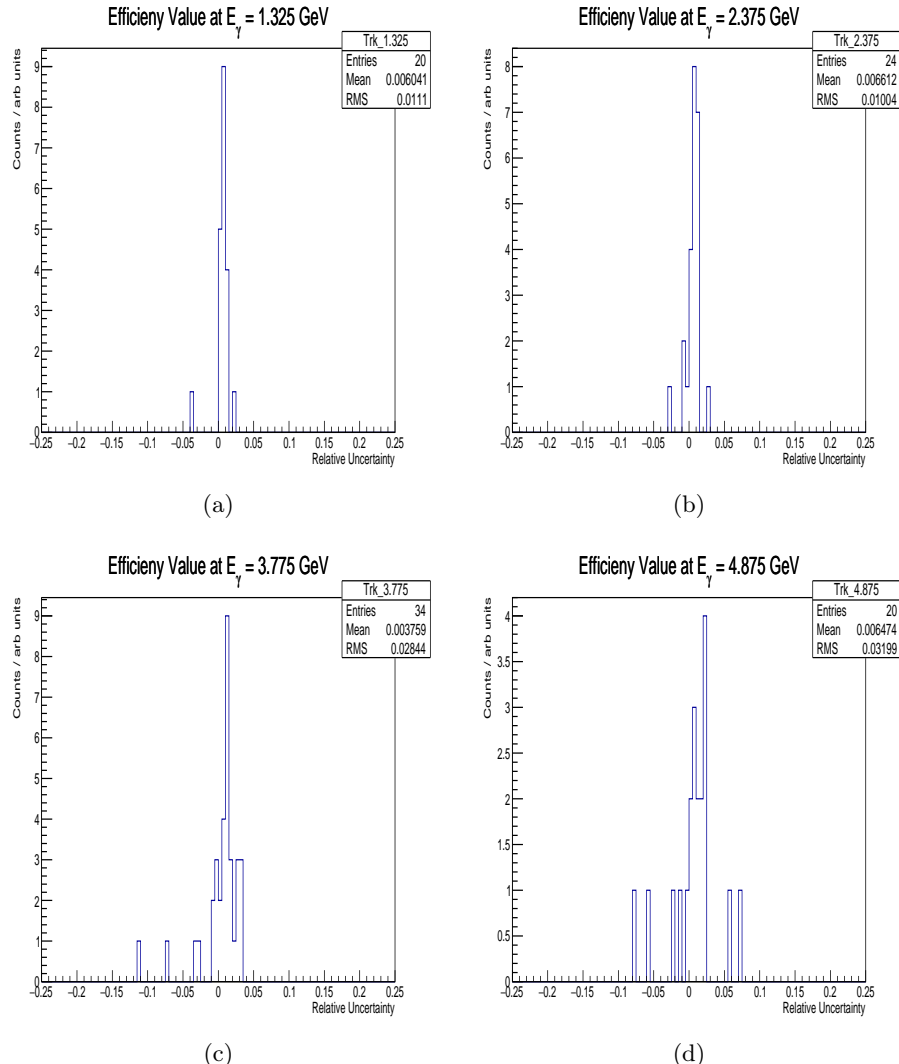


Figure 59: Mean value per incident beam energy 1.325 GeV(a), 2.375 GeV(b), 3.775 GeV(c), 4.875 GeV(d).

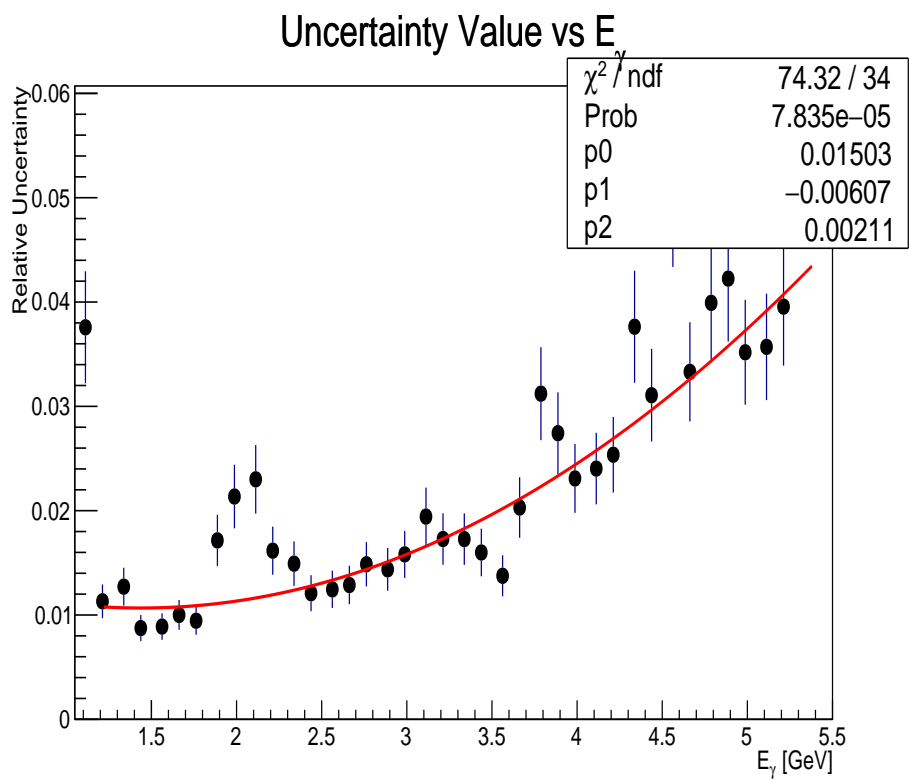


Figure 60: (Color-online) Relative error calculated between the two sets of track efficiencies as a function of incident beam energy (black points). Fit consisting of a 2nd order polynomial to the data (red line).

8.3.8 Total Systematic Uncertainty

The total systematic uncertainty along with a list of the individual sources of systematic error is presented in this subsection. The calculation of the total systematic error is

$$\sigma_{tot}^{sys} = \sqrt{\sum_{i=1}^M \sigma_i^2}. \quad (52)$$

This total uncertainty is an upper limit, as some of the sources of the uncertainty were derived from a bin-by-bin analysis, but their upper limits are quoted. A bin-by-bin analysis for all systematic uncertainties was not possible with the binning scheme used for the specific uncertainty. For example, the sector systematic was energy dependent, adding a third, very fine binned, dimension would not have been possible with the statistics in each sector. The E_γ dependence on the systematics is due to the Lorentz boosting as energy increases, see Appendix 10.2. Figure 61 is a pictorial version of Table 14.

Relative Systematic	Error (\leq)
Particle Efficiency (total)	$0.01503 - 0.00607E_\gamma + 0.0021E_\gamma^2$
Sector	$0.0361 + 0.0065E_\gamma$
Flux	0.057
Missing Energy Cut	0.02781
2-C Fit Pull Probability	0.0219
1-C Fit Pull Probability	$0.00216 + 0.01083E_\gamma$
4-C Fit Pull Probability	0.00031
Target	0.005
Branching Ratio	0.0037
Fiducial Cut	0.024
z -vertex Cut	0.0041
Total	$\sqrt{(6.67 + 0.334E_\gamma + 0.26E_\gamma^2) \cdot 10^{-3}}$

Table 14: Upper limit of relative systematic uncertainty used in the $\frac{d\sigma}{d \cos \theta_{C.M.}^{\pi^0} d\phi}$ measurements.

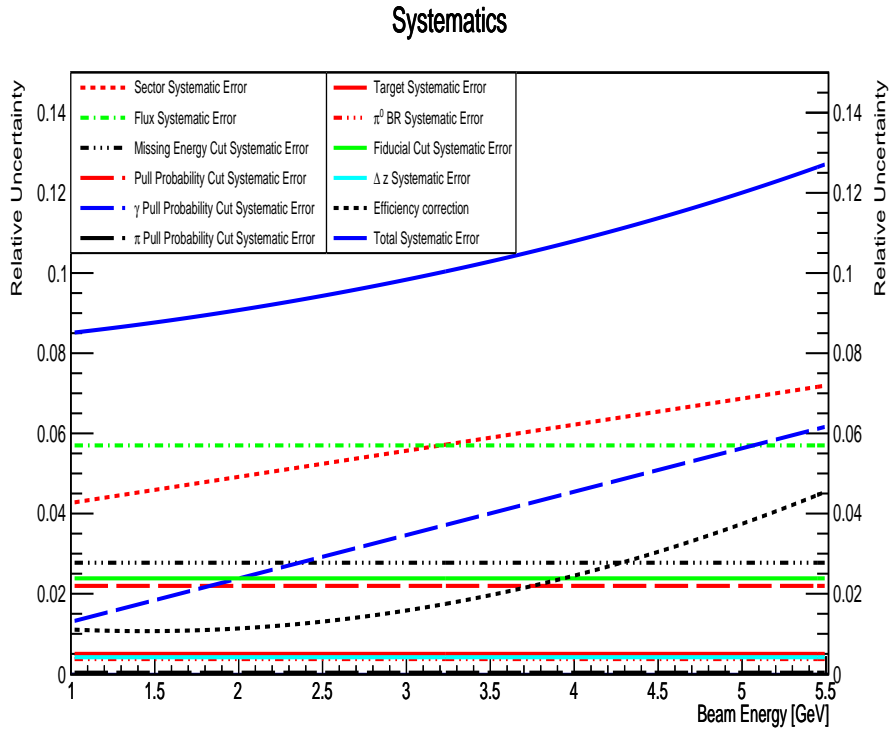


Figure 61: The contribution of all systematic uncertainties.

8.4 Comparison to World Data and SAID Fits

This section will discuss comparisons of our data with SAID fits and the GPD handbag model. The SAID parameterization, discussed in [23], for this analysis was based upon previous data observables in conjunction with the new cross-section measurement presented in this analysis.

8.4.1 Differential Cross-Sections $\frac{d\sigma}{d\Omega}$

The differential cross-sections $\frac{d\sigma}{d\Omega}$ are illustrated in Figs. 62, 63, 64, 65. A brief discussion is presented in Sec. 8.4.5.

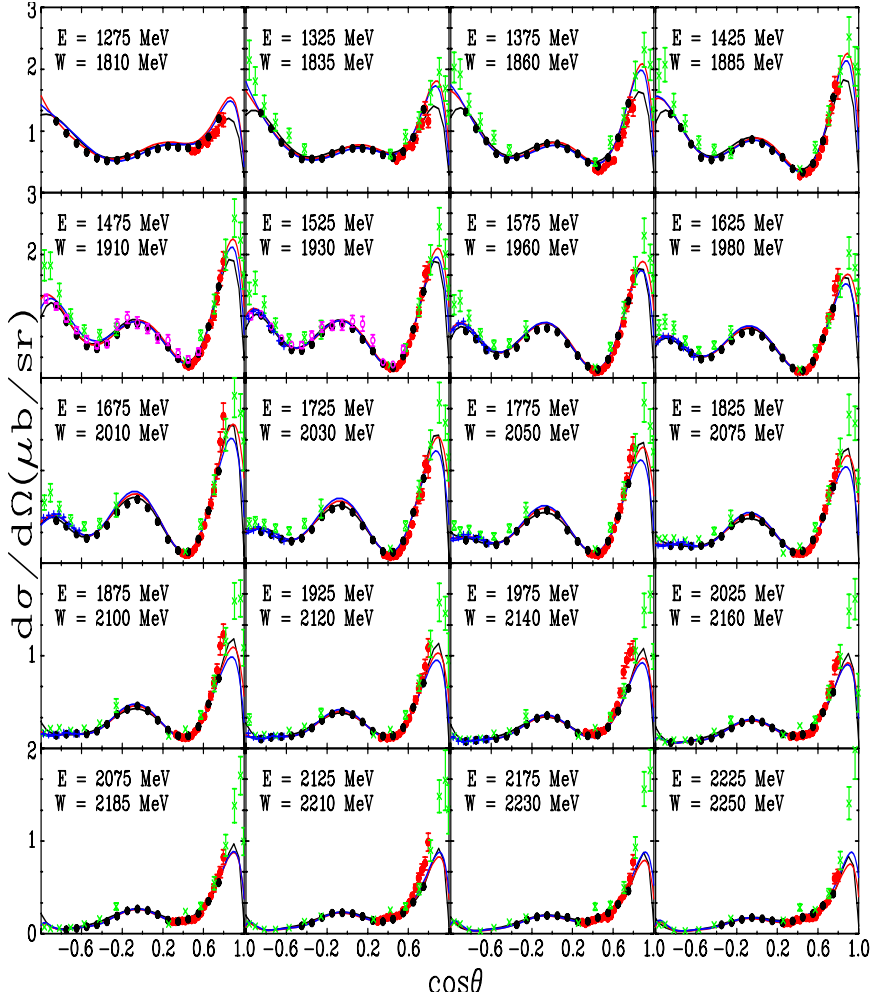


Figure 62: (Color online) The π^0 proton photoproduction cross section, ($d\sigma/d\Omega$), at $E_\gamma = 1.275 - 2.225$ GeV versus $\cos\theta$ where θ is the pion center-of-mass production angle. Photon energy is indicated by E , while the center-of-mass total energy is indicated by W . Red solid (blue solid) lines show the SAID KU14 (DU13 [26]) calculations. Black solid lines give the BG2011-02 BnGa [27] predictions. Experimental data are from the current measurement (red filled circles), CLAS [28] (black filled circles), GRAAL [29] (magenta open circles), LEPS [30] (blue plus), CB-ELSA [31] [21] (green crosses) and previous bremsstrahlung measurements [32] (black open circles). Plotted uncertainties are statistical. The plotted points from previously published experimental data are those data points within ± 3 MeV of the photon energy indicated on each panel.

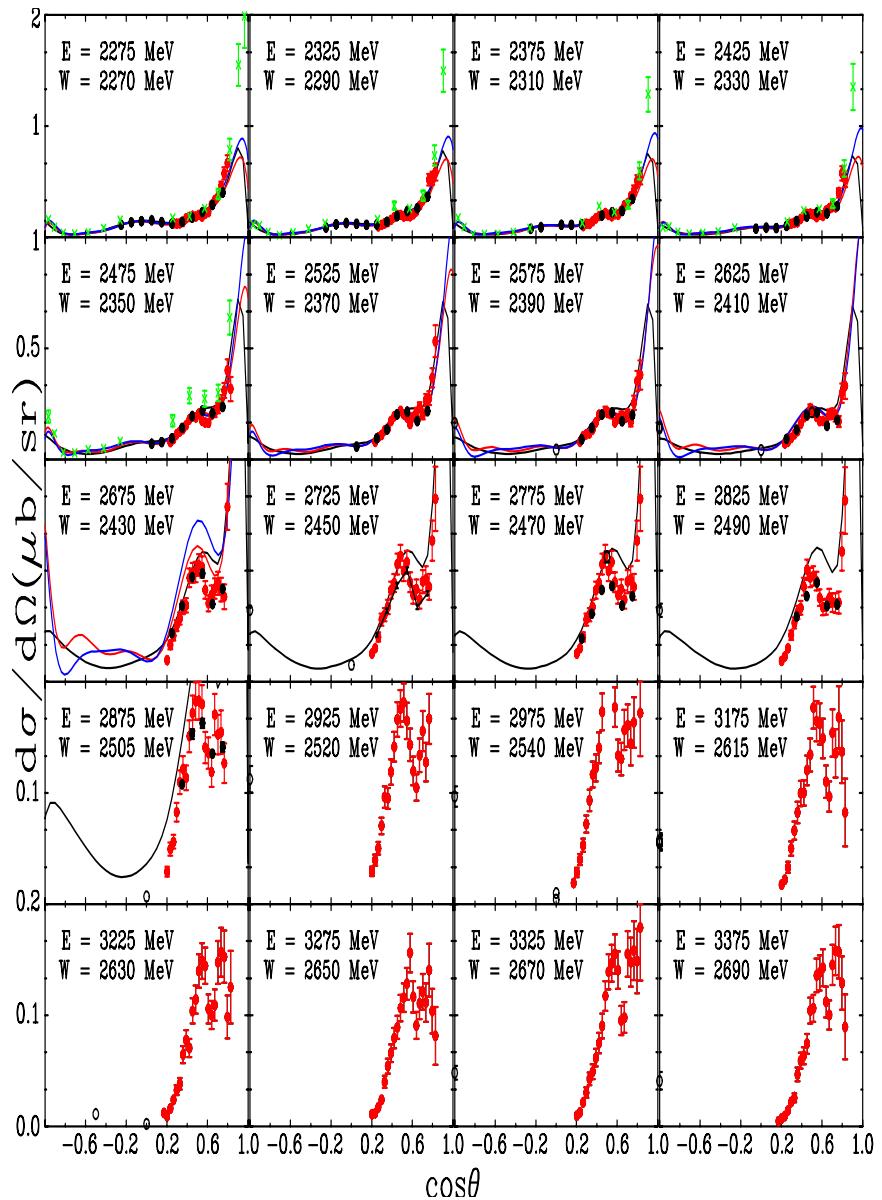


Figure 63: (Color online) The π^0 proton photoproduction cross section at $E_\gamma = 2.275 - 3.375$ GeV versus cosine of the pion center-of-mass production angle. Notation as in Fig. 62.

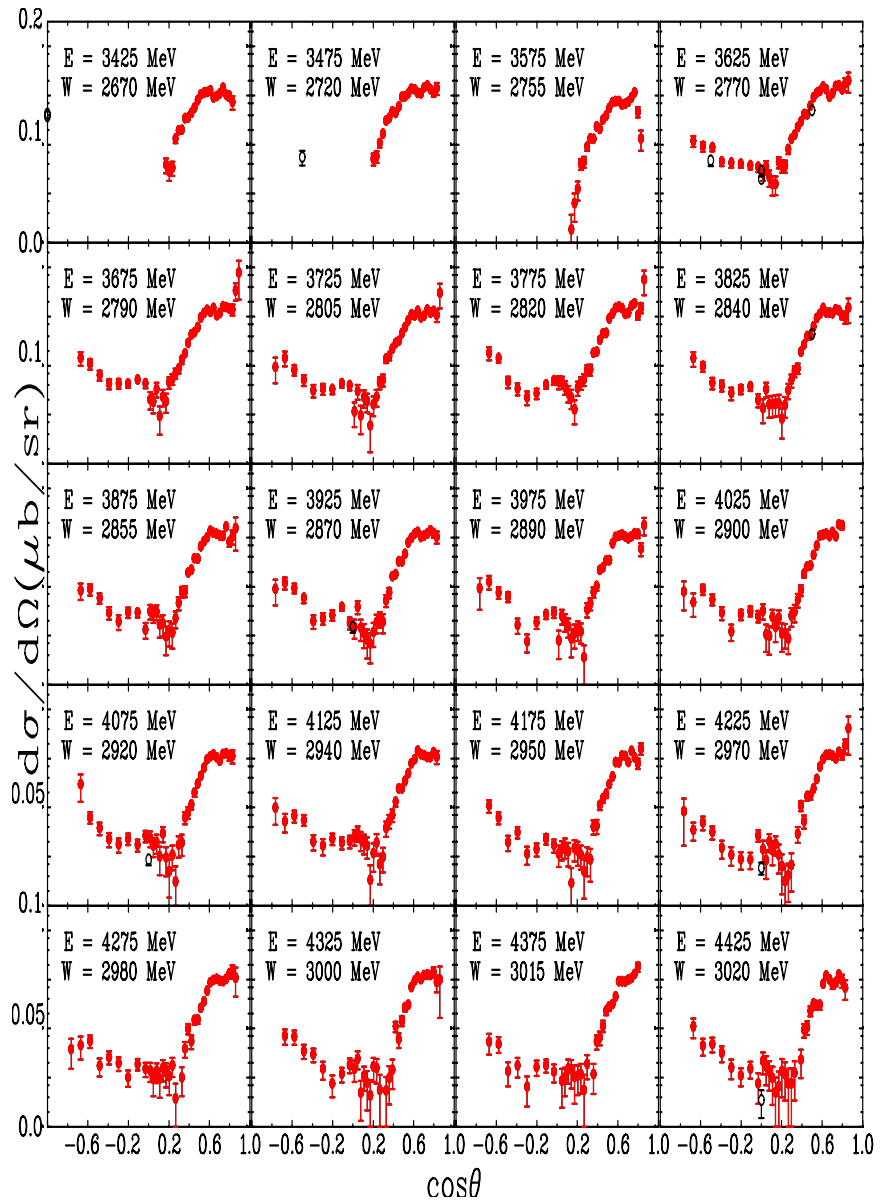


Figure 64: (Color online) The π^0 proton photoproduction cross section at $E_\gamma = 3.425 - 4.425$ GeV versus cosine of the pion center-of-mass production angle. Notation as in Fig. 62.

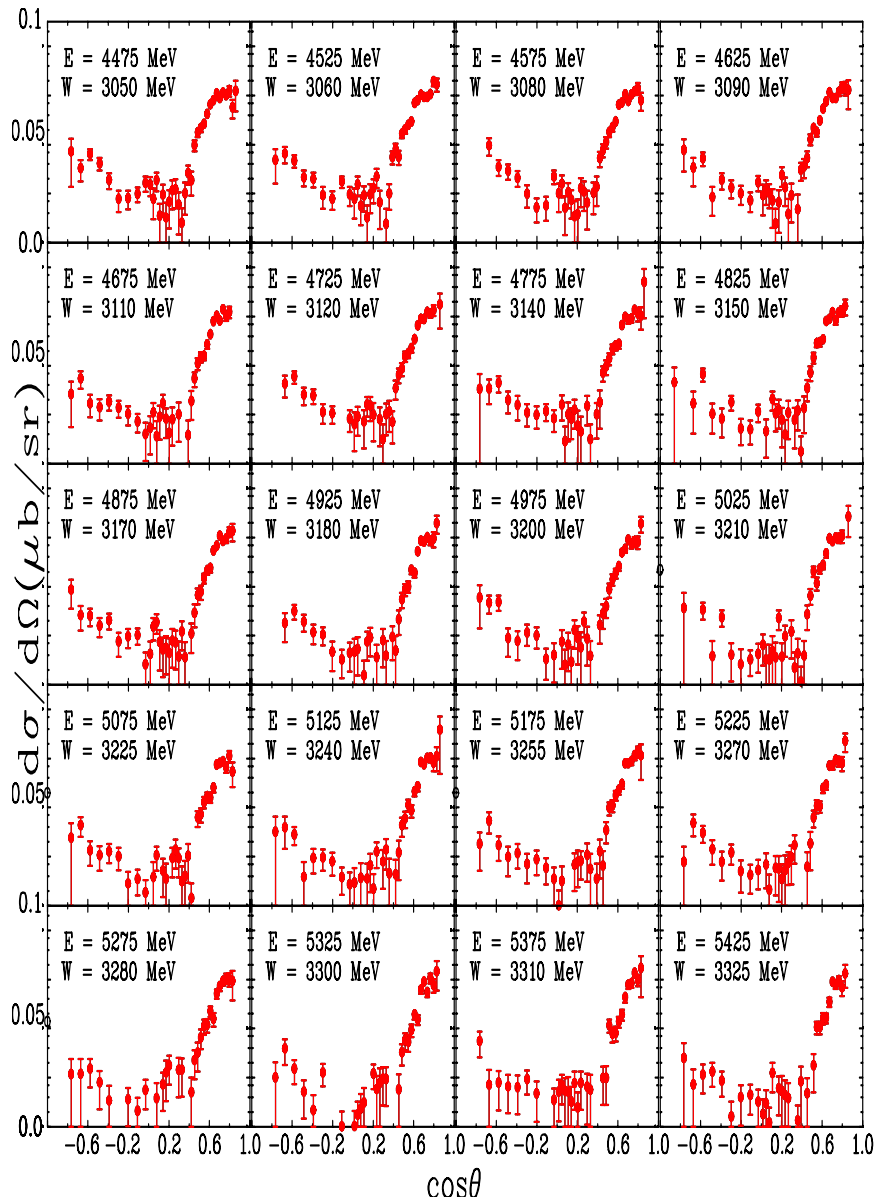


Figure 65: (Color online) The π^0 proton photoproduction cross section at $E_\gamma = 4.475 - 5.425$ GeV versus cosine of the pion center-of-mass production angle. Notation as in Fig. 62.

8.4.2 Excitation Functions

The excitation functions $\frac{d\sigma}{d\Omega}$ at fixed θ are illustrated in Figs. 66, 67. A brief discussion is written in Sec. 8.4.5.

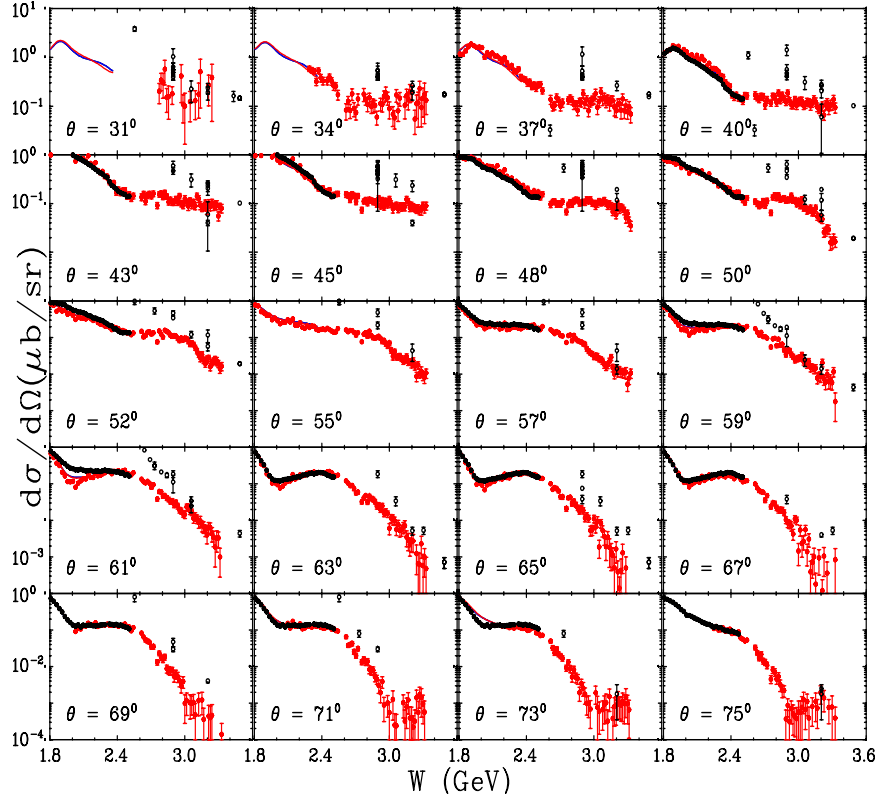


Figure 66: (Color online) Fixed angle excitation functions of the π^0 photoproduction cross section, $(d\sigma/d\Omega)$, off the proton at $\theta = 31 - 75^\circ$ versus center-of-mass total energy W . The pion center-of-mass production angle is shown. Plotted uncertainties are statistical. The plotted points from previously published experimental data are those data points within $\pm 2^\circ$ of pion center-of-mass production angle indicated on each panel. Notation as in Fig. 62.

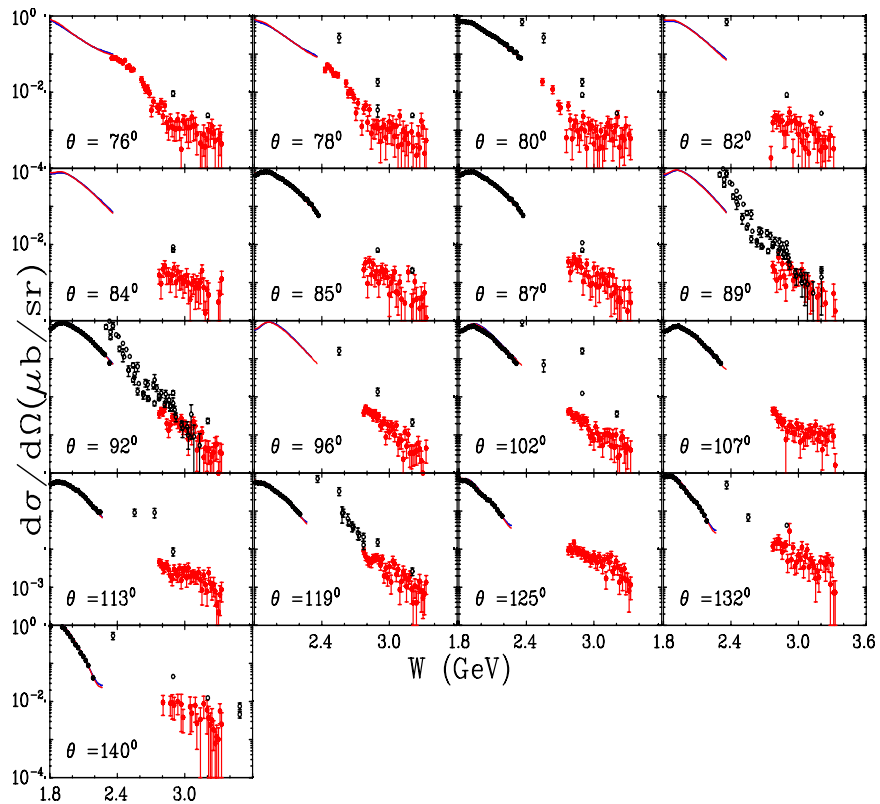


Figure 67: (Color online) Fixed angle excitation functions of the π^0 photo-production cross section, ($d\sigma/d\Omega$), off the proton at $\theta = 76 - 140^\circ$ versus center-of-mass total energy W . Notation as in Fig. 62.

8.4.3 t -Dependence

The t -dependence of $\frac{d\sigma}{dt}$ at fixed E_γ are illustrated in Figs. 68, 69, 70, 71. A brief discussion is written in Sec. 8.4.5.

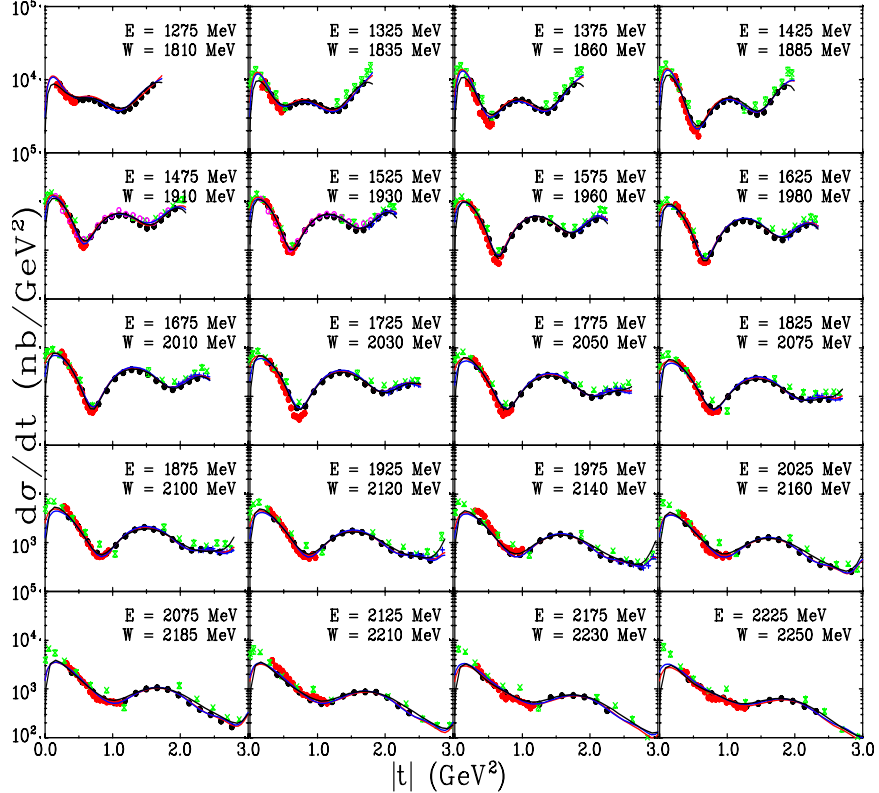


Figure 68: (Color online) π^0 photoproduction cross section, $(d\sigma/dt)$, off the proton at $E_\gamma = 1275 - 2225$ MeV versus momentum transfer t . Notation as in Fig. 62.

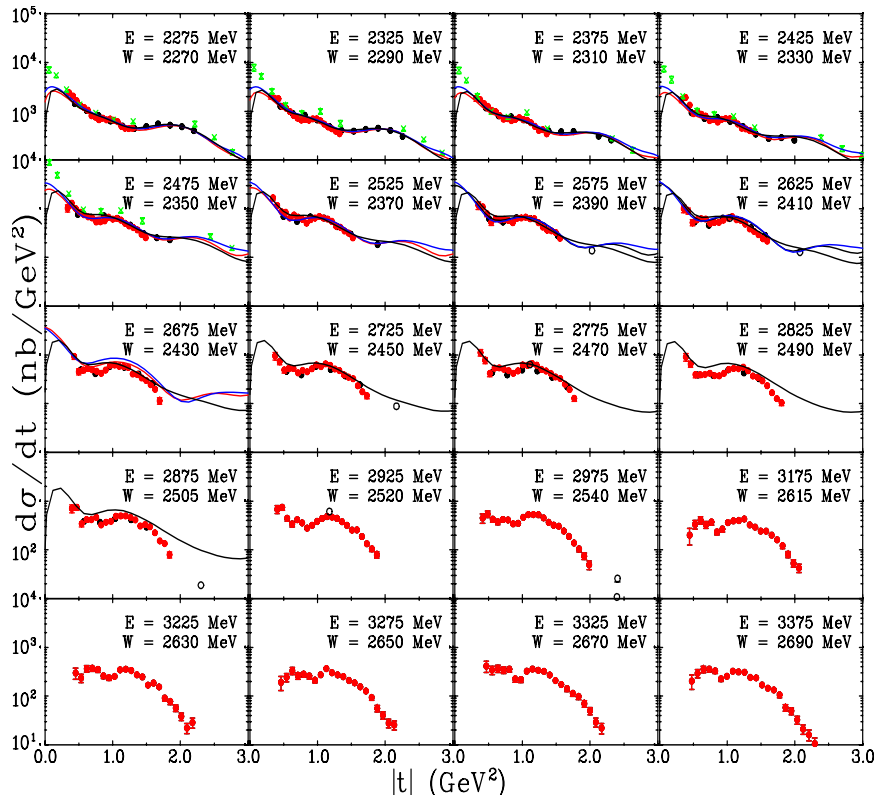


Figure 69: (Color online) π^0 photoproduction cross section, ($d\sigma/dt$), off the proton at $E_\gamma = 2275 - 3375$ MeV versus momentum transfer t . Notation as in Fig. 62.

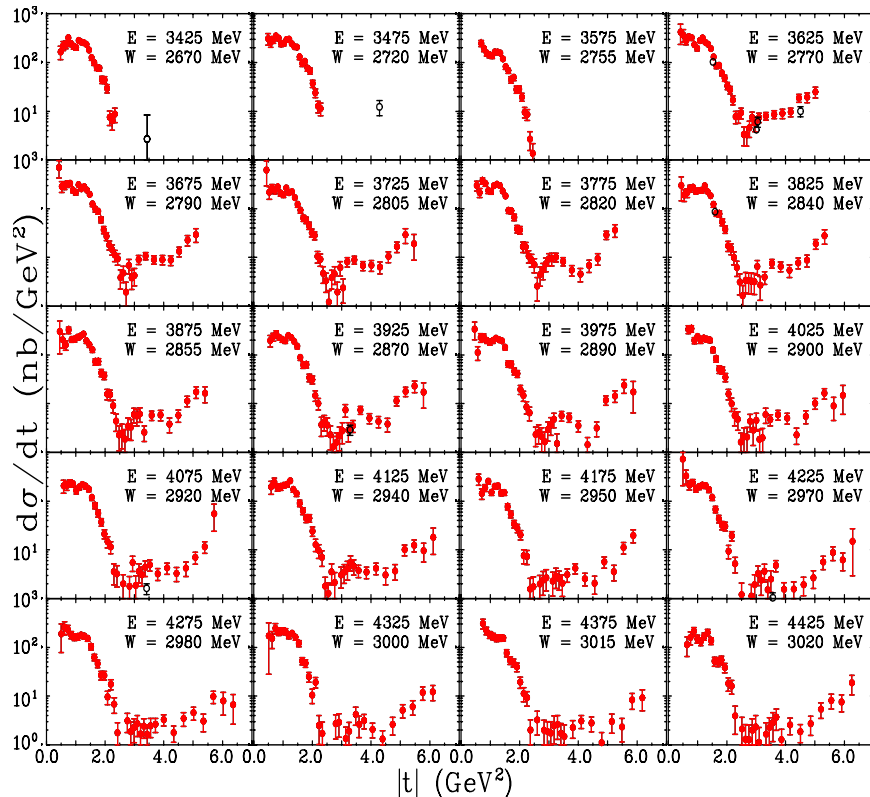


Figure 70: (Color online) π^0 photoproduction cross section, ($d\sigma/dt$), off the proton at $E_\gamma = 3425 - 4425$ MeV versus momentum transfer t . Notation as in Fig. 62.

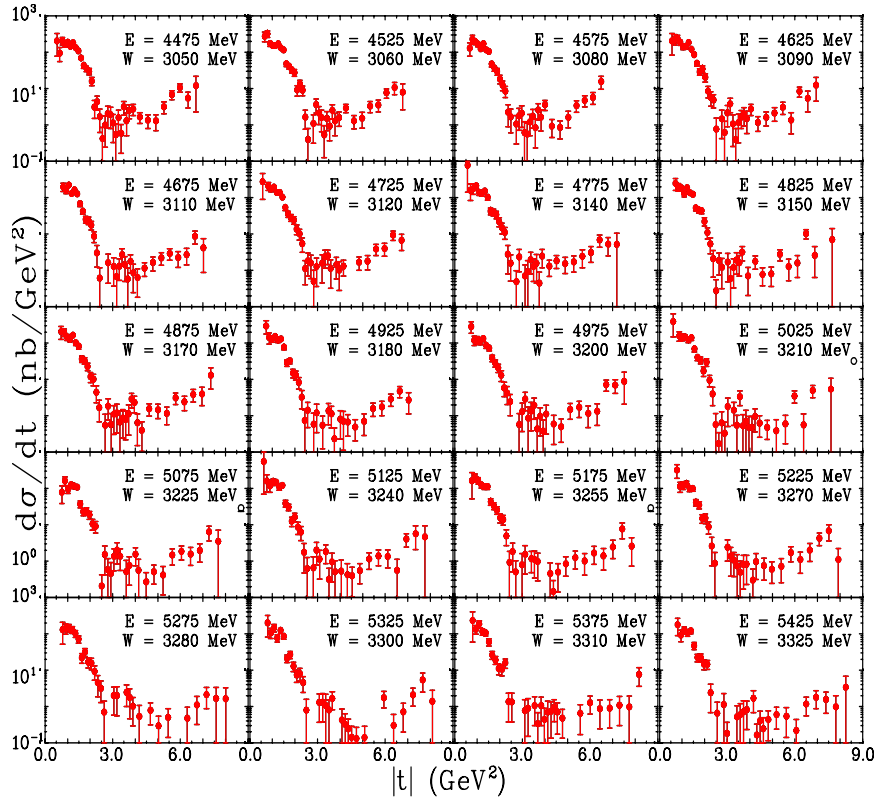


Figure 71: (Color online) π^0 photoproduction cross section, ($d\sigma/dt$), off the proton at $E_\gamma = 4475 - 5425$ MeV versus momentum transfer t . Notation as in Fig. 62.

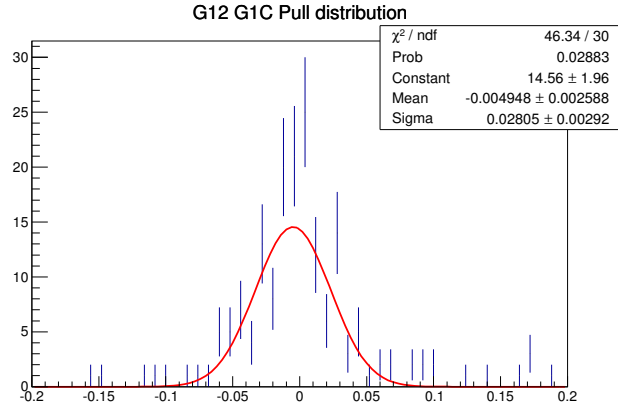


Figure 72: Pull distribution for g12/g1c comparison of data shown in Figs. 62 and 63.

8.4.4 SAID χ^2 Improvements

The measured cross-section presented in this analysis yielded an improvement to the SAID fit. This improvement, in the form of a χ^2/dp , can be seen in Fig. 73, where the new cross-section measurement is depicted in red while the previous is depicted in blue. Decreasing the χ^2/dp reflects the “goodness” of fit and overall quality of fitting the data. This is important because if a fit determines a resonance or change in amplitude, the quality of the fit determines the accuracy of the solution.

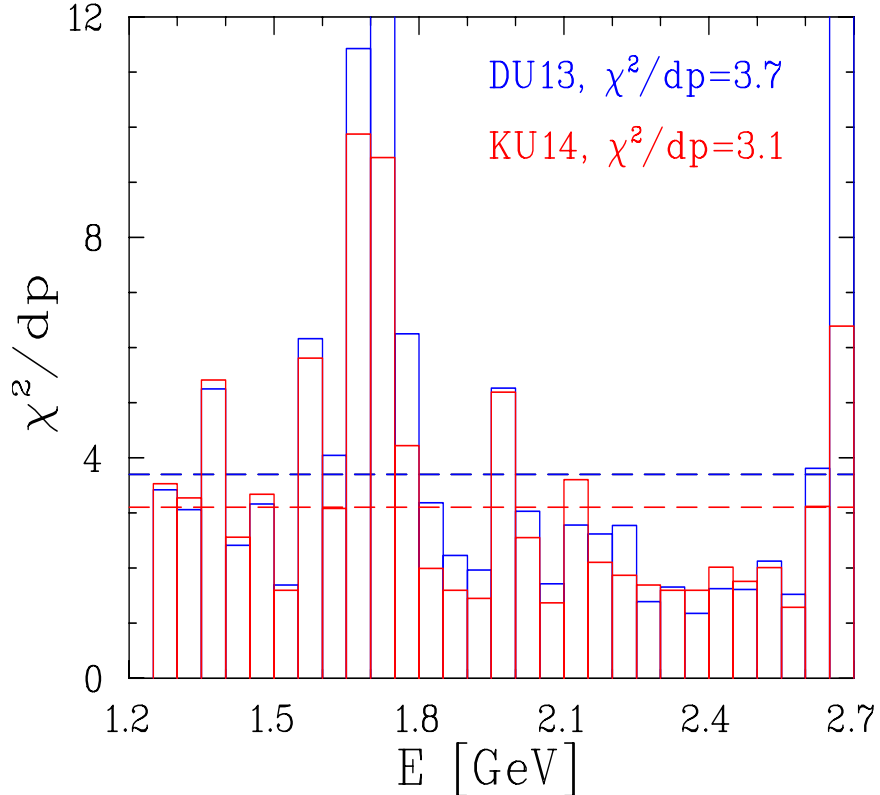


Figure 73: Energy dependence of the χ^2/dp comparison to previous SAID fits. Blue points depict previous DU13 solution, while the red points depict the new KU14 solution.

8.4.5 Discussion of SAID Fits and Comaprision to World Data

This measurement agrees with existing world data at low energy where there are numerous previous measurements. At higher energies there appears to be partial disagreement with [32] from which this data were taken from the untagged bremsstrahlung beam. This disagreement can be seen in some of

the low angle θ excitation functions in Sec. 8.4.2. However, with the same data presented in [32] there is agreement, noticeably at angles $\theta = 89^\circ$ and $\theta = 92^\circ$. Since the excitation function measurements performed in this analysis agree well in the low energy domain and also the data is congruent throughout the θ spectrum, further investigation is needed into the method of [32] to understand where or why the discrepancy exists.

9 Conclusions

This manuscript explained the procedure of collecting data in the CLAS detector for the g12 experiment. Data corrections, kinematic fitting and fiducial cuts were used to clean the data to the order of $\approx 98\%$ signal. Differential cross-sections in two representation, $\frac{d\sigma}{d\Omega}$ and $\frac{d\sigma}{dt}$, were given along with comparisons to the existing world data, comparison existing Bonn-Gatchina fits and new SAID parameterization fits. The cross-sections measured in this analysis agreed well with the existing world data for low incident beam energies, while there was a slight discrepancy with the previous limited high energy cross-sections. The fits using the SAID parametrization yielded a χ^2/dp lower than previous existing fits. The data set explained in this analysis is now 10% of the world data for π^0 photoproduction. More development of theory is need to properly explain π^0 production at incident photon beam energies higher than 2.8 GeV.

References

- [1] V. Mathieu et al. Neutral Pion Photoproduction in a Regge Model. *Phys. Rev.*, D92(7):074013, 2015.
- [2] Stanley J. Brodsky and Glennys R. Farrar. Scaling laws at large transverse momentum. *Phys. Rev. Lett.*, 31:1153–1156, 1973.
- [3] G. Peter Lepage and Stanley J. Brodsky. Exclusive processes in perturbative quantum chromodynamics. *Phys. Rev. D*, 22:2157–2198, 1980.
- [4] P.V. Landshoff and J.C. Polkinghorne. pp elastic scattering at large momentum transfer. *Physics Letters B*, 44(3):293 – 295, 1973.
- [5] R. L. Anderson et al. Comparison of 20 exclusive reactions at large t. *Phys. Rev. D*, 49, 1994.
- [6] W. Chen et al. Measurement of the differential cross section for the reaction $\gamma n \rightarrow \pi^- p$ from deuterium. *Phys. Rev. Lett.*, 103:012301, 2009.
- [7] L. Y. Zhu et al. Cross-section measurement of charged-pion photoproduction from hydrogen and deuterium. *Phys. Rev. Lett.*, 91:022003, 2003.
- [8] R. A. Schumacher and M. M. Sargsian. Scaling and resonances in elementary $K^+ \Lambda$ photoproduction. *Phys. Rev. C*, 83, 2011.
- [9] R. L. Anderson et al. Measurements of exclusive photoproduction processes at large values of t and u from 4 to 7.5 gev. *Phys. Rev. D*, 14:679–697, 1976.
- [10] J. Napolitano et al. Measurement of the differential cross section for the reaction ${}^2\text{H}(\gamma, p)n$ at high photon energies and $\theta_{\text{c.m.}} = 90^\circ$. *Phys. Rev. Lett.*, 61:2530–2533, 1988.
- [11] J. E. Belz et al. Two-body photodisintegration of the deuteron up to 2.8 gev. *Phys. Rev. Lett.*, 74:646–649, 1995.
- [12] C. Bochna et al. Measurements of deuteron photodisintegration up to 4.0 gev. *Phys. Rev. Lett.*, 81:4576–4579, 1998.
- [13] E. C. Schulte and others. Measurement of the high energy two-body deuteron photodisintegration differential cross section. *Phys. Rev. Lett.*, 87, 2001.
- [14] G12 Experimental Group. g12 Analysis Procedures, Statistics and Systematics. Technical report, CLAS-NOTE 2017 - 002, 2017.

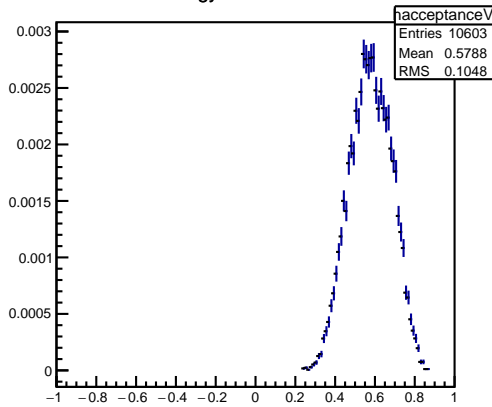
- [15] K.A. Olive et al. Review of particle physics. *Phys. Rev. C*, 38:090001, 2014.
- [16] K. Hicks D. Keller. Techniques in kinematic fitting. *CLAS-NOTE*, 2010-1.
- [17] Wikipedia. Crystal ball function — wikipedia, the free encyclopedia, 2013. [Online; accessed 2-September-2014].
- [18] Dmitry A Romanov. Crystal ball function, 2013. [Online; accessed 2-September-2014].
- [19] R. Bradford and R.A. Schumacher. Liquid hydrogen density in the g1c clas cryotarget. *CLAS-NOTE*, 2002-003.
- [20] I. Frohlich, I. Froehlich, Lorenzo Cazon, T. Galatyuk, V. Hejny, et al. Pluto: A Monte Carlo Simulation Tool for Hadronic Physics. *PoS*, ACAT2007:076, 2007.
- [21] V. Crede et al. Photoproduction of Neutral Pions off Protons. *Phys.Rev.*, C84:055203, 2011.
- [22] Durham Reaction DataBase. Durham reaction database, 2014.
- [23] W.J. Briscoe and others. Institute of Nuclear Studies of The George Washington University Database. <http://gwdac.phys.gwu.edu/>, 2016. Accessed: 2015-12-01.
- [24] Frank A. Haight. *Handbook of the Poisson Distribution*. John Wiley & Sons, 1967.
- [25] Williams M. *Measurement of Differential Cross Sections and Spin Density Matrix Elements along with a Partial Wave Analysis for $\gamma p \rightarrow p\omega$ using CLAS at Jefferson Lab*. Doctoral, Carnegie Mellon University, May 2007.
- [26] M. Dugger et al. Beam asymmetry Σ for π^+ and π^0 photoproduction on the proton for photon energies from 1.102 to 1.862 GeV. *Phys.Rev.*, C88(6):065203, 2013.
- [27] A.V. Anisovich et al. Photoproduction of pions and properties of baryon resonances from a Bonn-Gatchina partial wave analysis. *Eur.Phys.J.*, A44:203–220, 2010.
- [28] M. Dugger et al. pi0 photoproduction on the proton for photon energies from 0.675 to 2.875-GeV. *Phys.Rev.*, C76:025211, 2007.
- [29] O. Bartalini et al. Measurement of pi0 photoproduction on the proton from 550-MeV to 1500-MeV at GRAAL. *Eur.Phys.J.*, A26:399–419, 2005.

- [30] M. Sumihama et al. Backward-angle photoproduction of pi0 mesons on the proton at $E_{\gamma} = 1.5\text{-}2.4\text{-GeV}$. *Phys.Lett.*, B657:32–37, 2007.
- [31] O. Bartholomy et al. Neutral pion photoproduction off protons in the energy range $0.3\text{-GeV} < E(\gamma) < 3\text{-GeV}$. *Phys.Rev.Lett.*, 94:012003, 2005.
- [32] M. Braunschweig et al. Single photoproduction of neutral π -mesons on hydrogen at small angles between 4 and 5.8 gev. *Physics Letters B*, 26(6):405 – 409, 1968.

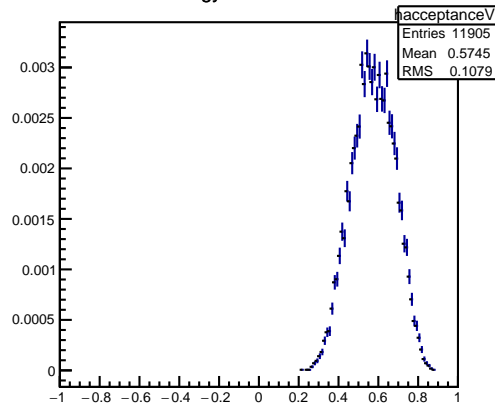
10 Appendix I

10.1 Acceptance plots

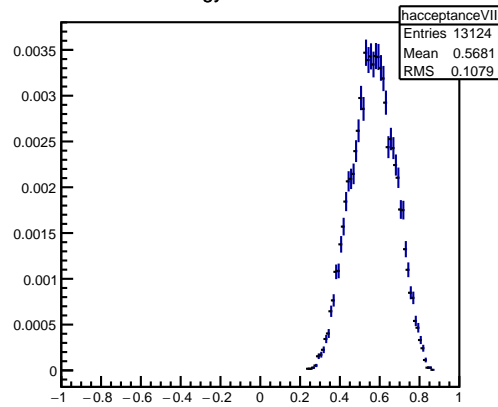
Beam Energy $1.275 \text{ GeV} \pm 25\text{MeV}$



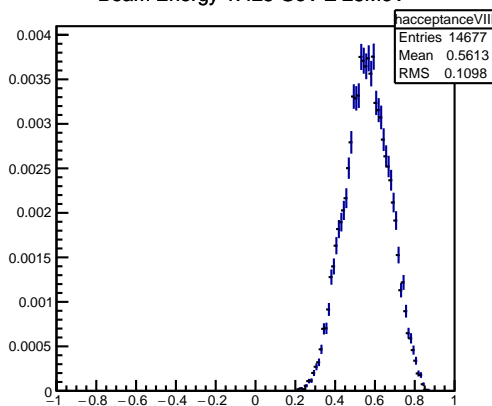
Beam Energy $1.325 \text{ GeV} \pm 25\text{MeV}$



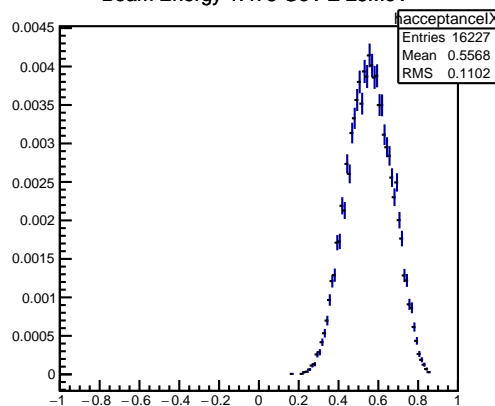
Beam Energy $1.375 \text{ GeV} \pm 25\text{MeV}$



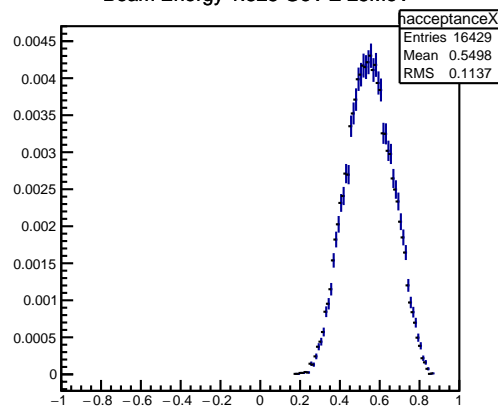
Beam Energy $1.425 \text{ GeV} \pm 25\text{MeV}$



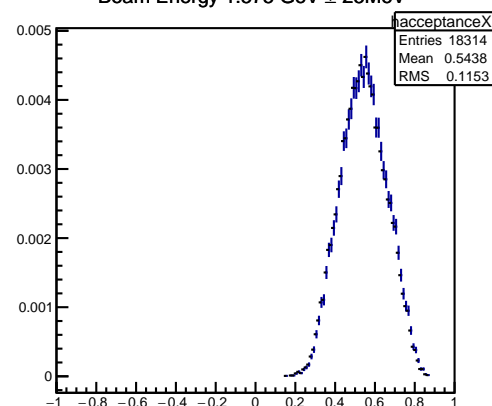
Beam Energy $1.475 \text{ GeV} \pm 25\text{MeV}$



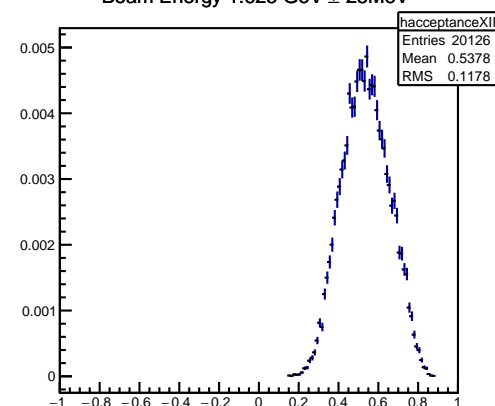
Beam Energy $1.525 \text{ GeV} \pm 25\text{MeV}$



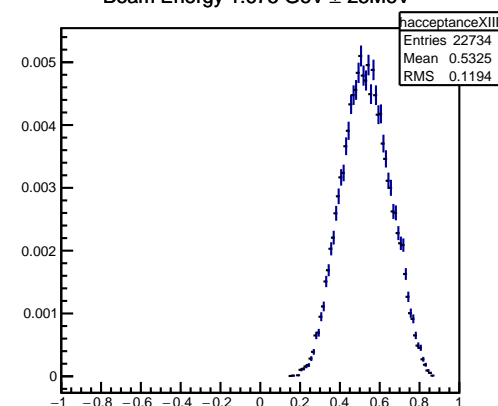
Beam Energy $1.575 \text{ GeV} \pm 25\text{MeV}$



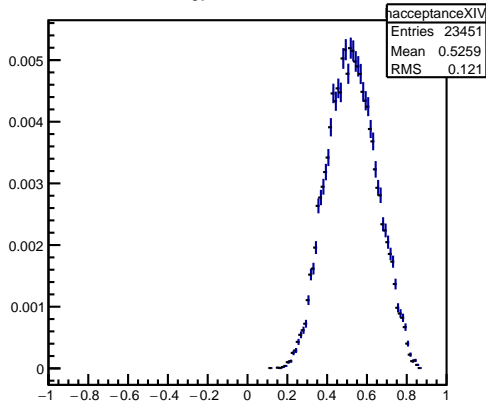
Beam Energy $1.625 \text{ GeV} \pm 25\text{MeV}$



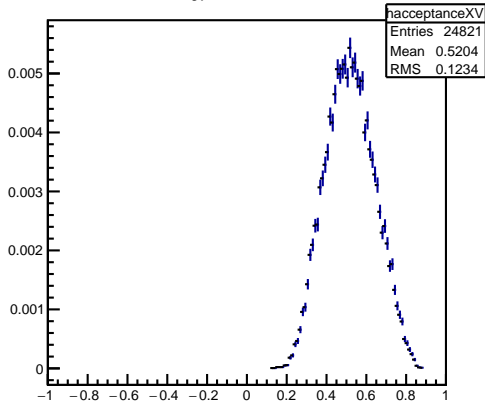
Beam Energy $1.675 \text{ GeV} \pm 25\text{MeV}$



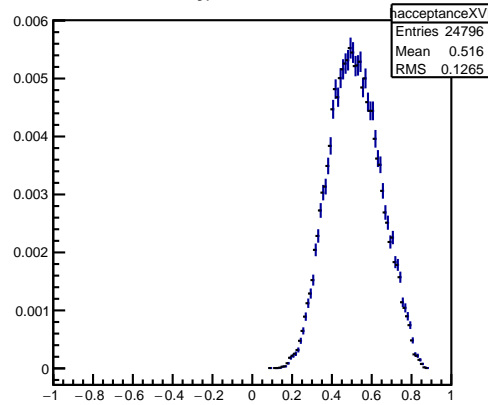
Beam Energy $1.725 \text{ GeV} \pm 25\text{MeV}$



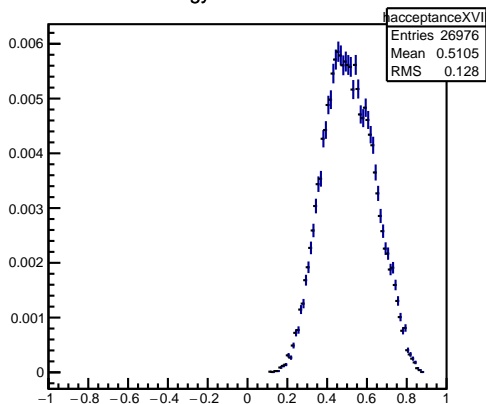
Beam Energy $1.775 \text{ GeV} \pm 25\text{MeV}$



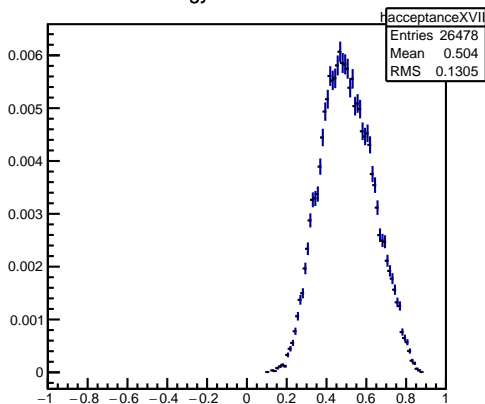
Beam Energy $1.825 \text{ GeV} \pm 25\text{MeV}$



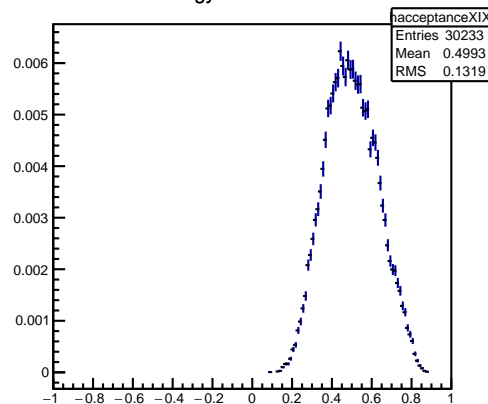
Beam Energy $1.875 \text{ GeV} \pm 25\text{MeV}$



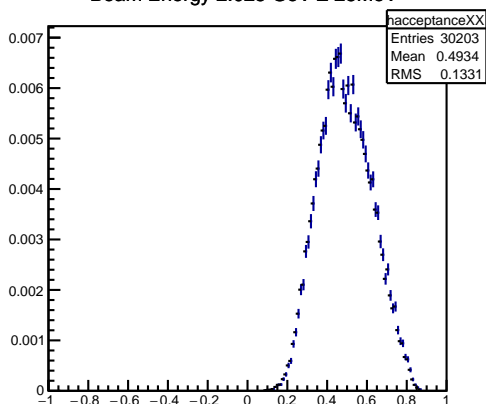
Beam Energy $1.925 \text{ GeV} \pm 25\text{MeV}$



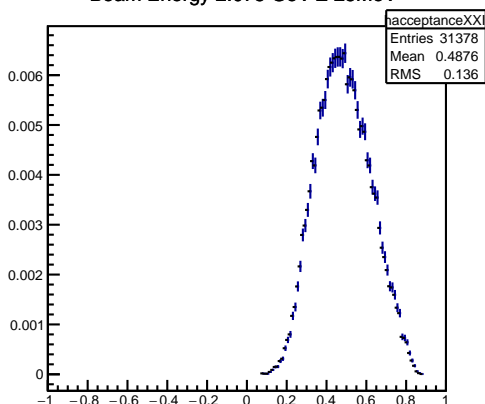
Beam Energy $1.975 \text{ GeV} \pm 25\text{MeV}$



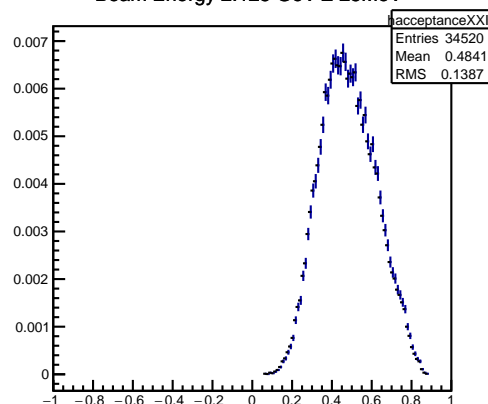
Beam Energy $2.025 \text{ GeV} \pm 25\text{MeV}$



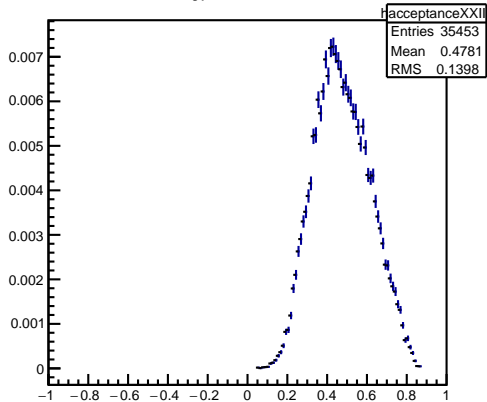
Beam Energy $2.075 \text{ GeV} \pm 25\text{MeV}$



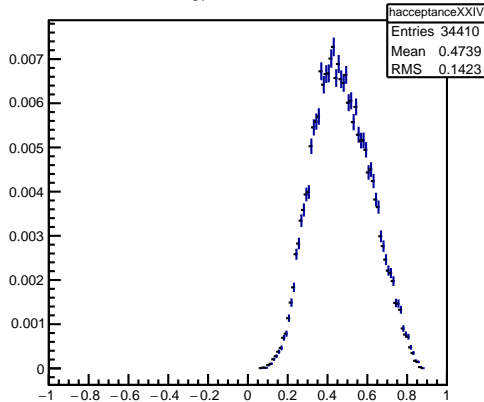
Beam Energy $2.125 \text{ GeV} \pm 25\text{MeV}$



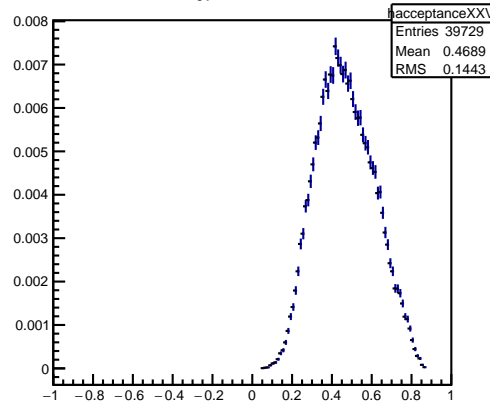
Beam Energy $2.175 \text{ GeV} \pm 25\text{MeV}$



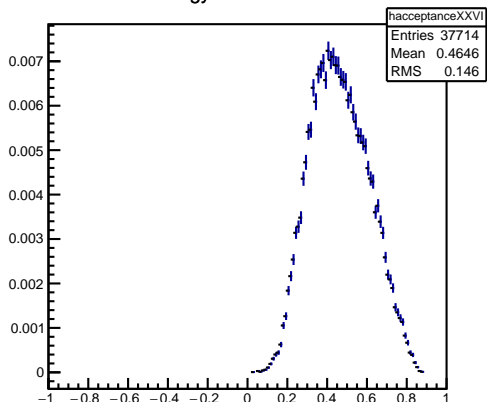
Beam Energy $2.225 \text{ GeV} \pm 25\text{MeV}$



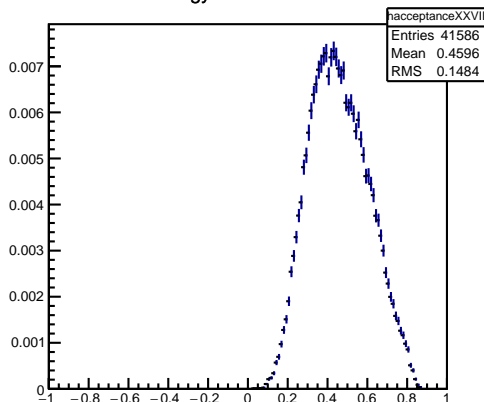
Beam Energy $2.275 \text{ GeV} \pm 25\text{MeV}$



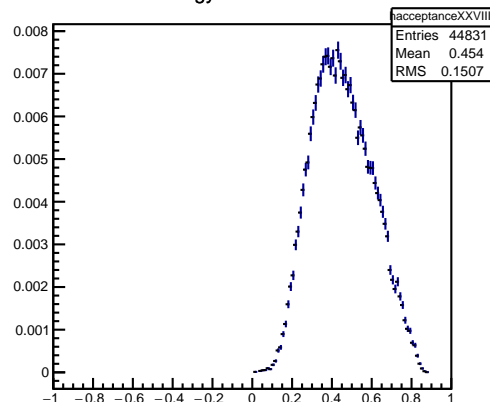
Beam Energy $2.325 \text{ GeV} \pm 25\text{MeV}$



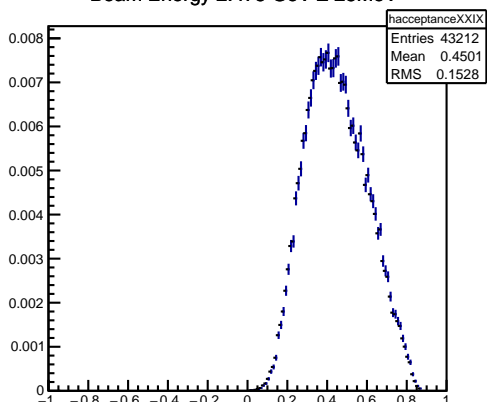
Beam Energy $2.375 \text{ GeV} \pm 25\text{MeV}$



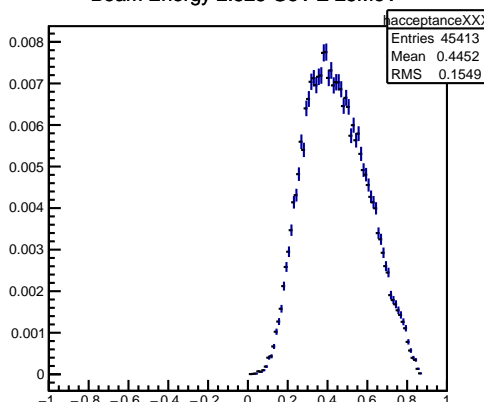
Beam Energy $2.425 \text{ GeV} \pm 25\text{MeV}$



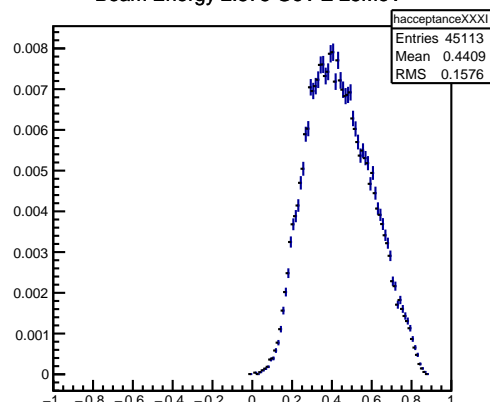
Beam Energy $2.475 \text{ GeV} \pm 25\text{MeV}$



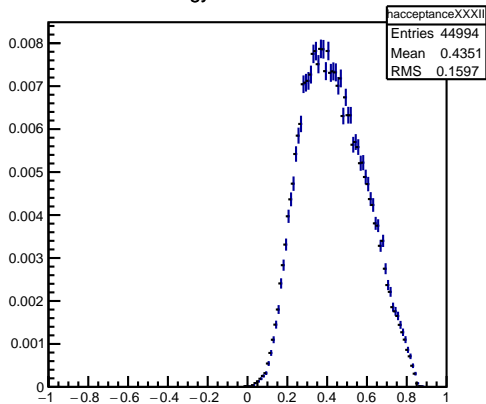
Beam Energy $2.525 \text{ GeV} \pm 25\text{MeV}$



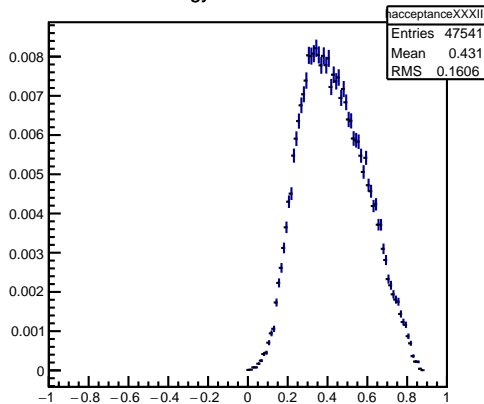
Beam Energy $2.575 \text{ GeV} \pm 25\text{MeV}$



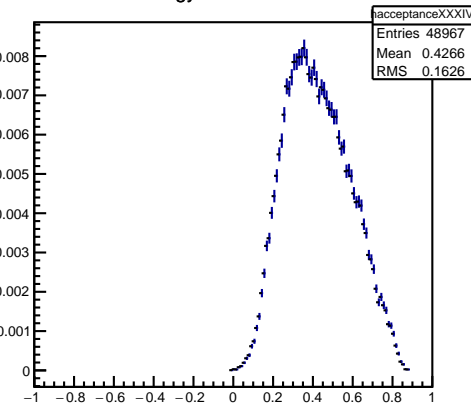
Beam Energy $2.625 \text{ GeV} \pm 25\text{MeV}$



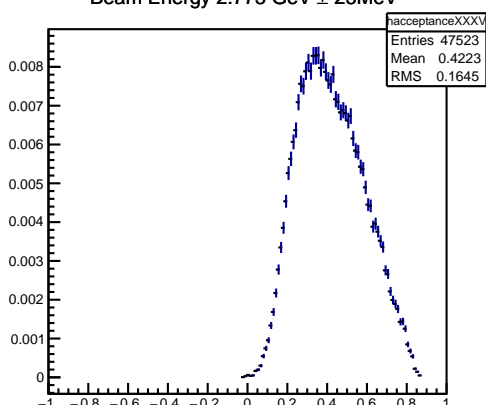
Beam Energy $2.675 \text{ GeV} \pm 25\text{MeV}$



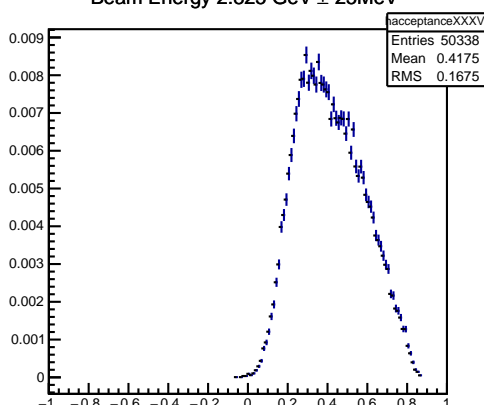
Beam Energy $2.725 \text{ GeV} \pm 25\text{MeV}$



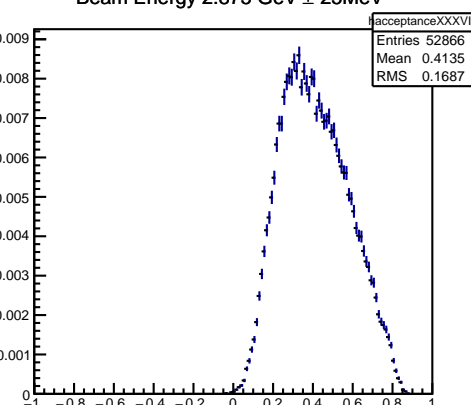
Beam Energy $2.775 \text{ GeV} \pm 25\text{MeV}$



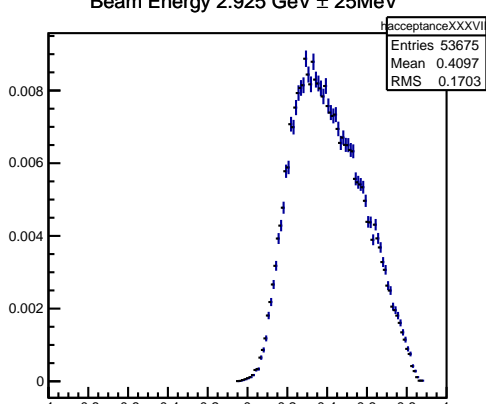
Beam Energy $2.825 \text{ GeV} \pm 25\text{MeV}$



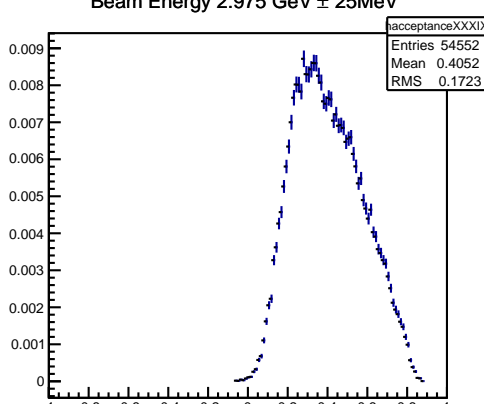
Beam Energy $2.875 \text{ GeV} \pm 25\text{MeV}$



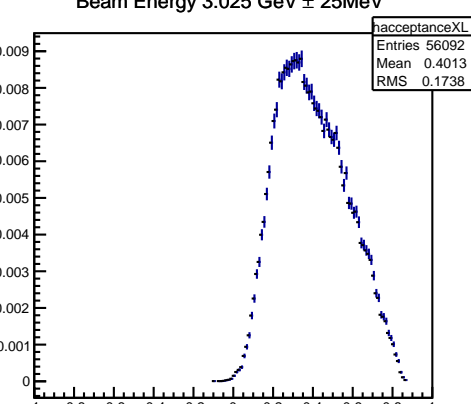
Beam Energy $2.925 \text{ GeV} \pm 25\text{MeV}$



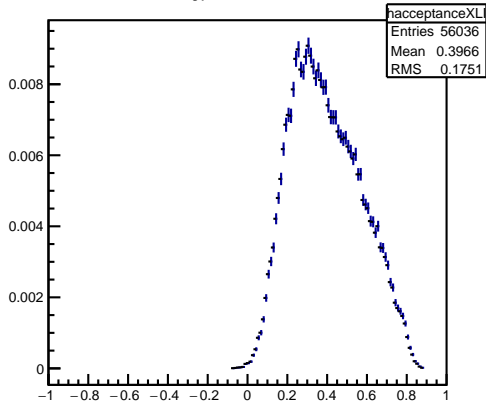
Beam Energy $2.975 \text{ GeV} \pm 25\text{MeV}$



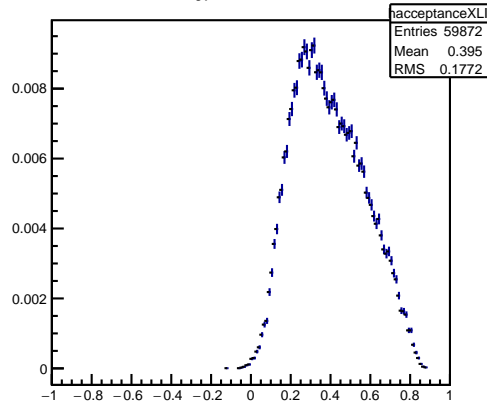
Beam Energy $3.025 \text{ GeV} \pm 25\text{MeV}$



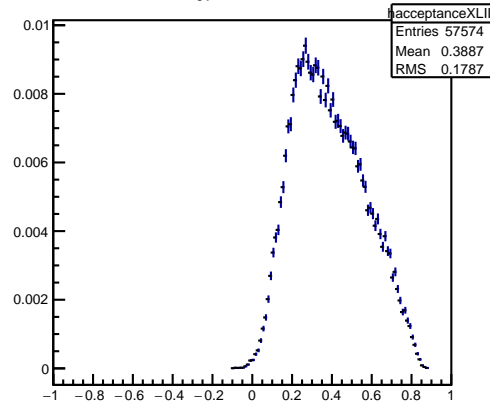
Beam Energy $3.075 \text{ GeV} \pm 25\text{MeV}$



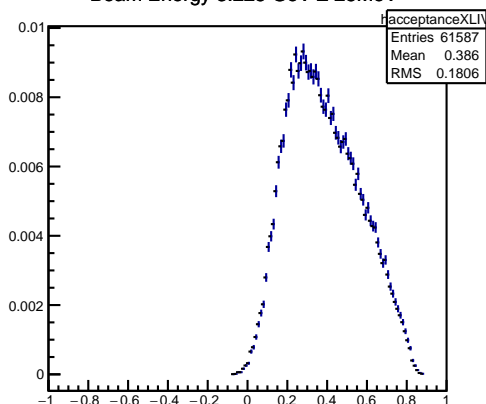
Beam Energy $3.125 \text{ GeV} \pm 25\text{MeV}$



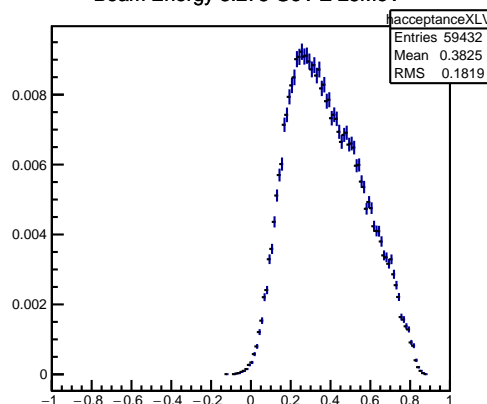
Beam Energy $3.175 \text{ GeV} \pm 25\text{MeV}$



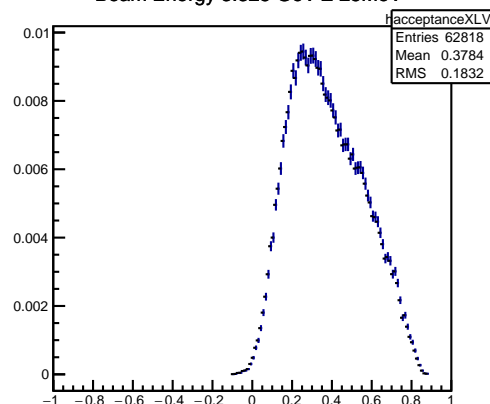
Beam Energy $3.225 \text{ GeV} \pm 25\text{MeV}$



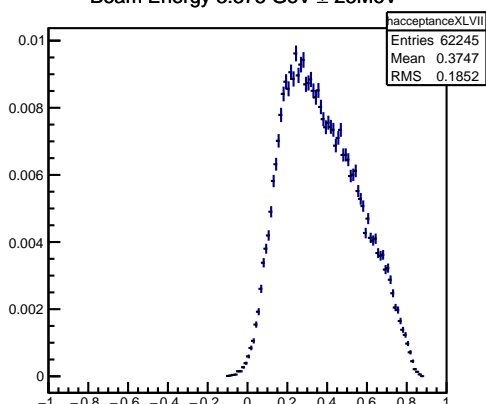
Beam Energy $3.275 \text{ GeV} \pm 25\text{MeV}$



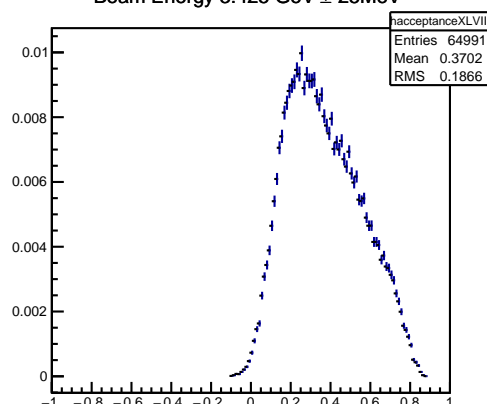
Beam Energy $3.325 \text{ GeV} \pm 25\text{MeV}$



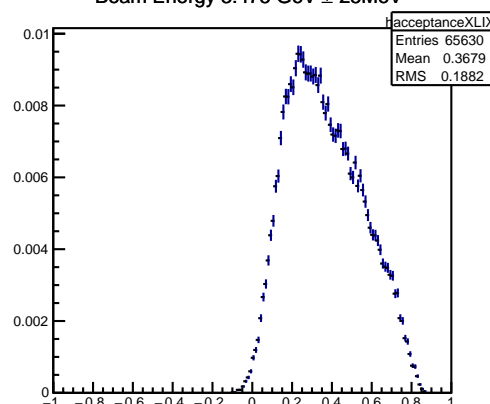
Beam Energy $3.375 \text{ GeV} \pm 25\text{MeV}$



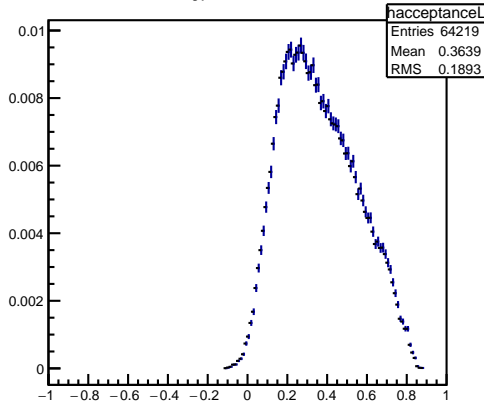
Beam Energy $3.425 \text{ GeV} \pm 25\text{MeV}$



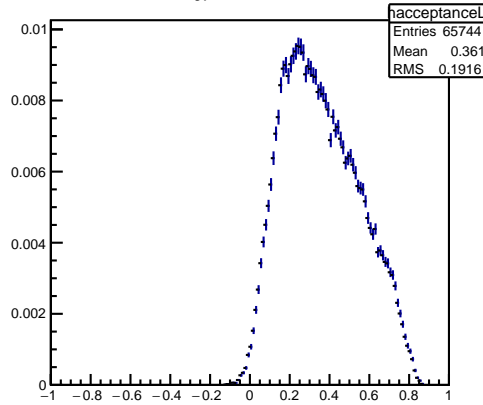
Beam Energy $3.475 \text{ GeV} \pm 25\text{MeV}$



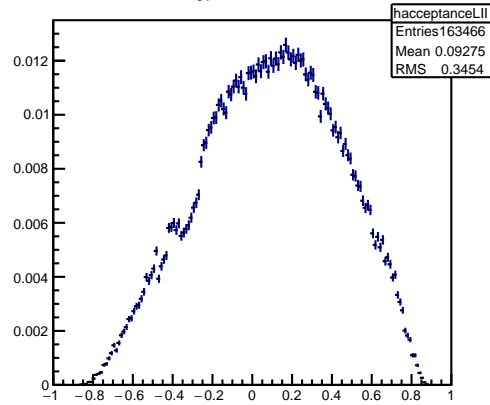
Beam Energy $3.525 \text{ GeV} \pm 25\text{MeV}$



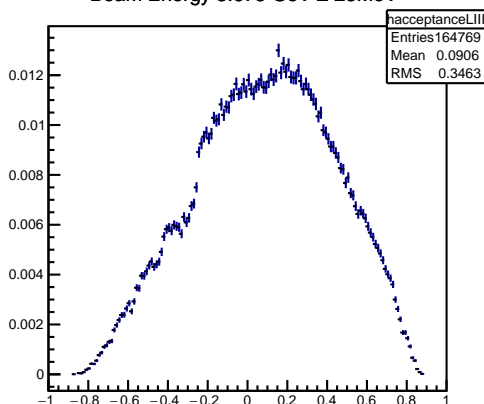
Beam Energy $3.575 \text{ GeV} \pm 25\text{MeV}$



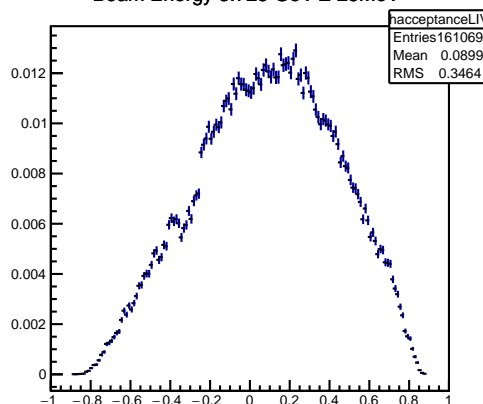
Beam Energy $3.625 \text{ GeV} \pm 25\text{MeV}$



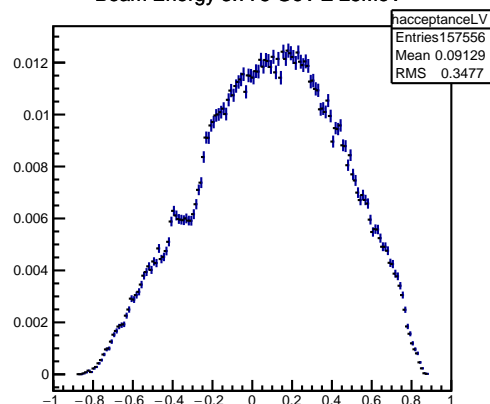
Beam Energy $3.675 \text{ GeV} \pm 25\text{MeV}$



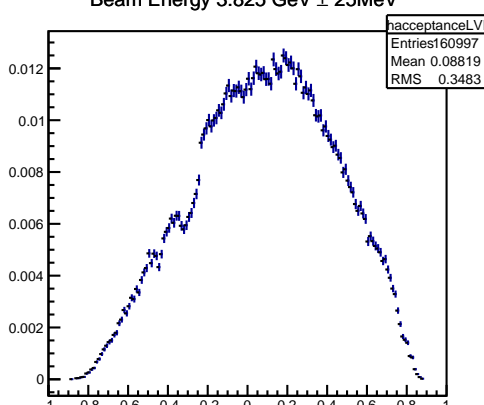
Beam Energy $3.725 \text{ GeV} \pm 25\text{MeV}$



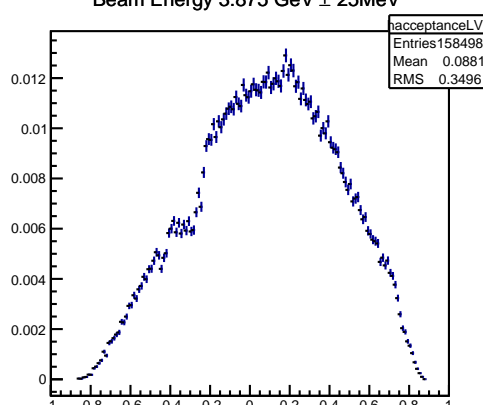
Beam Energy $3.775 \text{ GeV} \pm 25\text{MeV}$



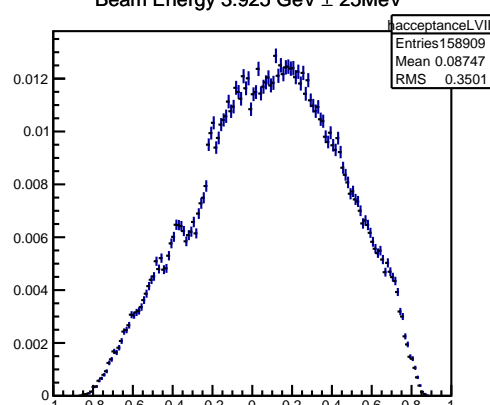
Beam Energy $3.825 \text{ GeV} \pm 25\text{MeV}$



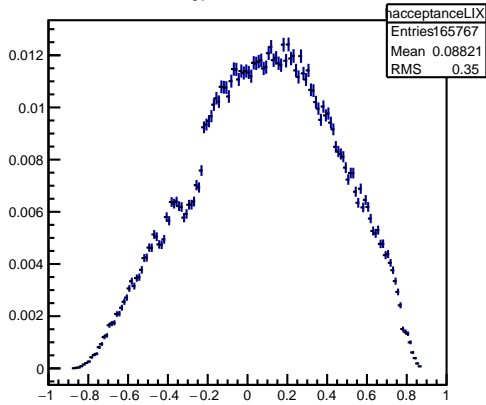
Beam Energy $3.875 \text{ GeV} \pm 25\text{MeV}$



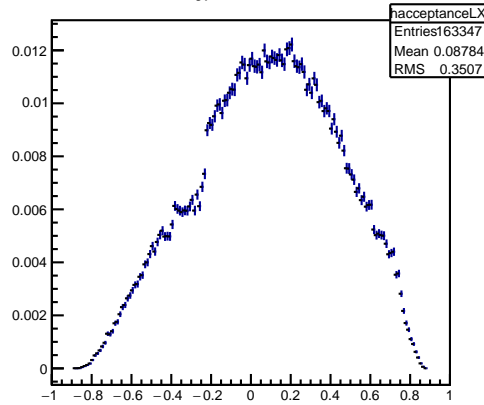
Beam Energy $3.925 \text{ GeV} \pm 25\text{MeV}$



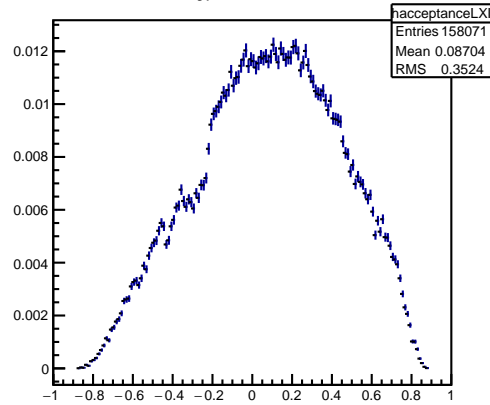
Beam Energy $3.975 \text{ GeV} \pm 25\text{MeV}$



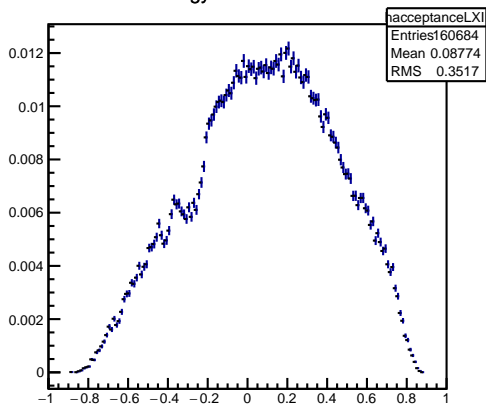
Beam Energy $4.025 \text{ GeV} \pm 25\text{MeV}$



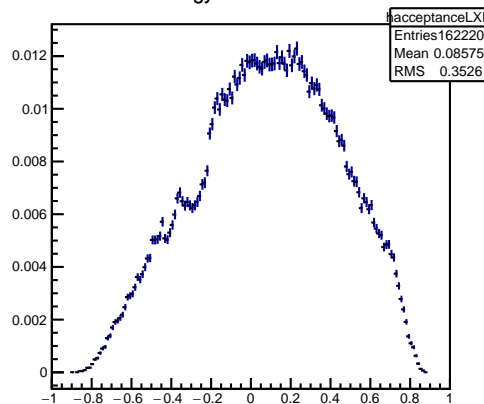
Beam Energy $4.075 \text{ GeV} \pm 25\text{MeV}$



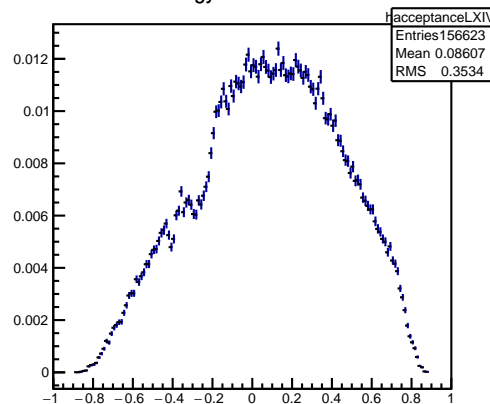
Beam Energy $4.125 \text{ GeV} \pm 25\text{MeV}$



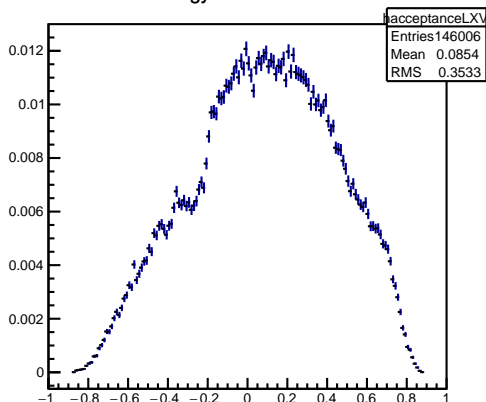
Beam Energy $4.175 \text{ GeV} \pm 25\text{MeV}$



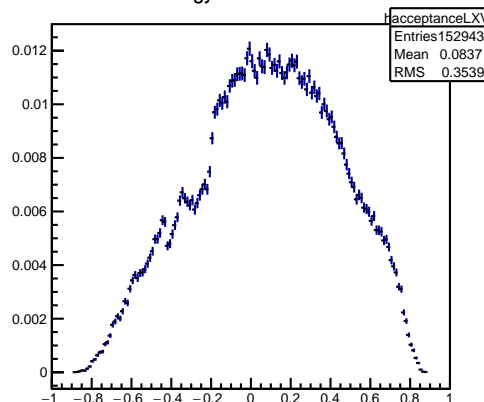
Beam Energy $4.225 \text{ GeV} \pm 25\text{MeV}$



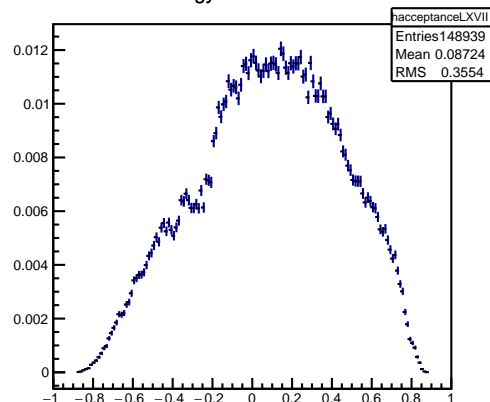
Beam Energy $4.275 \text{ GeV} \pm 25\text{MeV}$



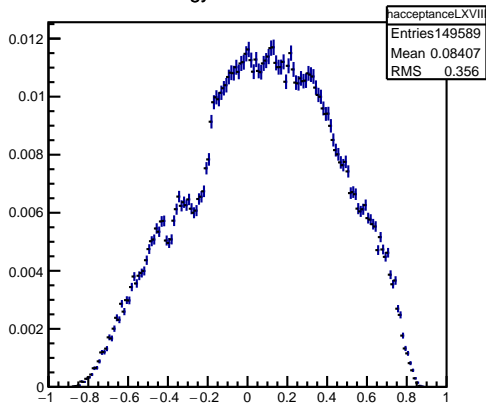
Beam Energy $4.325 \text{ GeV} \pm 25\text{MeV}$



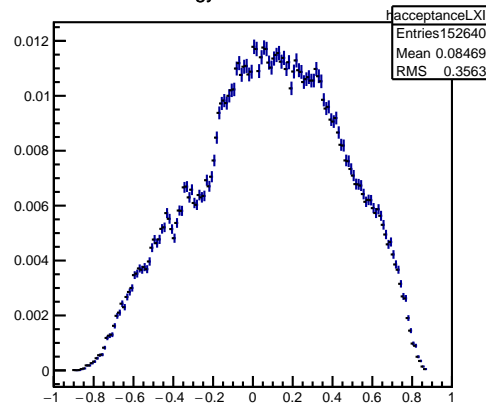
Beam Energy $4.375 \text{ GeV} \pm 25\text{MeV}$



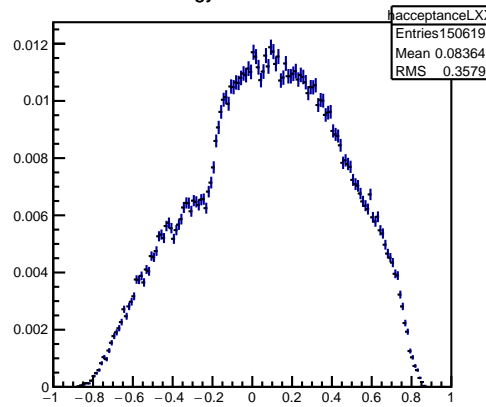
Beam Energy $4.425 \text{ GeV} \pm 25\text{MeV}$



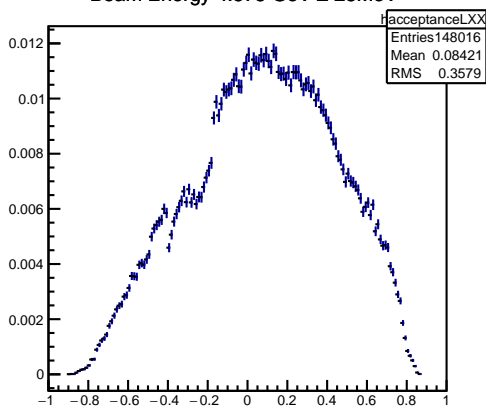
Beam Energy $4.475 \text{ GeV} \pm 25\text{MeV}$



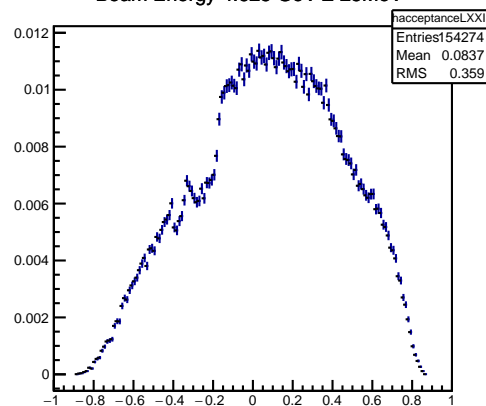
Beam Energy $4.525 \text{ GeV} \pm 25\text{MeV}$



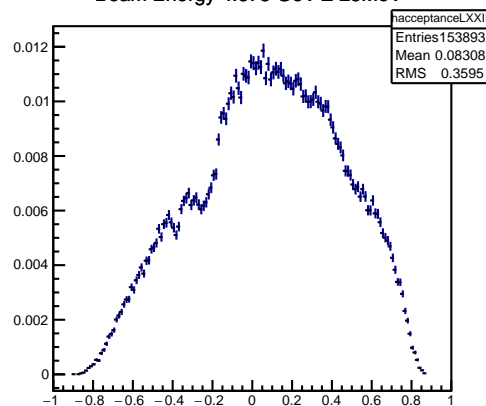
Beam Energy $4.575 \text{ GeV} \pm 25\text{MeV}$



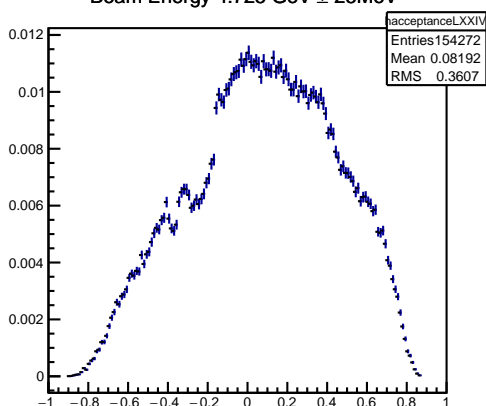
Beam Energy $4.625 \text{ GeV} \pm 25\text{MeV}$



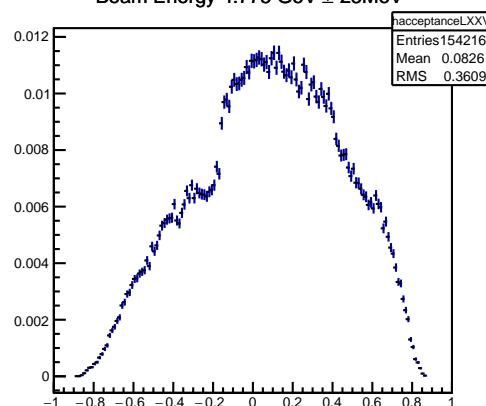
Beam Energy $4.675 \text{ GeV} \pm 25\text{MeV}$



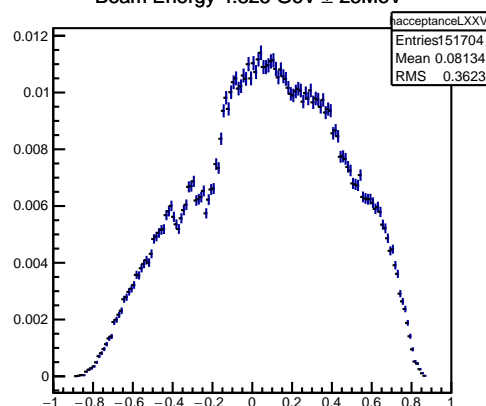
Beam Energy $4.725 \text{ GeV} \pm 25\text{MeV}$



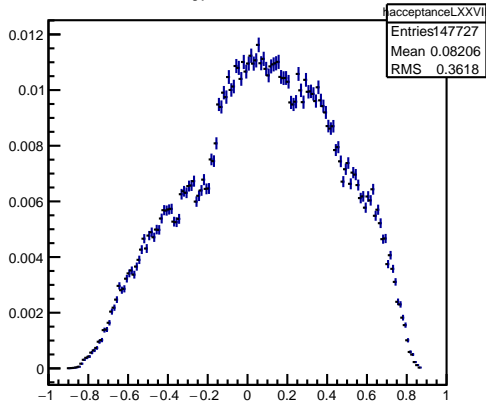
Beam Energy $4.775 \text{ GeV} \pm 25\text{MeV}$



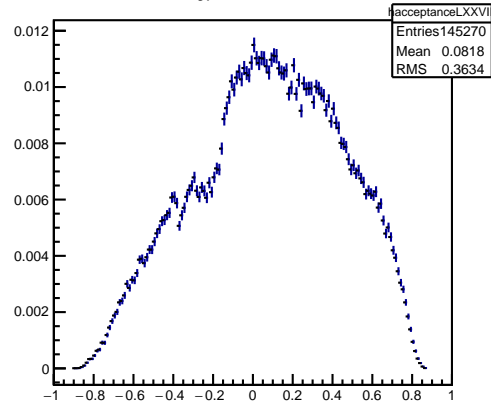
Beam Energy $4.825 \text{ GeV} \pm 25\text{MeV}$



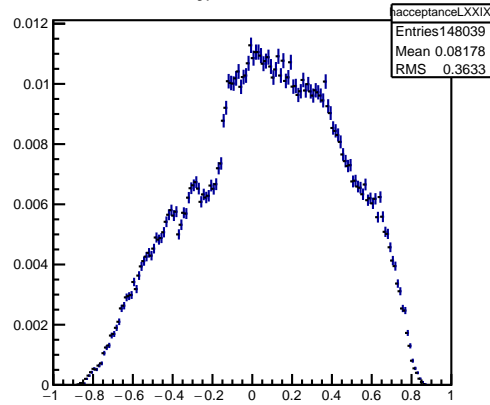
Beam Energy $4.875 \text{ GeV} \pm 25\text{MeV}$



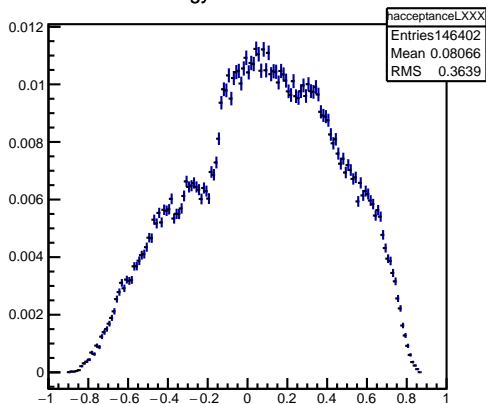
Beam Energy $4.925 \text{ GeV} \pm 25\text{MeV}$



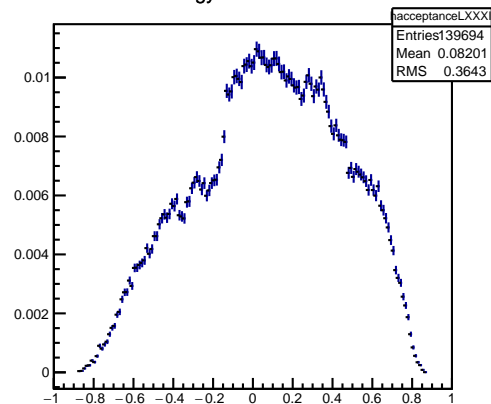
Beam Energy $4.975 \text{ GeV} \pm 25\text{MeV}$



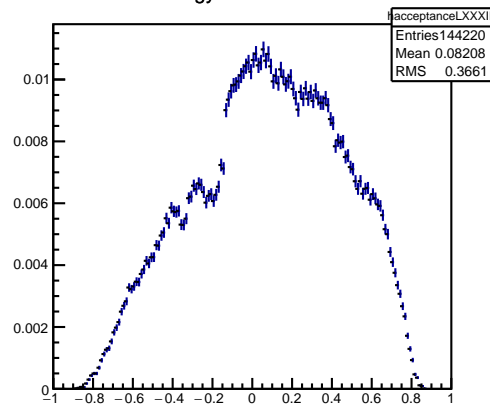
Beam Energy $5.025 \text{ GeV} \pm 25\text{MeV}$



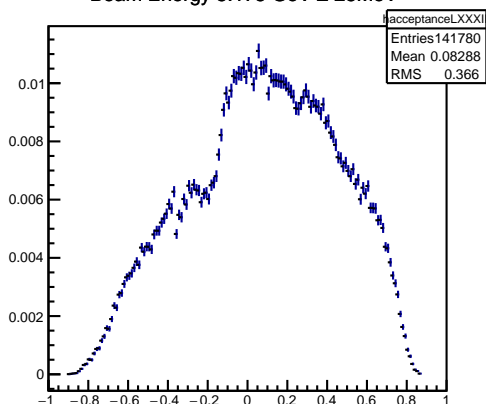
Beam Energy $5.075 \text{ GeV} \pm 25\text{MeV}$



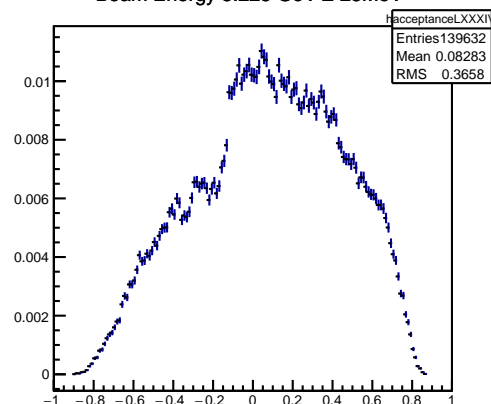
Beam Energy $5.125 \text{ GeV} \pm 25\text{MeV}$



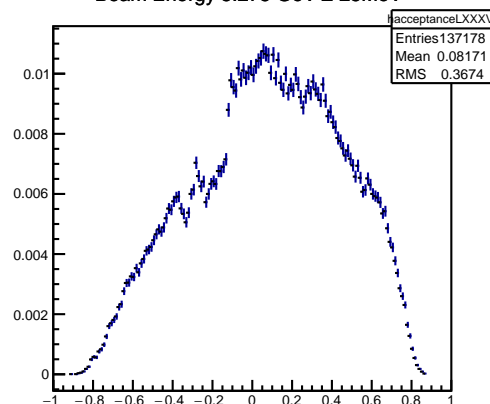
Beam Energy $5.175 \text{ GeV} \pm 25\text{MeV}$



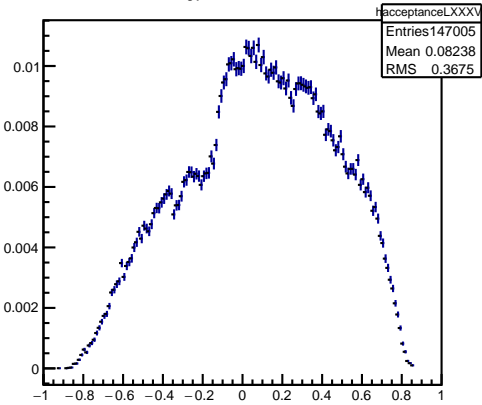
Beam Energy $5.225 \text{ GeV} \pm 25\text{MeV}$



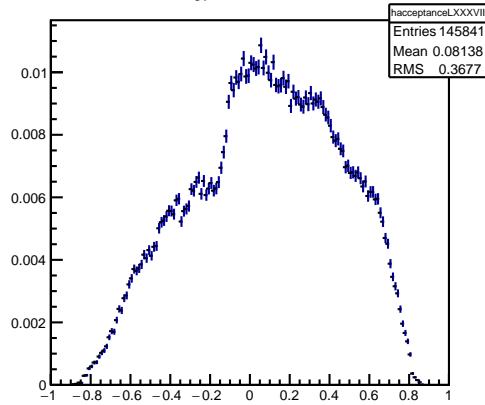
Beam Energy $5.275 \text{ GeV} \pm 25\text{MeV}$



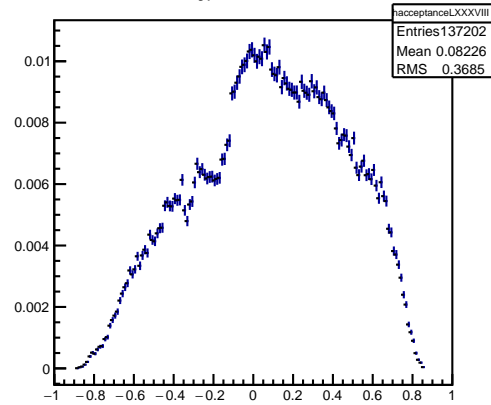
Beam Energy $5.325 \text{ GeV} \pm 25\text{MeV}$



Beam Energy $5.375 \text{ GeV} \pm 25\text{MeV}$



Beam Energy $5.425 \text{ GeV} \pm 25\text{MeV}$



10.2 Acceptance plots

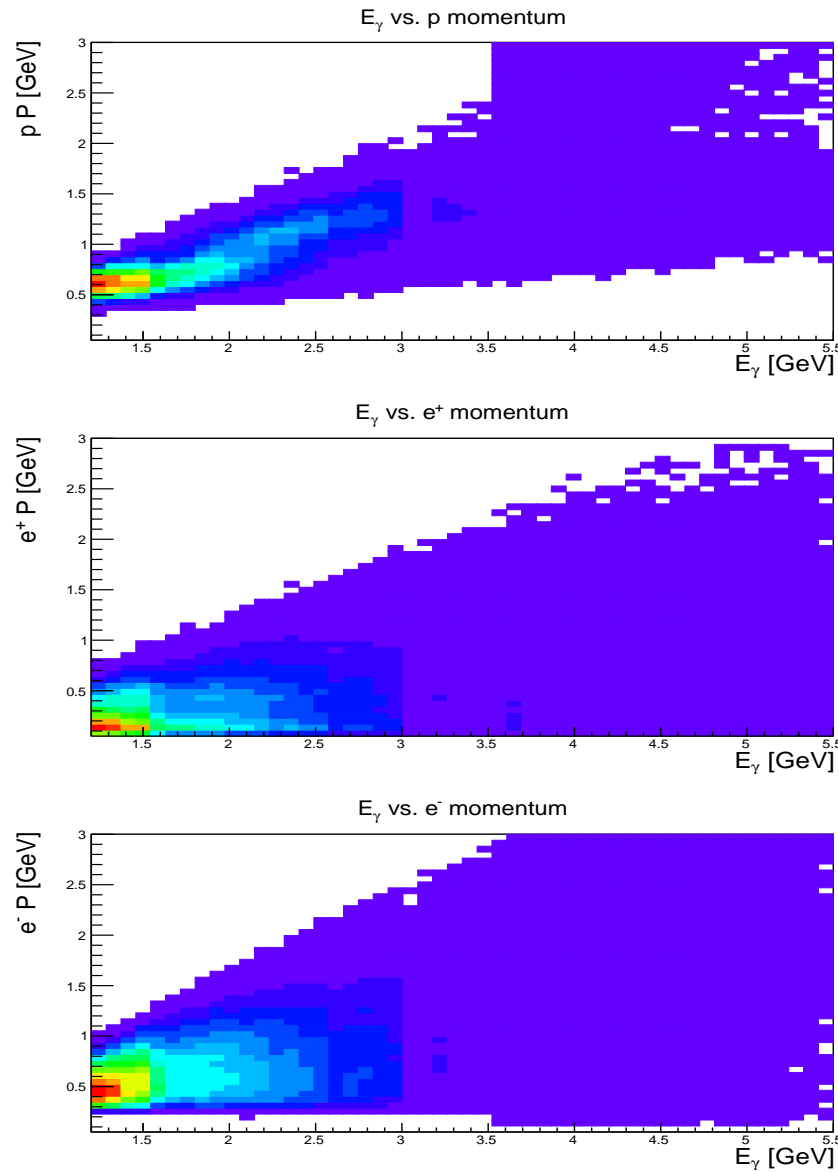


Figure 74: Momentum vs. E_γ for proton (top), e^+ (middle), and e^- (bottom).

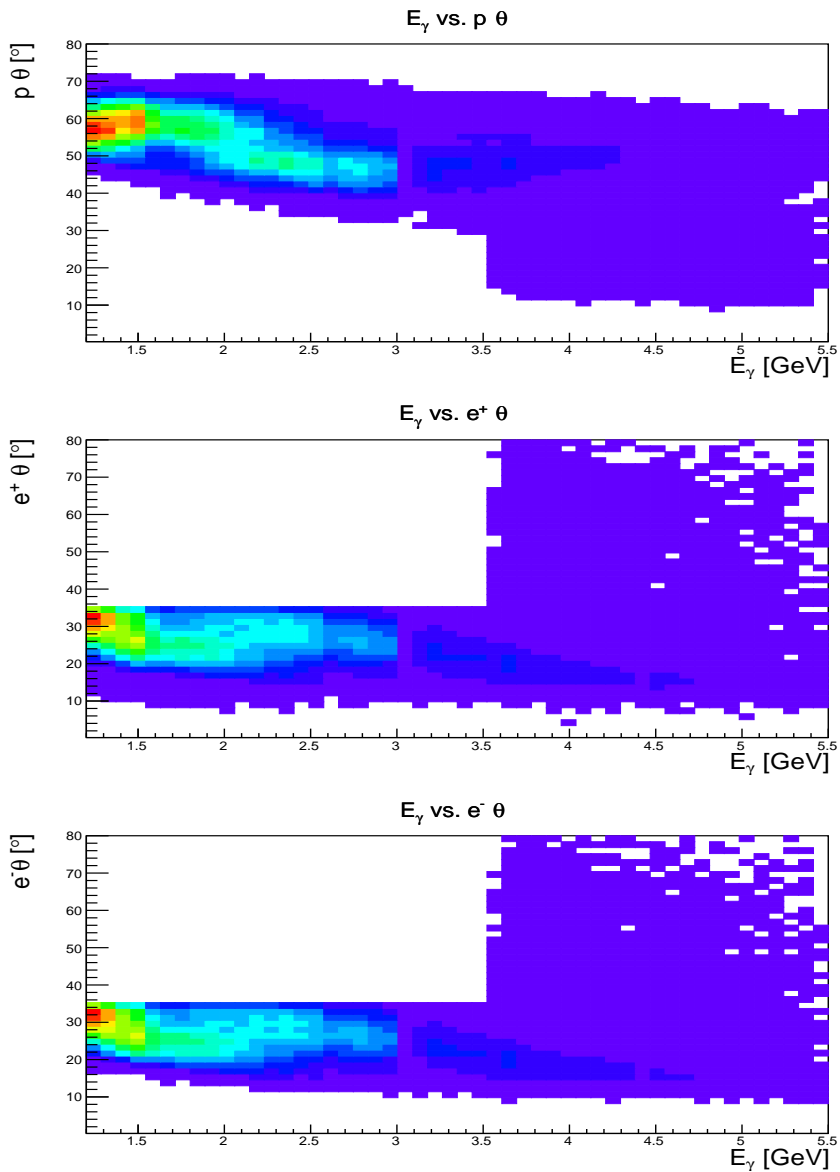


Figure 75: θ_{lab} vs. E_γ for proton (top), e^+ (middle), and e^- (bottom).

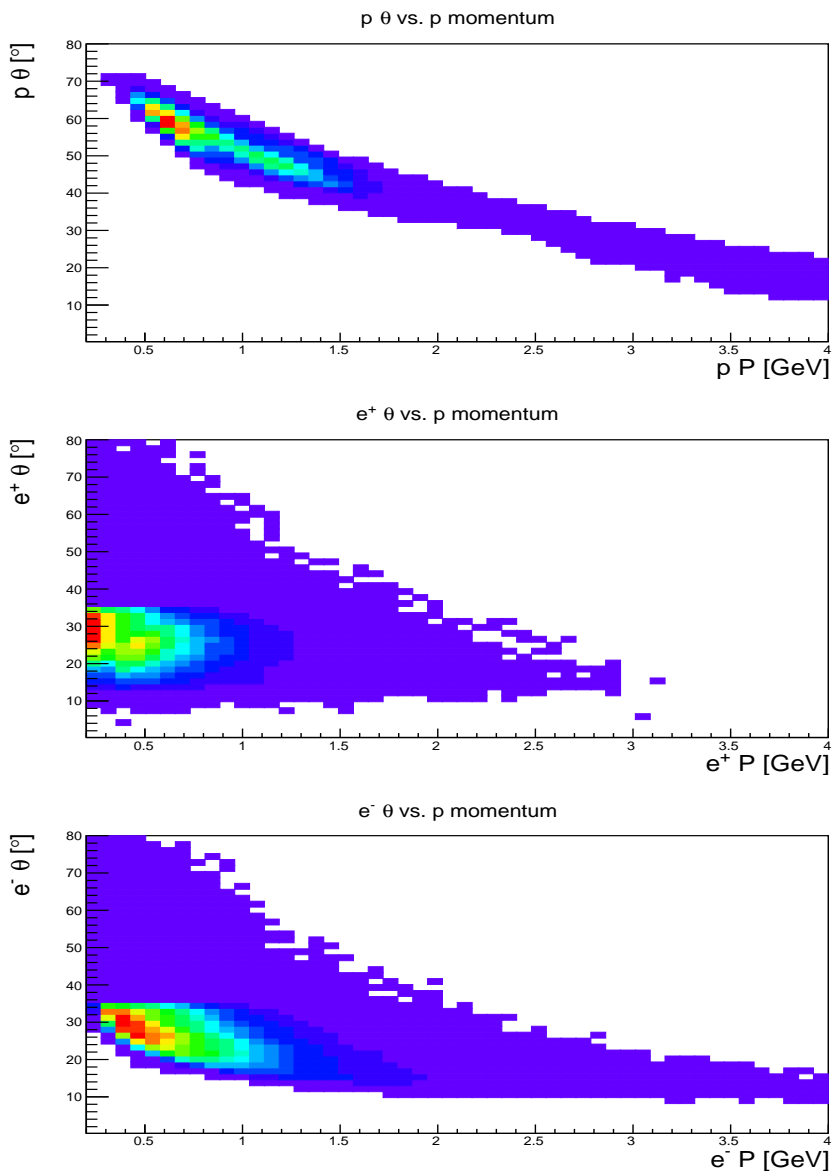


Figure 76: θ_{lab} vs. Momentum for proton (top), e^+ (middle), and e^- (bottom).